Spin-Orbit Misalignment of Planets Orbiting High-Mass Stars: Observations and Techniques Using NASA's Kepler Telescope

A Dissertation
Presented in Partial Fulfillment of the Requirements for the
Degree of Doctorate of Philosophy
with a
Major in Physics
in the
College of Graduate Studies
University of Idaho
by
John P. Ahlers

Major Professor: Jason W. Barnes, Ph.D.
Committee Members: Gwen Barnes, Ph.D.; Matthew Hedman, Ph.D.;
Brian Jackson, Ph.D.
Department Administrator: Ray Von Wandruska, Ph.D.

December 2018

Authorization to Submit Dissertation

This dissertation of John P. Ahlers, submitted for the degree of Doctorate of Philosophy with a Major in Physics and titled "Spin-Orbit Misalignment of Planets Orbiting High-Mass Stars: Observations and Techniques Using NASA's Kepler Telescope," has been reviewed in final form. Permission, as indicated by the signatures and dates below, is now granted to submit final copies for the College of Graduate Studies for approval.

Major Professor:	Jason W. Barnes, Ph.D.	Date
Committee Members:	Gwen Barnes, Ph.D.	Date
	Matthew Hedman, Ph.D.	Date
	Brian Jackson, Ph.D.	Date
Department Administrator:	Ray Von Wandruska, Ph.D.	Date

Abstract

This dissertation summarizes my graduate research on exoplanets orbiting high-mass, rapidly-rotating stars using NASA's *Kepler* telescope. In the included research, I bridge exoplanet observations with existing planet formation and evolution theories with the goal of constraining the mechanisms that torque planet orbits away from their host star's rotation plane. This phenomenon, known as spin-orbit misalignment, occurs surprisingly often around high-mass stars, suggesting that planet formation in these systems may be fundamentally different than that for solar-type stars. While many explanations have been put forth to explain spin-orbit misalignment, its root cause is still unknown. Observing spin-orbit misalignment around high-mass stars helps address this problem by comparing measurements against predicted spin-orbit distributions based on existing misalignment hypotheses to shed light on the planet formation processes taking place around high-mass stars.

This dissertation provides a detailed explanation of the gravity-darkening technique that I use to measure orbit geometries from photometric datasets collected by the *Kepler* spacecraft of planets transiting rapid rotators, and includes four published peer-reviewed papers relating to spin-orbit misalignment and planet formation. In Chapter 1, I summarize some of the outstanding questions regarding exoplanets and formation pathways and explain how spin-orbit misalignment challenges conventional formation theory. In Chapter 2, I discuss stellar gravity-darkening and explain how its photometric effects can be used to constrain spin-orbit alignment values. In Chapter 3, I present the analysis of the spin-orbit alignment value of Kepler Object of Interest 368 and demonstrate the capabilities of the gravity-darkening technique. In Chapter 4, I present the published project that measured the spin-orbit alignment of two-planet-system KOI-89 (now named Kepler-462). This work shows that the two planets have orbits significantly misaligned relative to their host star, but are well-aligned with each other, providing clues to the system's formation and evolution history. In Chapter 5, I show that gravity-darkened stars can produce unusual insolation patterns on the planets that orbit them, potentially driving atmospheric and surficial processes unlike anything seen in our solar system. In Chapter 6, I provide an additional technique for analyzing transit photometry by resolving and subtracting stellar seismic activity commonly seen in high-mass stars. This technique provides a new avenue for extracting information from the transit light curves polluted by stellar seismic activity and allows for the gravity-darkening technique to be applied to

previously inaccessible datasets. The work described in Chapter 6 has been accepted for publication. In Chapter 7, I discuss future work toward reconciling planet formation and spin-orbit misalignment.

Acknowledgements

While an undergraduate physics major, I had no particular interest in exoplanets. I had almost no exposure to the field of astrophysics while at Gonzaga University; I hadn't even considered it as a possible career until my future thesis advisor came to Gonzaga to recruit me. So, I can confidently say that I would not be where I am today without Jason Barnes. He asked me to come to the University of Idaho despite my limited experience with astronomy and patiently allowed me to transition to the world of astrophysics. He provided with me an interesting and unique research project and allowed me to pursue it in my own style, and mentored me with the best open-door policy I could possibly ask for. He gave me both the guidance and the freedom to take my research in new directions and helped me grow my work into something I can call my own. So to Jason, for bringing me to the University of Idaho, for advising me these past six years, and for all the stickball, I say thank you.

While at the University of Idaho, I was fortunate enough to be immersed in an exceptionally supportive environment. The first person to come to mind is my academic twin Shannon MacKenzie, who suffered countless late nights slaving away with me on E&M or quantum homework. She kept me sane through those classes and especially through our quals, and proved over and over to be a reliable friend and quality sounding board. I've also benefitted from sharing my workspace with a great group of people in the rest of the 301 cohort, including Rob Chancia, Rajani Dhingra, Joseph A'Hearn, Tim Hatchett, and Casey Cook-Hallet. It's been an honest pleasure sharing my workspace with all of them, and I'll always remember how much they all brightened my graduate experience.

I would also like to thank a few specific people with whom I have collaborated or pestered for letters of recommendation. Foremost is Matt Hedman, whose door is always open and who I am convinced secretly knows everything. Also I would like to thank Julian van Eyken and Rory Barnes for helping me explore new research ideas and working with me on various projects despite their incredibly busy schedules, and finally Gwen Barnes and Brian Jackson for agreeing to put in the time to make sure I am prepared to graduate to the next stage of my career.

Dedication

For Laura, who makes all of this worthwhile. And to our unborn baby: hopefully I can bore you with this someday.

Table of Contents

List of Tables

List of Figures

Chapter 1: Introduction

With the first exoplanet orbiting a main sequence star discovered in 1995 (Mayor & Queloz, 1995) and the majority of exoplanets discovered in the last ten years (Borucki, 2016), astronomers have only just begun exploring the rich and lush population of exoplanets in our galaxy. With many thousands of planets in nearby planetary systems now discovered, a growing realization about our galaxy is that planetary system architectures can vary tremendously.

Before this recent boon of exoplanet discoveries, the widely accepted nebular hypothesis described formation as a process that produces planetary systems with similar overall structures as our solar system (e.g., Woolfson, 1993). As a result, the assumption in astronomy was that our solar system serves as a blueprint for all other systems. Planets inside a planetary system's ice line likely form into small, rocky bodies, and planets outside its ice line form into massive gas and ice giants (O'Brien et al., 2006; Batygin & Brown, 2010; Boss, 2002). Planets typically end up in mostly-circular orbits with none of them extremely close to their host star, and all planet orbits should be relatively well-aligned with the system's invariable plane (Lissauer, 1993).

In the past two decades, exoplanet observations have proven every one of these assumptions incorrect.

Extrasolar gas and ice giants very frequently reside inside their system's ice line (Guillot et al., 1996; Rice & Armitage, 2005), implying that giant planets form beyond their system's ice line and then migrate inward much more commonly than previously thought. These close-in giants often reside far closer to their host stars than Mercury does in our own, with orbital periods of only a few days.

Gas giants with orbital periods of shorter than 10 days, or "Hot Jupiters", pose a formidable challenge to conventional formation theory. Current estimates place approximately 1% of all Sun-like host stars with at least one hot Jupiter, which implies that planets often form in a turbulent environment that commonly produces large-scale planet migration. The most likely way to produce close-in gas and ice giants is through resonances and dynamic interactions that drive up their eccentricities. Over time, tidal interactions between the star and planet near its periastron recircularize the orbit into much shorter-period orbits (Nagasawa et al., 2008). However, the possibility for some mechanism existing that forms Jupiter-mass planets in inner planetary systems directly

has not been ruled out (Batygin et al., 2016).

Many Jupiter- and Neptune-mass planets have been discovered not only interior to the ice line in their system, but in much shorter-period orbits than anything seen in our solar system. Figure 1.1 shows the orbital periods of the 3823 confirmed exoplanets to date, 2998 of which have orbital periods shorter than Mercury's and 1648 of which have orbital periods of under ten days. For example, the gas giant KELT-9b orbits its host star once every 1.48 days (Gaudi et al., 2017). Many systems contain several tightly-packed inner planets that likely migrated inward because of resonances, aerodynamic drift, or planet-planet scattering (Raymond et al., 2009; Boley & Ford, 2013; Boley et al., 2014; Jackson et al., 2016). Kepler-11 is one such system, with five terrestrial-mass planets all orbiting between 10 and 47 days around a Sun-like star (Lissauer et al., 2011). KELT-9, Kepler-11, and many similar systems pose a serious challenge in understanding how they stably form and evolve.

Unlike our solar system, many exoplanets orbit their host star in highly eccentric configurations. For example, the gas giant HD 80806b orbits its solar-type host star every 112 days with an eccentricity of $e = 0.927$ (Naef et al., 2001). This planet's timescale for circularization is Gyr, and its orbit is likely slowly evolving toward circular (Winn et al., 2009). In addition to being highly eccentric, the orbit of HD 80806b is significantly misaligned from the spin axis of its host star, with a projected misalignment angle of $\lambda \sim 50^\circ$ (see Figure 1.2 for angle definitions).

Recent exoplanet discoveries such as HD 80606b have shown that planet orbits tilt relative to the spin axis of their host star far more commonly than previously thought (Winn et al., 2005, 2010; Rogers et al., 2012). This phenomenon, known as spin-orbit misalignment, has been observed in over 100 extrasolar systems to date discovered by the *HATNet* (Bakos et al., 2004), *Hubble* (e.g., Henry et al., 1999), *KELT* (Pepper et al., 2007), *Kepler* (Borucki et al., 1997; Basri et al., 2005), *MASCARA* (Lesage et al., 2014), *TrES* (O'Donovan et al., 2006), *QES* (Alsubai et al., 2014), *WASP* (Pollacco et al., 2006), and *XO* (McCullough et al., 2005) telescopes. Together, these surveys have discovered dozens of systems with severely misaligned or even retrograde orbits. Figure 1.3 displays known extrasolar spin-orbit values to date.

Altogether, exoplanet discoveries over the last decade have revealed planetary system architectures that drastically contradict canonical planet formation theories based on the solar system. While exoplanets display a surprising diversity throughout our solar

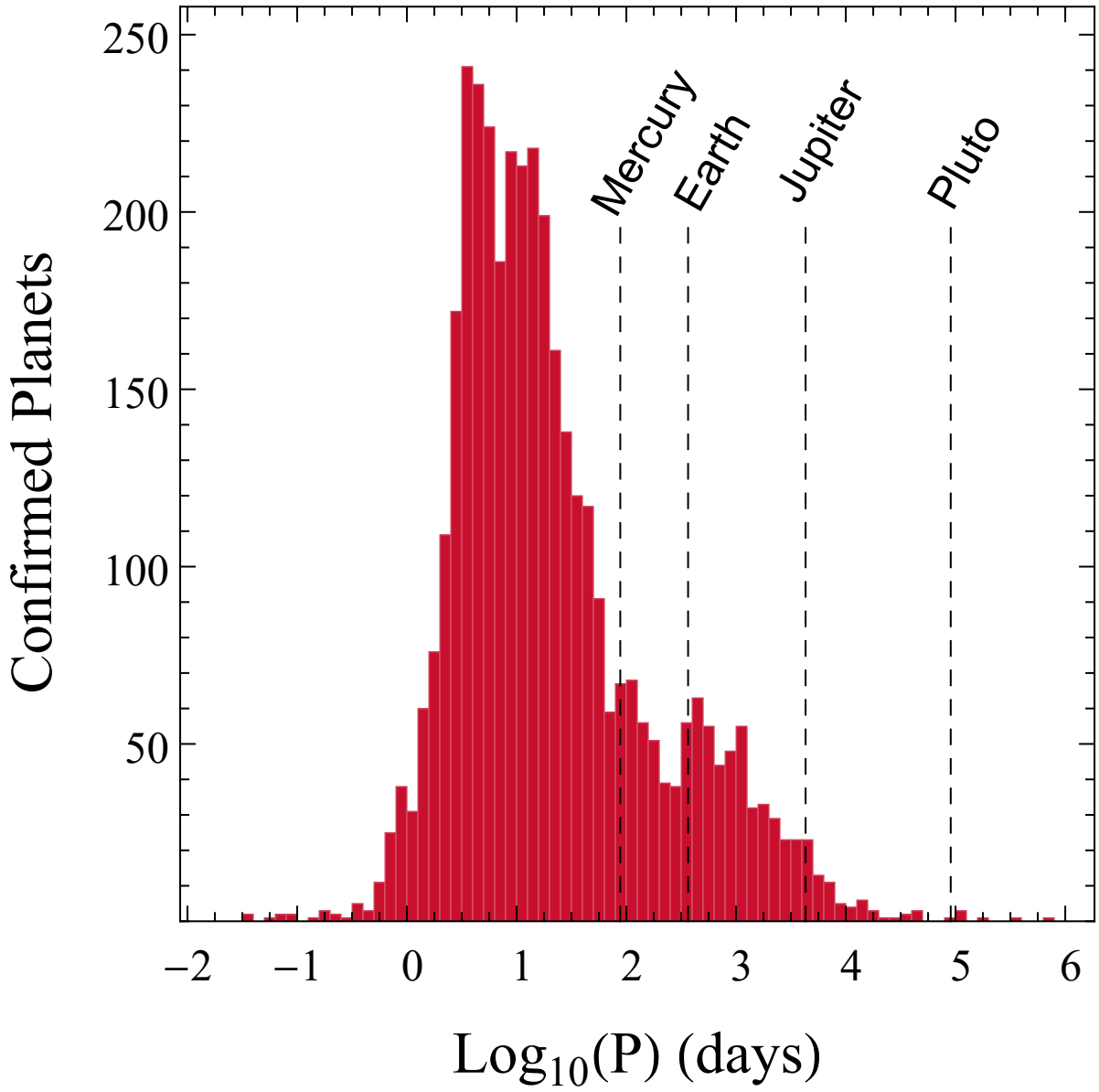

Figure 1.1: Orbital periods of 3823 confirmed planets in 2803 planetary systems. 2998 of those planets have orbital periods shorter than Mercury's 88-day year, 741 of which are ice/gas giants that likely formed beyond that system's ice line. Data provided by http://exoplanet.eu/catalog.

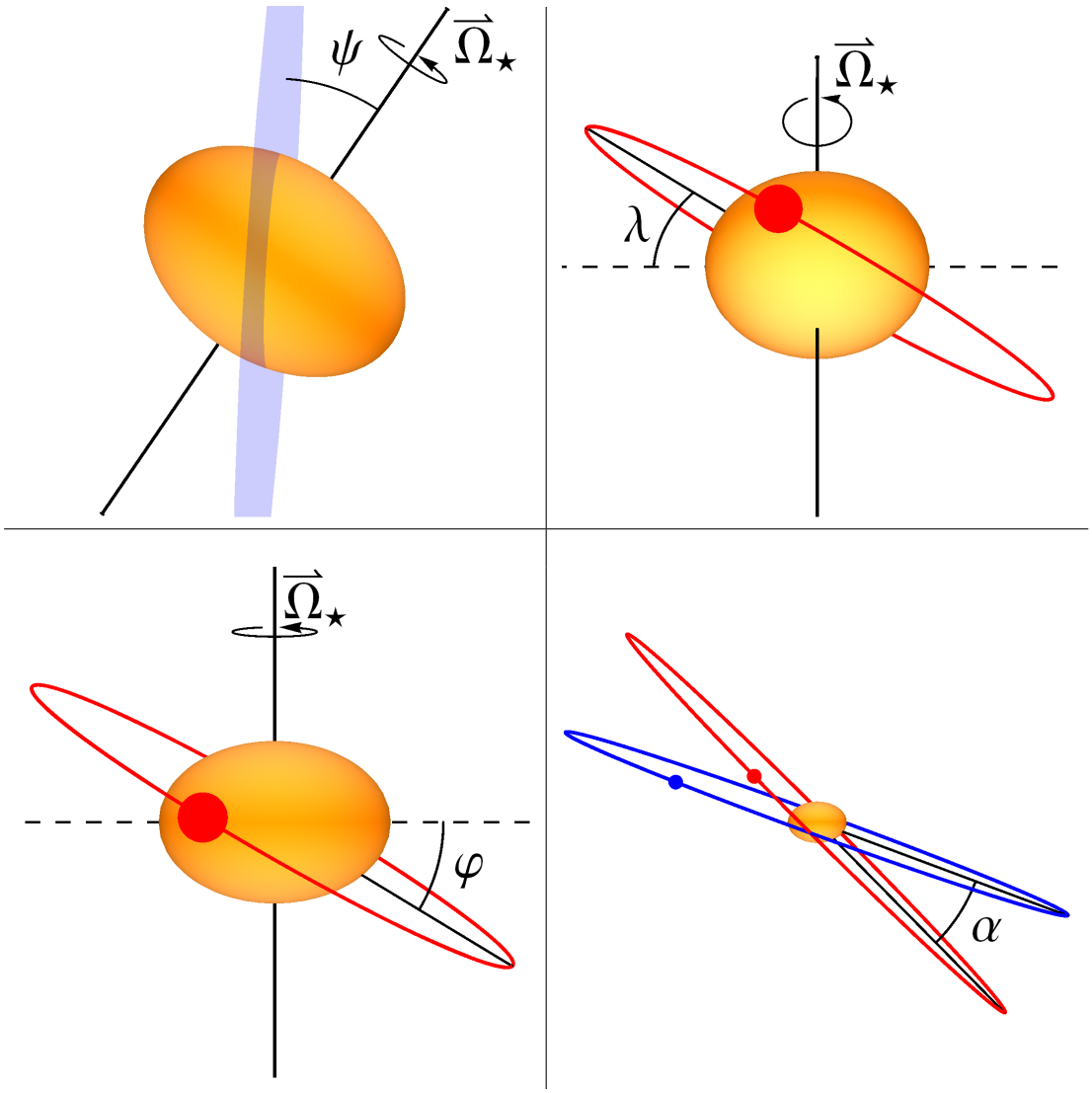

Figure 1.2: Top left: The stellar obliquity ψ is defined as the axial tilt toward/away the plane of the sky. The blue plane represents the plane of the sky. Top right: the sky-projected alignment λ is the misalignment angle seen from *Kepler's* point of view. It represents the tilt of planet's orbit vector relative to the star's *projected* rotation axis in the plane of the sky. Bottom left: the spin-orbit alignment φ is the angle between the plane of an orbit and the star's equatorial plane. Bottom right: the coalignment angle α is the angle between two orbit planes. This figure is from Ahlers et al. (2015) and is displayed again in Chapter 4.

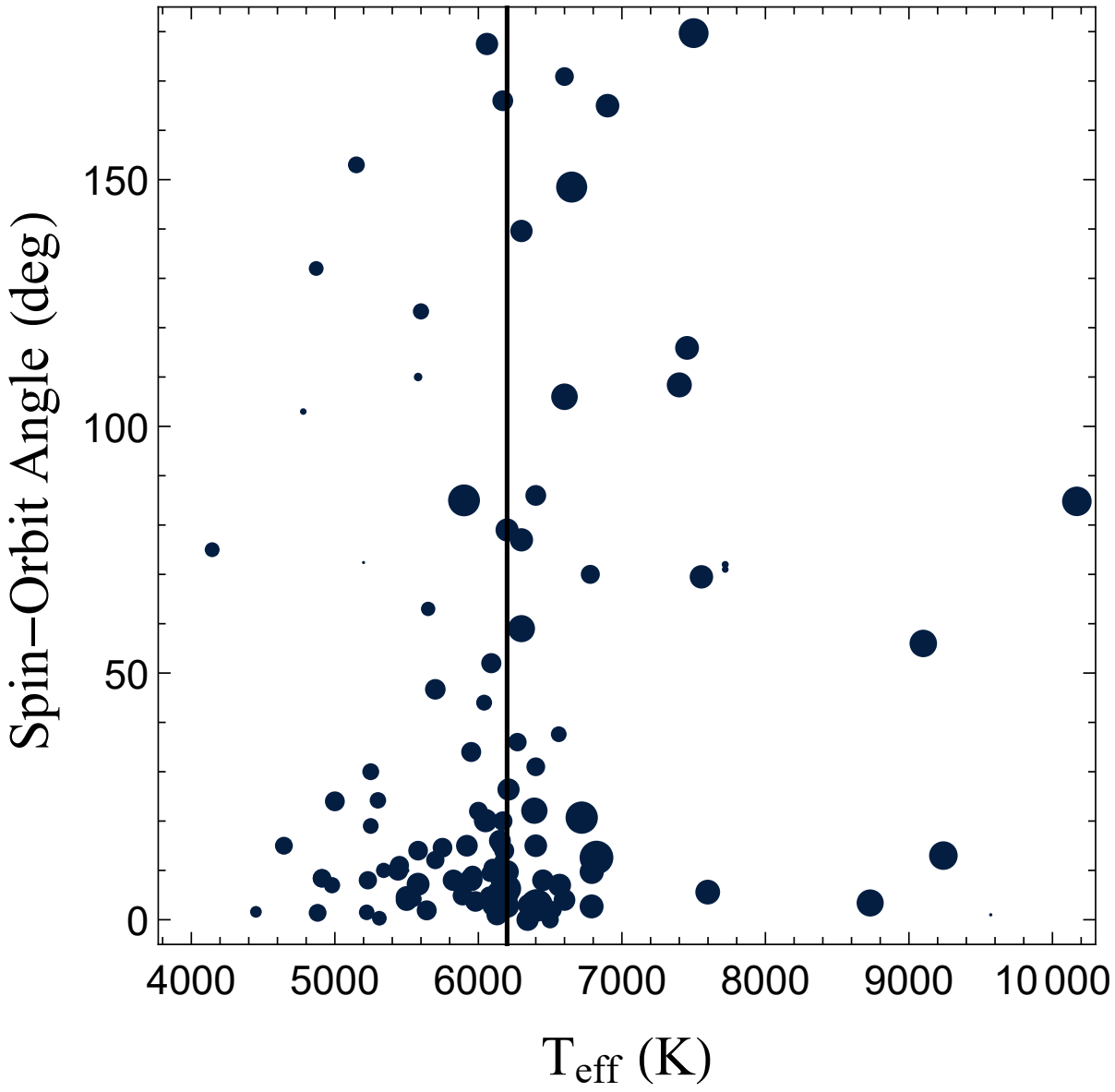

Figure 1.3: Absolute values of all measured spin-orbit alignments as a function of stellar effective temperature. The size of each data point represents that planet's radius. The vertical line at 6200 K indicates the generally-used cutoff between "high-mass" and "low-mass" stars in reference to spin-orbit misalignment although many new discoveries indicate that low-mass stars may commonly host misaligned planets as well (e.g., Albrecht et al., 2012). Most alignment values around low-mass stars were measured via the Rossiter McLaughlin effect (Gaudi & Winn, 2007) or asteroseismology (Campante et al., 2016), and around most high-mass stars using Doppler tomography (e.g., Collier Cameron et al., 2010) or gravity-darkening (Barnes, 2009).

neighborhood, the sample size of discoveries is actually quite small. The astronomy community has only just begun exploring nearby systems for exoplanets, and significant detection biases and challenges remain. The most prolific current method for finding exoplanets is the transit method, which detects exoplanets when they pass in front of their host star and block some of its light. This method requires the planet's orbit to be nearly perfectly aligned with the observer's line of sight to the host star, which occurs a very small fraction of the time. For example, a planet orbiting a sun-like star at 1 AU has only a 0.47% probability of transiting, implying that transit surveys such as NASA's *Kepler* mission actually detects a small fraction of nearby planetary systems (Borucki et al., 1985). This detection method also requires the planet to be large enough to block a detectable amount of light, biasing detections toward larger planets. Additionally, the telescope must actually be looking at the star during each planet's brief transit in order to detect it, biasing detections against finding long-period planets that transit less frequently.

The other existing methods for discovering exoplanets share similar biases. For example, the spectroscopic radial velocity technique takes advantage of mutual gravitation between a host star and an orbiting planet to detect Doppler shift in the star's emission spectrum (Cumming, 2004). As the star is gravitationally perturbed by an orbiting body, it moves slightly in and out of the plane of the sky, causing its spectrum to alternate between red- and blue-shifted. The larger amplitude and higher frequency of that motion, the more detectable its Doppler shift, biasing the radial velocity technique towards discovering high-mass, short-period planets, ultimately discovering a very similar sample of exoplanets as the transit method.

Overall, extrasolar systems are not well-sampled yet. At the time of this writing, exoplanets.nasa.gov lists 3,735 confirmed exoplanets in 2,787 planetary systems and lists another 2,723 current planet candidates. Best estimates suggest that there is *at least* one planet per star in our galaxy (Cassan et al., 2012), and that number is trending upward all the time, giving a reasonable estimate at one trillion total exoplanets in the Milky Way alone. We have only discovered a tiny fraction of total planets even in the nearby part of the galaxy, and the population we have found exhibits severe detection biases. Finding terrestrial-scale exoplanets is still very challenging, and we know almost nothing of the state of the outer part of extrasolar systems. We cannot claim to know the true structure of a single planetary system – perhaps not even our own if Planet Nine exists (Batygin & Brown, 2016). Although tremendous progress has been made in the field of

exoplanets in the last 20 years, we have not yet produced robust exoplanet statistics. I submit that neither theory nor observation have yet spelled out all the possible ways to build a planetary system.

Both observation and theory have a long way to go toward constraining planet formation pathways. Current big-picture challenges include explaining planet migration mechanisms that form hot Jupiters/Neptunes or that produce spin-orbit misalignment. Exoplanet observations must overcome strong detection biases and collect a large enough of a discovery sample to properly test exoplanet statistics against formation theory. We need to know bulk parameters such as planet mass distributions as a function of orbital period and planet occurrence rates as a function of stellar type. We also need to better constrain dynamic processes that can affect system architecture such as protoplanetary disk interactions with stellar companions (Lai, 2014; Xiang-Gruess & Papaloizou, 2014) and Lidov-Kozai resonance (Lidov, 1961; Kozai, 1962) or other resonances. Additionally, we must better constrain planet occurrence rates as a function of stellar metallicity, planetary system carbon/oxygen ratios, and protoplanetary disk compositions to better understand formation and evolution processes.

This dissertation takes a small step toward the enormous task of bridging exoplanet discoveries with solar system formation and evolution theories by connecting current theories and observations of spin-orbit misalignment around high-mass stars. In Chapter 2, I discuss measuring spin-orbit misalignment around high-mass stars through transit photometry. In Chapters 3 and 4, I detail the spin-orbit alignment values of planetary systems KOI-368 and Kepler-462 and examine their possible formation scenarios. In Chapter 5, I explore the surficial and atmospheric effects that spin-orbit misalignment could have on exoplanets orbiting high-mass stars. In Chapter 6, I derive a technique for overcoming stellar variability in high-mass stars. In Chapter 7, I discuss the impact of my graduate work and further consider the importance of spin-orbit misalignment toward understanding solar system formation.

Chapter 2: Measuring Spin-Orbit Misalignment via Gravity-darkening

High-mass stars ($M_\star \geq 1.3\ M_\odot$) exhibit a different internal structure than low-mass stars. Our own Sun's primary radial zones are its core, its interior radiative zone, and its outer convective zone. The Sun's radiative zone transports energy radially outward through radiative diffusion (Gough & McIntyre, 1998). In its convection zone, plasma transports energy through bulk convective cycling (Christensen-Dalsgaard et al., 1996).

In general, stars less massive than the Sun have larger convective zones and smaller radiative zones, and stars more massive than the Sun have larger radiative zones and smaller convective zones (Toomre et al., 1976). However, at masses higher than $\sim 1.3 M_\odot$ the star's carbon-nitrogen-oxygen cycle of nuclear fusion produces an extremely high core temperature, causing the core itself to become convective. This convective core resides inside a radiative region that extends to the star's surface. The result is that these stars are effectively inside-out from their low-mass counterparts, with convective interiors and radiative exteriors. Albrecht et al. (2012) identifies this inversion at a stellar surface temperature of $\sim$ 6200K. Throughout this dissertation, I use $M_\star \approx 1.3 M_\odot$ and $T_{\rm eff} \approx 6200$ as approximate cutoffs for designating a star "high-mass" or "low-mass".

As a consequence, high-mass stars have weak external magnetic fields. Solar dynamo theory states that stellar magnetic fields are caused by the convection zone of the star (Charbonneau, 2014), so the magnetic field in high-mass stars should be mostly internal near its convective core. Recent observations using NASA's *Kepler* telescope corroborate this theory (e.g., Bagnulo et al., 2006; Boehm et al., 2015).

Without a strong external magnetic field, no stellar magnetic braking takes place, allowing high-mass stars to maintain their primordial rotation rates throughout their lifetimes (Mestel, 1968). All stars start off spinning quickly during their formation as protostellar material collapses inward (Hansen & Kawaler, 1994); however, low-mass stars' external magnetic fields cause them to slowly decrease their rate of rotation over time. This effect, called magnetic braking, occurs when the star's magnetic field transfers angular momentum into an escaping stellar wind. These outflows are stirred by the star's magnetic field, which transfers angular momentum from the star to the outflow, slowing the star's rotation rate. With little-to-no external magnetic field, magnetic braking does not occur for high-mass stars, allowing them to keep their initial angular momentum and

stay rotating rapidly throughout their lifetimes.

The second important difference between high- and low-mass stars is that stars with radiative exteriors exhibit relatively weak tidal dissipation (Villaver et al., 2014). Stellar tidal dissipation and planet orbit circularization occur primarily due to gravitational interactions between the star's convective region and the planet, which for high-mass stars, is far beneath the stellar surface. A high-mass star's outer radiative zone exhibits a higher tidal quality factor and thus exchanges less angular momentum with its orbiting bodies through tidal dissipation.

These two stellar properties, weak external magnetic fields and weak tidal dissipation, result in high-mass stars commonly rotating rapidly throughout their lifetimes (Epstein & Pinsonneault, 2013). Their rotation rate often hovers near their rotational break-up speed, with equatorial rotational velocities reaching hundreds of kilometers per second. The Darwin-Radau relation (Bourda & Capitaine, 2004, e.g.,) models how rotation distorts a body's hydrostatic equilibrium into an oblate spheroid,

$$\frac{C}{mR_\star^2} = \frac{2}{3}\left[1 - \frac{2}{5}\left(\frac{5\Omega_\star^2 R_{\rm eq}^3}{2\zeta G M_\star} - 1\right)^{1/2}\right] \tag{2.1}$$

where C is the star's moment of inertia about its rotation axis, $R_{\rm eq}$ and $R_{\rm pole}$ are the star's equatorial and polar radii, $\zeta \equiv (R_{\rm pole} - R_{\rm eq})/R_{\rm pole}$ is the stellar oblateness factor, $\Omega_\star$ is the star's rotation rate, and $R_\star \equiv R(\theta)$ is the stellar radius at a given polar angle θ. The resulting high centrifugal force near its equator reduces the star's effective surface gravity,

$$\vec{g_{\rm eff}} = -\vec{\nabla}\left[\frac{-GM_\star}{R_\star}\left(1 - \frac{J_2 R_{\rm eq}^2 P_2(\mu)}{R_\star}\right) - \frac{1}{2}\Omega_\star^2 R_\star^2 \sin^2(\theta)\right], \tag{2.2}$$

where J_2 is the second-order gravitational harmonic term, and $P_2(\mu)$ is a second-order Legendre polynomial. The centrifugal force term $\frac{1}{2}\Omega_\star^2 R_\star^2 \sin^2(\theta)$ is negligible for slow rotators like our Sun, but rapid rotation in high-mass stars can produce massively distorted stellar surfaces. For example, the well-known rapid rotator Altair has an oblateness factor of 0.177, meaning its polar radius is only 82.3% of its equatorial radius (Monnier et al., 2007).

The smaller surface gravity near the star's equator results in a lower stellar effective temperature. The von Zeipel theorem (Von Zeipel, 1924) or "gravity-darkening law" relates surface gravity with effective temperature:

$$T_{\rm eff} = T_{\rm pole} \left(\frac{g_{\rm eff}}{g_{\rm pole}} \right)^{\beta} \tag{2.3}$$

where β is the so-called gravity-darkening exponent (GDE). Rapid rotation produces a pole-to-equator temperature gradient across the stellar surface, resulting in the pole of an oblate spheroid that can be several thousand Kelvin hotter than its equator. As an example, Altair's stellar effective temperature likely varies from $\sim$ 8500K to 6500K between its hot poles and cool equator (Kervella et al., 2005).

Von Zeipel (1924) originally assumed that $\beta = 0.25$, invoking the assumption that stars emit light as perfect black body radiators. However, more recent works have demonstrated that this assumption is not always accurate. For example, Monnier et al. (2007) showed that Altair's true GDE lies somewhere between 0.19 and 0.25. In general, β approaches 0.25 as stellar masses increase due to the grown of the radiative exterior; however, the true relationship between surface gravity and effective temperature is complicated and remains somewhat unclear. Its deviation from a true blackbody may arise from the fact that Altair's outermost layer might not be purely radiative or might still maintain a small convective envelope.

Work following in the footsteps of Von Zeipel (1924) has further shed light on the nature of gravity-darkening. Kopal (1959) introduced and Martynov (1973) improved the idea of using gravity-darkening coefficients to account for both bolometric and wavelength-dependent quantities. More recently, several works calculated expected bandpass-integrated gravity-darkening coefficients as a function of stellar properties for the *Kepler*, *Spitzer*, and *CoRoT* space telescopes (Claret & Bloemen, 2011), as well as for NASA's newly-launched Transiting Exoplanet Survey Satellite (*TESS*) (Claret, 2017).

An object transiting a rapidly-rotating star can block some of the pole-to-equator luminosity gradient emitted by the star's surface. When the object transits near the stellar pole, it blocks a hotter, brighter part of the stellar surface than when it transits near the equator. Barnes (2009) first modeled transit light curves of planets orbiting rapidly-rotating stars and by the star's latitudinal asymmetry can affect transit depth, transit duration, overall transit light curve shape, and ingress/egress symmetry depending on the planet's transit properties.

Figures 2.1, 2.2, and 2.3 demonstrate the various ways in which gravity-darkening can influence a transit light curve. They display transit light curves for various stellar

obliquities, projected alignments, and impact parameters for transits across an extremely rapidly-rotating star. To generate these light curves, I simulated a 1.0 $R_{\rm Jup}$ planet transiting across a $M_\star = 1.5\ M_\odot$ star with a $P_{\rm rot} = 12$ hr rotation period, a $R_\star = 2.0 R_\odot$ equatorial radius, a $T_{\rm pole} = 8000$ K polar surface temperature, a $\beta = 0.25$ gravity-darkening exponent, and a derived oblateness factor of 0.202.

Note that the gravity-darkening effect on the transits in Figures 2.1, 2.2, and 2.3 than typically observed in photometric datasets. These figures include an extremely gravity-darkened star rotating near its break-up speed, an ideal $\beta = 0.25$ gravity-darkening exponent that maximizes the star's luminosity gradient (Equation 2.3), and specifically chosen transit geometries that maximize the gravity-darkening anomalies. These effects on known gravity-darkened transits have been much more subtle. For example, Kepler-13Ab's gravity-darkened transit light curve deviates only slightly away from a standard transit shape (Figure 2.4). However, even from that small effect, orbit geometry parameters have been extracted (Barnes et al., 2013; Masuda, 2015).

The process of measuring spin-orbit misalignment from a gravity-darkened light curve, first derived in Barnes (2009), involves fitting transit photometry to a transit model that includes an oblate, rapidly-rotating star. In general, the expression describing the amount normalized stellar flux (F) blocked at any given time during a transit event is,

$$F = 1 - \frac{\int_0^{R_\star} \int_0^{2\pi} I(r,\theta)\ \Gamma(r,\theta) r\ d\theta\ dr}{\int_0^{R_\star} \int_0^{2\pi} I(r,\theta)\ r\ d\theta\ dr} \tag{2.4}$$

where $I(r,\theta)$ is the flux per unit area of the particular (r,θ) location on the stellar disk, and $\Gamma(r,\theta)$ is a function that denotes the location of the transiting object by yielding 1 for blocked locations and 0 everywhere else. Functionally, one can evaluate the θ portion of the integral by finding both limbs of the planet at distance r by use of a root-finding routine and then integrating $I(r,\theta)$ between these known limb locations. Note that Equation 2.4 calculates the *instantanous* flux blocked; when fitting a photometric light curve, one must account for the averaging that occurs over each time bin. For example, the *Kepler* telescope's photometric cadences are one minute and thirty minutes for short- and long-cadence data, respesctively (Borucki, 2016).

The flux density $I(r,\theta)$ must account for the projected area of each part of the stellar surface, and needs include a term for stellar limb-darkening. Ahlers (2016) accounts for these properties by setting

$$I(r,\theta) = B(T(\theta'))\frac{I(\mu)}{I(1)}\mu R_\star(\theta')\sin^2(\theta'), \tag{2.5}$$

where $B(T(\theta'))$ is the stellar emission function, θ' is the star's polar angle, $I(\mu)/I(1)$ is the stellar limb-darkening profile, and $\mu = \cos(\pi - \epsilon)$ describes the angle between the line-of-sight and the normal vector of the star's surface (see Figure 5.1). Also, $I(r,\theta)$ must account for the photometric bandpass of the telescope in use. For example, *Kepler's* response function spans from about 420nm to 900nm (Van Cleve & Caldwell, 2016).

Barnes (2009) derives one approach to numerically evaluate Equation 2.4. This work derives the effective oblateness – that is, the ratio of the long and short axes of the projected disk – to be,

$$\zeta_{\rm eff} = 1 - \sqrt{(1-\zeta)^2\cos^2(\psi) + \sin^2(\psi)}, \tag{2.6}$$

where ζ is the true oblateness and ψ is the stellar obliquity. Figures 2.1, 2.2, and 2.3 show how the shape of the projected disk changes at different ψ values, with $\psi = 0°$ yielding the highest effective oblateness and $\psi = 90°$ yielding no effective oblateness.

Barnes (2009) uses the effective oblateness to account for the star's shape through a Cartesian coordinate transform,

$$y' = \frac{y}{1-\zeta_{\rm eff}}, \tag{2.7}$$

where y is the coordinate running parallel to the projected disk's short axis. This transform expands the stellar projected disk into a circle, making the integral in Equation 2.4 much easier to calculate.

With both the stellar luminosity gradient (Equation 2.3) and the oblate shape of the star (Equations 2.6 and 2.7) included in a transit light curve model, the gravity-darkening effect is fully accounted for. All of these effects are modeled using the fitting software `transitfitter` (Barnes & Fortney, 2003).

In general, the fitting algorithm in `transitfitter` uses the parameters listed in Table 2.1 to model a transit light curve. The impact parameter b, the sky-projected alignment λ and the stellar obliquity ψ constrain the planet's spin-orbit alignment value (φ) via,

$$\cos(\varphi) = \sin(\psi)\cos(i) + \cos(\psi)\sin(i)\cos(\lambda) \tag{2.8}$$

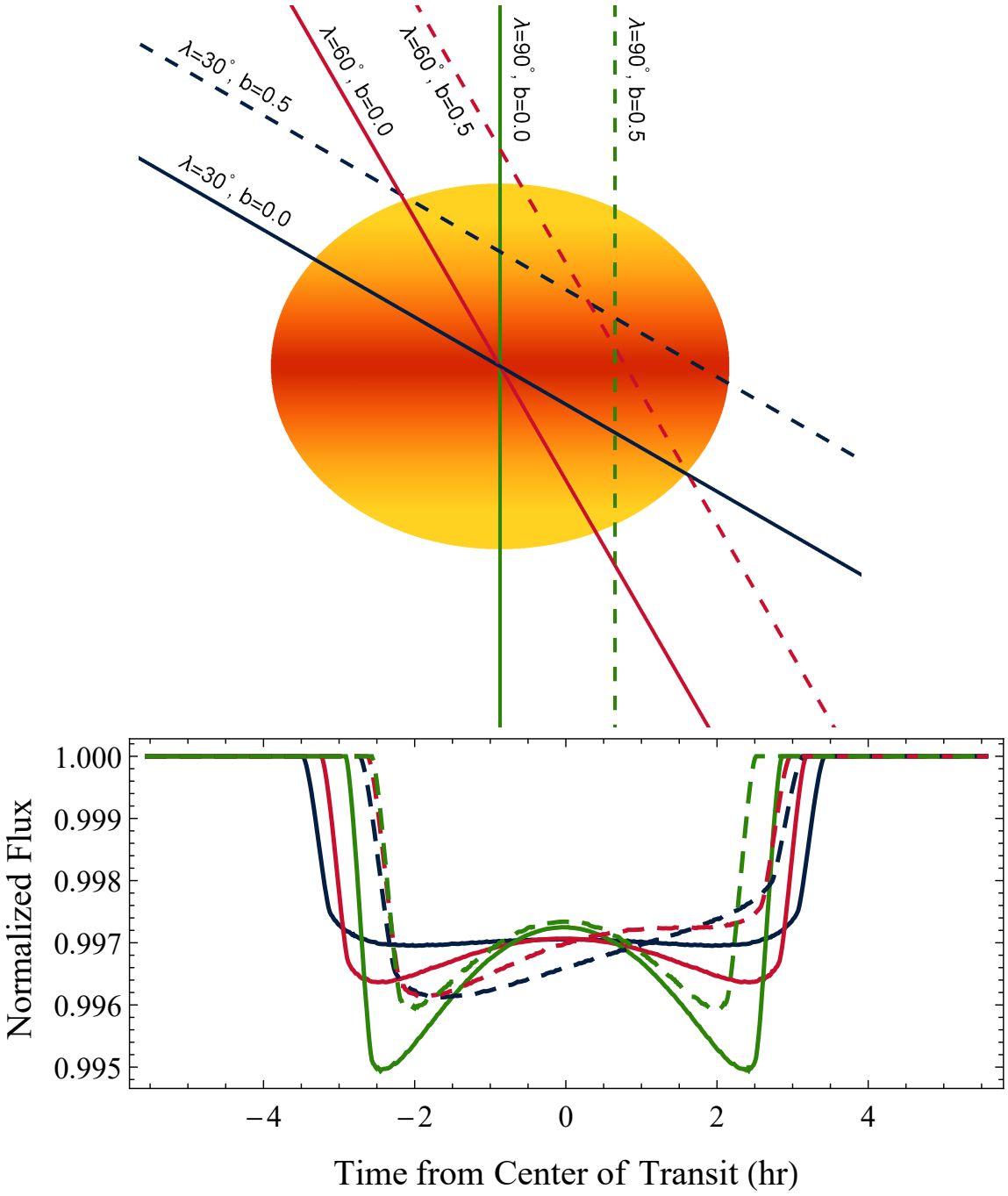

Figure 2.1: Transit light curves across an oblate, rapidly rotating star. The star's rotation axis is positioned in the plane of the sky, meaning its obliquity (ψ) is 0° (see Figure 1.2 for angle definitions). The blue, red, and green lines show transits with projected alignment (λ) values of 30°, 60°, and 90°, respectively. The solid lines indicate impact parameters (b) of 0.0, and the dashed lines indicate $b = 0.5$. All transits occur left-to-right across the stellar surface. Gravity-darkening produces very different effects on a transit light curve depending on the viewing geometry. For example, the dashed blue light curve ($\lambda = 30°$, $b = 0.5$) is left-right asymmetric as the planet starts transiting near the star's bright north pole and then gradually blocks less light as it transits the star's equator.

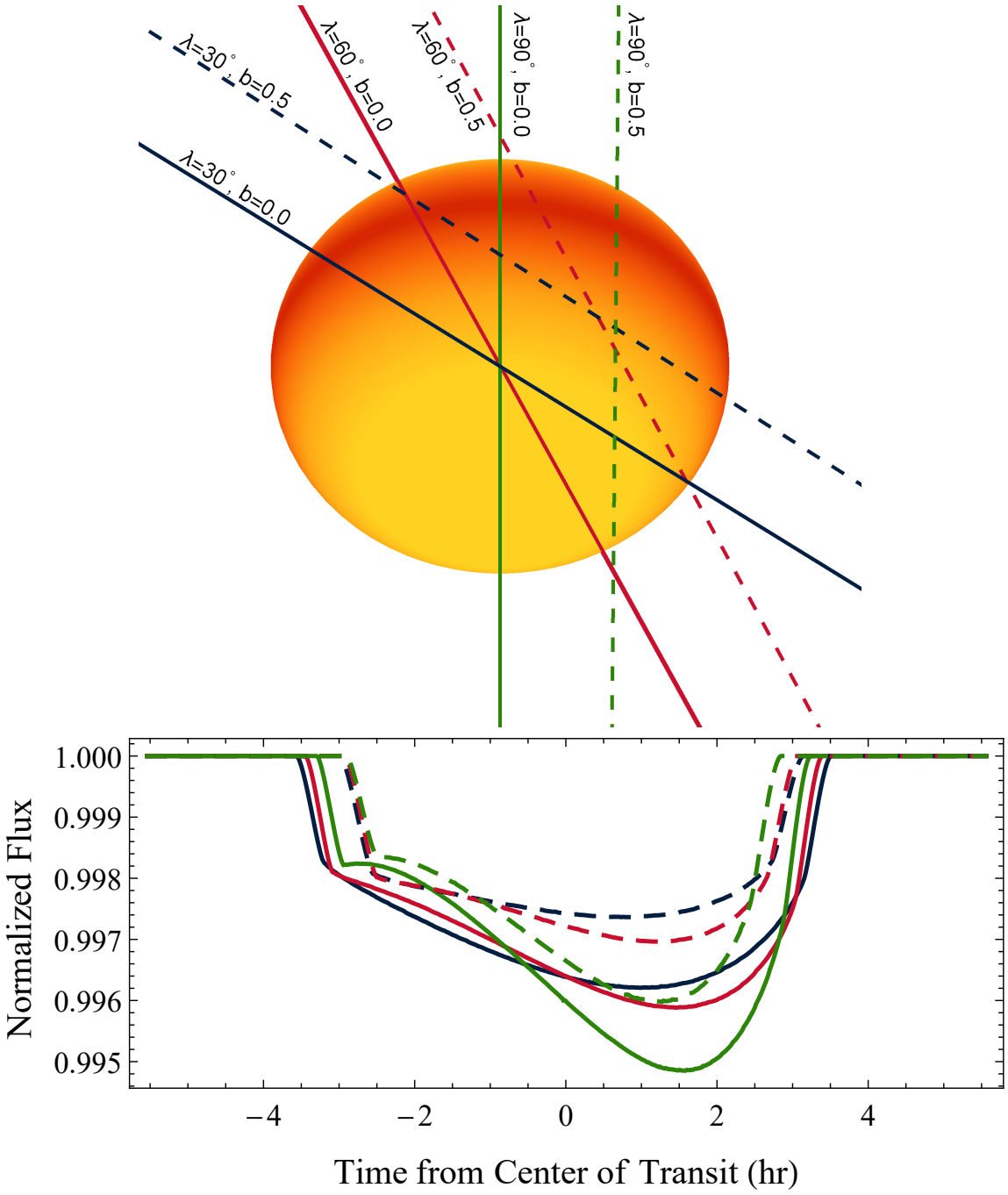

Figure 2.2: Synthetic gravity-darkened transit light curves using the same transit geometries as Figure 2.1 but with stellar obliquity $\psi = 45°$. Now the north pole of the star is tilted out of the plane of the sky, placing the brightest part of the star (the poles) closer to the center of the projected disk. The star's gravity-darkening now somewhat mimics the luminosity gradient due to limb-darkening, resulting in transit light curve anomalies somewhat different than for $\psi = 0°$. For example, the solid green transit ($\lambda = 90°$, $b = 0.0$) now produces a highly asymmetric light curve, with the greatest transit depth occurring near the stellar pole.

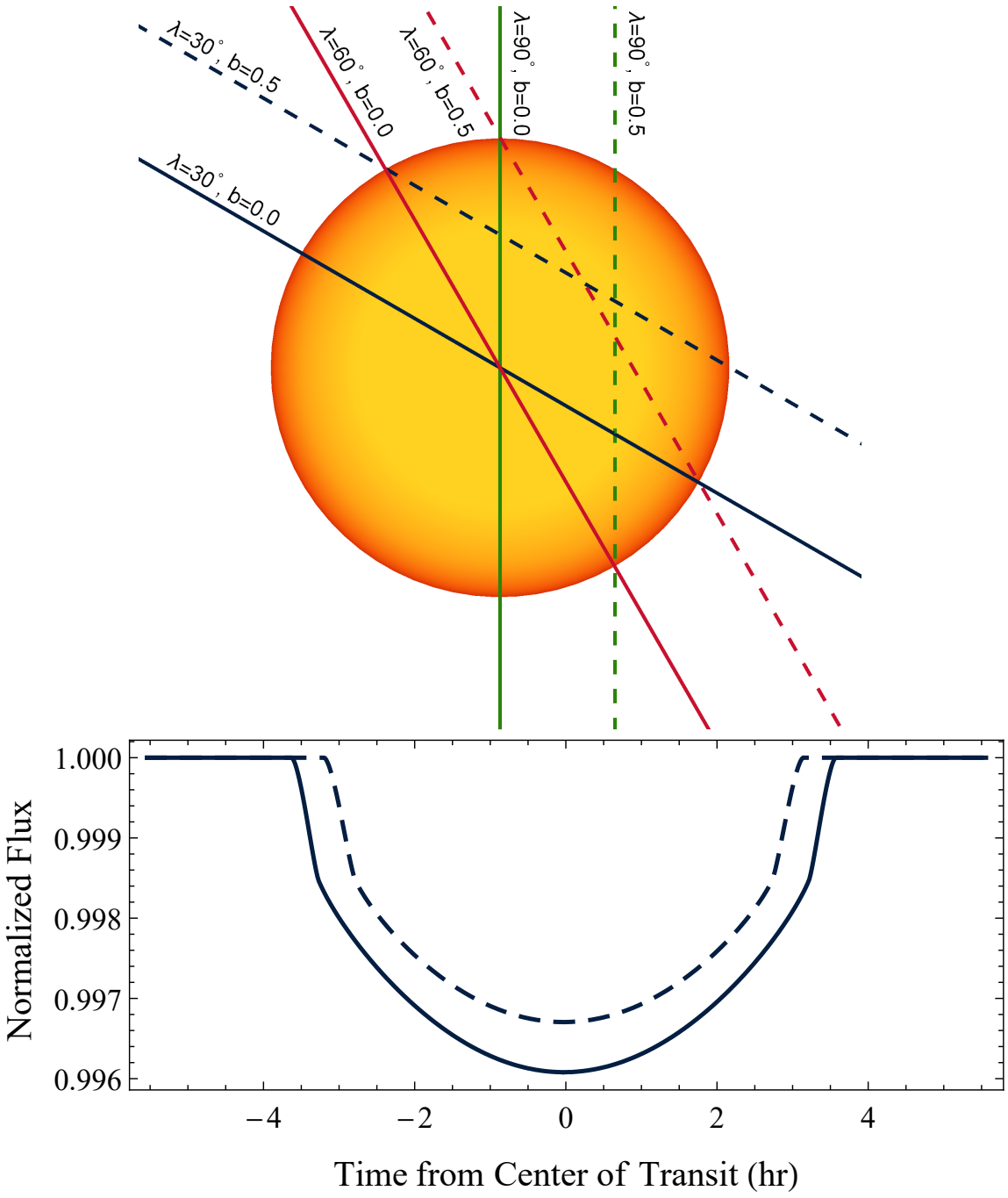

Figure 2.3: Synthetic transit light curves with $\psi = 90°$. Now, the star's south pole is located at the center of the stellar projected disk. Note that in this configuration, the asymmetries caused by the stellar luminosity gradient and the stellar oblateness both vanish, leaving a radially symmetric disk in the plane of the sky. Limb-darkening and gravity-darkening are effectively additive from this viewing geometry, and the symmetric stellar disk produces exclusively symmetric transit light curves. The planet's projected alignment (λ) has no effect on the shape of the light curve.

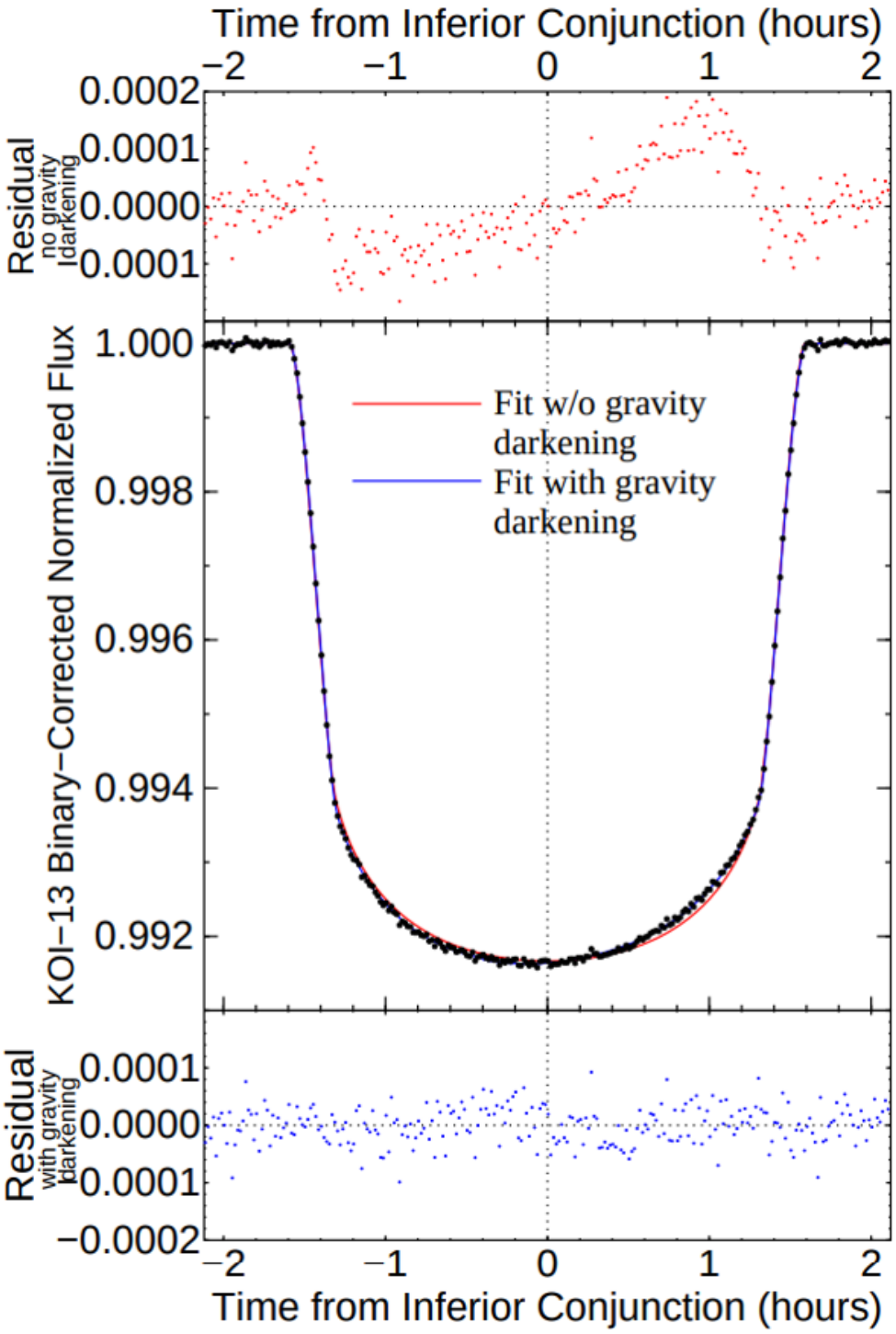

Figure 2.4: Transit light curve of Kepler-13Ab, from Barnes et al. (2013). A best-fit model that does not include gravity-darkening produces distinct, asymmetric residuals, due to a slight left/right asymmetry caused by the star's gravity-darkened, asymmetric shape.

Parameter	**Definition**	**Free/Constant**
$R_{\rm p}/R_\star$	Ratio of planet radius and stellar radius	Free
$T_{\rm cent}$	Time at center of transit	Free
b	Transit impact parameter	Free
F_0	Average stellar flux	Free
λ	Sky-projected alignment	Free
ψ	Stellar obliquity	Free
$M_\star$	Stellar mass	Constant
$T_{\rm pole}$	Stellar effective temperature at its poles	Constant
P	Orbital period	Constant
c_1	First quadratic limb-darkening term	Constant
c_2	Second quadratic limb-darkening term	Constant
$v\sin(i)$	Sky-projected rotational velocity	Constant
β	Gravity-darkening exponent	Constant
ζ	Stellar Oblateness	Derived

Table 2.1: Standard parameters involved in fitting a transit light curve with a gravity-darkened model. Parameters held constant or allowed to float are indicated. This table does not include a planet's eccentricity or argument of periapsis; ostensibly, fitting these parameters is possible, but it requires extremely high photometric precision and can be difficult to distinguish from the gravity-darkening signal.

where the sky-projected inclination i is the angle between the planet's orbital pole and the plane of the sky, which is an alternate expression for impact parameter ($b = a\cos(i)/R_\star$ for circular orbits, where a is the semi-major axis). Note that the gravity-darkening signal a four-way degeneracy between λ and ψ. Works such as Barnes et al. (2011), Ahlers et al. (2014), and Ahlers et al. (2015) assume $0^\circ \leq |\lambda| \leq 90^\circ$ and $0^\circ \leq \psi \leq 90^\circ$ in order to overcome this degeneracy, producing spin-orbit angles of either φ or $2\pi - \varphi$. The gravity-darkening technique cannot distinguish between prograde/retrograde orbits.

The fitting software `transitfitter` employs the quadratic limb-darkening law to model transit light curves,

$$I(\mu) = 1 - u_1 \cos(\pi - \epsilon) - u_2 \cos^2(\pi - \epsilon) \tag{2.9}$$

where ϵ is the angle between the line of sight and the normal vector of the star's surface (see figure 5.1) and $c_1 = u_1 + u_2$ and $c_2 = u_1 - u_2$. Table 2.1 lists c_1 and c_2 as constants during light curve fitting; however, two different approaches exist. The first approach is to use assumed values derived from works such as Claret & Bloemen (2011), which provide best-estimates for limb-darkening coefficients as functions of stellar temperature and mass. The second approach is to directly fit limb-darkening coefficients, which ostensibly can work for high signal-to-noise datasets and as long as the stellar obliquity isn't too close to 90°, where gravity-darkenening and limb-darkening become degenerate. Barnes et al. (2013) fit the gravity-darkened Kepler-13Ab light curve using assumed limb-darkening coefficients of $c_1 = 0.49$ and $c_2 = 0.0$, following Brown et al. (2001). However, the resulting fit of Kepler-13Ab's sky-projected alignment differed significantly from the spectroscopically-determined value measured by Johnson (2013). Masuda (2015) found a possible reconciliation between Barnes et al. (2013) and Johnson (2013) by fitting limb-darkening coefficients and instead holding the sky-projected alignment constant. Ultimately, the proper course of action for handling stellar limb-darkening in gravity-darkened models remains an area for further exploration.

The stellar oblateness ζ is derived from Equation 2.1 using the stellar radius, stellar mass, and $v\sin(i)$ value. The stellar luminosity gradient that ultimately drives gravity-darkening anomalies in transit light curves is modeled by ζ and the gravity-darkening exponent β (Equation 2.3).

The gravity-darkening technique serves as a useful tool for determining whether a planet is well-aligned or misaligned from its host star. It targets planets orbiting high-

mass stars, a particularly interesting population for spin-orbit alignment. It can constrain the *full* spin-orbit angle, whereas other methods only constrain either the sky-projected alignment or the stellar obliquity. The *Kepler* mission produced thousands of quality transit light curves, many of which are from high-mass, rapidly rotating stars. The not-fully-processed *K2* mission yield will likely reveal dozens more gravity-darkened transiting systems, and NASA's new *TESS* mission is expected to find over a thousand planets orbiting A/F-type stars (Barclay et al., 2018). This technique will therefore continue to serve as a valuable tool for for exploring planet formation and for extracting valuable information from existing transit light curves for the foreseeable future.

Chapter 3: Spin-Orbit Alignment for 110-Day-Period KOI368.01 from Gravity-darkening

"Spin-orbit alignment for 110 day period KOI368.01 from gravity-darkening." *The Astrophysical Journal*, vol. 786, no. 2, 2014, pp. 131-139.

This published article, co-authored by then-undergraduate Shayne Seubert and thesis advisor Barnes, served to establish the capability of the gravity-darkening technique to measure spin-orbit alignment. At the time of publication, the only other system to have its spin-orbit alignment angle measured through gravity-darkening was that of Kepler-13Ab (Barnes et al., 2011), and the full extent of gravity-darkening's usefulness was still largely unestablished among the astronomy community. Hirano et al. (2012) state that "asymmetries in the transit light curve may be used to determine the [alignment] parameters only if the spin-orbit angle is large.", referring to the asymmetry that gravity-darkening can produce in misaligned transit light curves that can reveal a planet's geometry. However, we demonstrate that the gravity-darkening technique can constrain well-aligned values as well from a transit's lack of asymmetry. We chose the high signal-to-noise system Kepler Object of Interest (KOI) 368 due to its high-quality photometry and very-nearly symmetric transit light curve. This system, consisting of a rapidly-rotating A star and an eclipsing M-dwarf, served as an ideal target to establish gravity-darkening as a useful tool for constraining orbit geometries. At the time of publication, the planet was listed as a "planet candidate" and not yet identified as an eclipsing binary.

While preparing the below manuscript for publication, the KOI-368 system was effectively scooped from us via Zhou & Huang (2013). That work constrained KOI-368's spin orbit angle via gravity-darkening, but their approach (and consequently their result) was quite different from ours. I discuss the differences between the two works in the manuscript.

3.1 Abstract

We fit the *Kepler* photometric light curve of the KOI-368 system using an oblate, gravity-darkened stellar model in order to constrain its spin-orbit alignment. We find

that the system is relatively well-aligned with a sky-projected spin-orbit alignment of $\lambda = 10^\circ \pm 2^\circ$, a stellar obliquity of $\psi = 3^\circ \pm 7^\circ$, and a true spin-orbit alignment of $\varphi = 11^\circ \pm 3^\circ$. Although our measurement differs significantly from zero, the low value for φ is consistent with spin-orbit alignment. We also measure various transit parameters of the KOI-368 system: $R_\star = 2.28 \pm 0.02 R_\odot$, $R_p = 1.83 \pm 0.02 R_{\rm Jup}$, and $i = 89.221^\circ \pm 0.013^\circ$. This work shows that our gravity-darkened model can constrain long-period, well-aligned planets and M-class stars orbiting fast rotators, allowing for measurement of a new subcategory of transiting bodies.

3.2 Introduction

Main-sequence stars earlier than spectral type ∼F6 are expected to rotate rapidly due to their radiative exteriors (Barnes, 2009). This induces the stellar figure to become oblate, which causes the star's photosphere to be up to several thousand Kelvin hotter at the poles than at the equator, leading to higher polar luminosity. This effect, called gravity-darkening, was first predicted by Von Zeipel (1924). Gravity-darkening causes asymmetric light curves for misaligned transiting candidates (Barnes, 2009), and has been used to constrain spin-orbit alignments for significantly misaligned candidates (Barnes et al., 2011). This work will show that this method can also constrain spin-orbit aligned systems with relatively symmetric transit light curves for eclipsing objects.

The measurement of the angle between the inclination of a planet's orbit normal and parent star's spin axis, spin-orbit alignment (φ), can tell us more about the formation and evolution of that system. Evidence shows that a wide variety of planetary system types exist, including many short and long period spin-orbit misaligned planets (Wright et al., 2011; Pont et al., 2010; Triaud et al., 2009; Guenther et al., 2012)[1]. We can use constrained spin-orbit alignments to compare planetary formation of extrasolar planets to that in our own planetary system. We propose an improved method for finding the spin-orbit alignment based off of Barnes et al. (2011), allowing for constraint of previously unmeasurable systems.

There are several existing methods for calculating the stellar obliquity and the sky-projected spin-orbit alignment, including the Rossiter-McLaughlin effect, stroboscopic starspots, Doppler tomography, asteroseismic determination of obliquity and gravity-darkening. The Rossiter-McLaughlin technique uses Doppler shifts in radial velocity measurements during the eclipse of the primary star. (Rossiter, 1924; McLaughlin, 1924).

Stroboscopic starstpots can be used to constrain an aligned system because the planet will cross the same starspot each time the planet transits. However, if the system is misaligned, the planet will cross the starspot very infrequently (Désert et al., 2011), and the method will fall short. Doppler tomography is able to achieve similar results to those possible from gravity-darkening, but this method needs high signal-to-noise radial velocity follow up measurements (Gandolfi et al., 2012). Asteroseismic determination of obliquity can constrain the obliquity, but not the projected spin-orbit alignment (Chaplin et al., 2013), so other measurements are required to find the spin-orbit alignment.

Gravity-darkening constrains *both* the stellar obliquity and the sky-projected spin-orbit alignment simultaneously. Barnes et al. (2011) used gravity-darkening to establish the spin-orbit misalignment in Kepler Object of Interest number 13 (KOI-13) system. Hirano et al. (2012) state that "For such rapid rotators, asymmetries in the transit light curve may be used to determine the parameters only if the spin-orbit angle is large;" however, we show here that we can constrain such rapid rotating systems, even if the spin-orbit angle is small.

In this paper, we show that our gravity-darkened model can constrain long-period, well-aligned planets and M-class stars orbiting fast-rotators, allowing for measurement of a new subcategory of transiting bodies. In §2, we describe our steps for data collection and preparation. In §3, we outline the gravity-darkened model that we use to fit the *Kepler* transit curve, and In §4 we list our constrained parameters for the KOI-368 system. We discuss implications of this work In §5. In §6 we compare our results to Zhou & Huang (2013). This work can be applied to the formation and evolution of intermediate-period planets orbiting fast-rotating stars and eclipsing binary systems; however, actual application of these concepts is beyond the scope of this paper.

3.3 Preparing the KOI-368.01 Light Curve

Borucki et al. (2011) first noted KOI-368.01 as a transiting planet candidate. This KOI is particularly interesting because of the parent star, KOI-368's, early spectral type ($T_{\rm eff}$ = 9257 K); because the star's brightness ($m_{\rm Kepler}$ = 11.375) leads to a high total signal-to-noise ratio (SNR) for the transit (SNR=1866.4); and because of the relatively long orbital period for its companion of 110 days. We summarize the original star and planet candidate parameters in Table 3.1.

More recently, follow-up spectroscopy of KOI-368 from the *Kepler* Community Follow-

up Observation Program (CFOP) showed a high degree of rotational broadening of the stellar absorption lines. That broadening allows measurement of the star's projected rotational velocity, conventionally denoted $v \sin(i)$ ($v \cos(\psi)$ using our parameter definitions, where ψ is the star's obliquity relative to the plane of the sky). The CFOP-measured $v \sin(i)$ value is 90 km/s, as measured by the TRES Echelle Spectrograph of the Smithsonian Astrophysical Observatory. Hence, KOI-368 is a rapid rotator, and may therefore show sufficient gravity-darkening to allow us to measure the relative alignment angle φ between the stellar rotation pole and the orbit normal.

To do so, we first acquire SAP_FLUX photometric timeseries for KOI-368 from the Mikulski Archive for Space Telescopes (MAST) *Kepler* database, including both short-cadence (60 second integration time) and long-cadence (30 minute integration time) photometry. We use *Kepler* Quarter 0 (Q0) through Quarter 16 (Q16) public data, totalling 67601 short-cadence and 60491 long-cadence data points. During Q0-Q7 and Q10-Q16 the spacecraft only used long-cadence for KOI-368, but during Q8 and Q9 it used short and long-cadence mode. When using both the long-cadence and available short-cadence data from Q0-Q16 we keep track of the specific integration time used for each data point.

Transiting planet candidate KOI-368.01 shows a total of 11 long-cadence and 2 short-cadence transits within the 17 quarters. One transit is missing because it is in a data gap. This missing transit is the eighth in the sequence.

We performed several steps to prepare both the short and long-cadence data for fitting. We first normalize each quarter's flux by dividing each point by its quarter's median value. We then glue all short-cadence quarters together and all long-cadence quarters together, and use a median boxcar filter with a period of triple the transit duration (42 hours) to correct for long-term instrument response variations. We show the full processed Q0-Q16 timeseries in Figure 3.1.

We fold the short and long-cadence data sets on their 110-day orbital periods (Borucki et al., 2011) and crop to a window 26.6 hours long centered on the time of inferior conjunction to arrive at a light curve for fitting. We then average the long-cadence data into 30 minute bins and the short-cadence data into 5 minute bins, and combine the two data sets into a single light curve. We perform this binning process to increase computational time; we compared an analytical fit of the binned vs. unbinned data to ensure no vital information was lost. We then clean the data to remove any remaining outliers, and begin the fitting process.

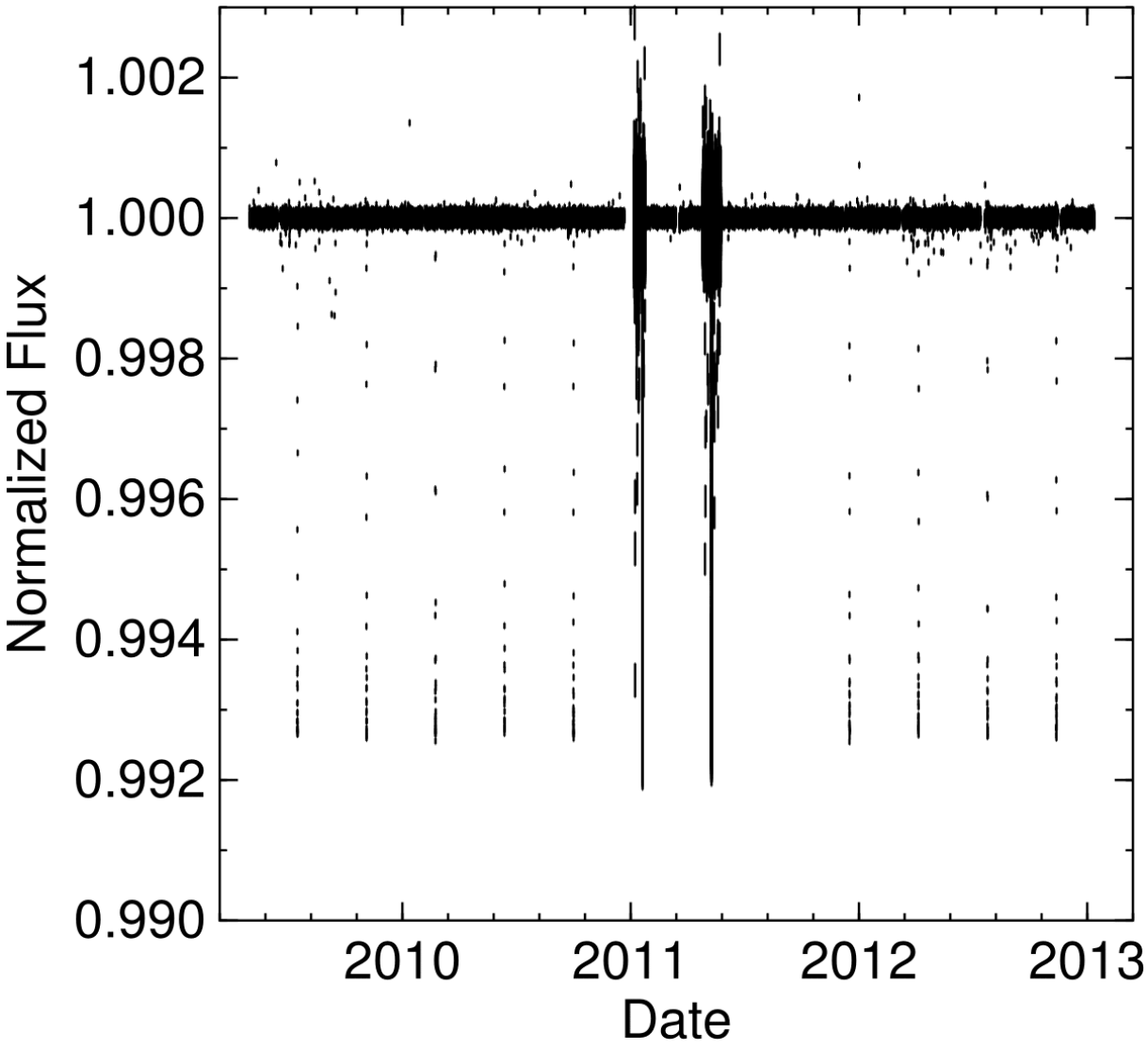

Figure 3.1: A boxcar-filtered version of all of the KOI-368 photometry that we use in this paper, combined into a single dataset before period folding. The vertical extent of each data point indicates its error bar. The noisier data in 2011 correspond to short-cadence observations, which use a time integration of 1 minute rather than the 30 minutes used in the long-cadence observations. The typical photometric precision of the long-cadence data is 4.0×10^{-5}, and for the short-cadence data is 2.3×10^{-4}.

Parameter	Previously Reported Value
T_0	130.6345 days $\pm$0.00015
Period	110.32160 days $\pm$0.00005
a	0.581 AU
$T_{\rm eq}$	754 K
Duration	13.32 h
Depth	7270 ppm
$\frac{\rm d}{\rm R_\star}$	51.19 $\pm$0.14
SNR	1658.2
$T_{\rm eff}$	9257 K
$m_{\rm Kepler}$	11.375
$\log(g)$	4.13
$v \sin(i)$[1]	90 km/s

Table 3.1: Transit parameters provided by the Mikulski Archive for Space Telescopes for the KOI-368 system. The time of transit center is denoted as T_0, the semi major axis of orbit is denoted as a, the equilibrium surface temperature of the planet is denoted as $T_{\rm eq}$, the duration is the transit duration, the depth is transit depth at center of transit, the ratio of the planet-star separation at the time of transit to the stellar radius is denoted by $d/R_\star$, SNR is the signal to noise ratio, the stellar effective temperature is denoted by $T_{\rm eff}$, and the log of stellar surface gravity is denoted by $\log(g)$. [1]From the Kepler Community Follow-up Observing Program, $v \sin(i)$ is the projected stellar rotational velocity.

3.4 Model

We model the KOI-368 transit using an algorithm developed by Barnes & Fortney (2003) and modified to treat rapidly-rotating, oblate stars (Barnes, 2009). The asymmetry of the non-uniformity in flux coming from a gravity-darkened stellar disk drives the use of explicit numerical integrals to compute eclipsed flux rather than an analytical expression (Mandel & Agol, 2002).

Our `transitfitter` program (Barnes & Fortney, 2003; Barnes, 2009) computes this integral for the stellar flux F in polar coordinates R (the projected distance from the center of the star) and θ (azimuthal angle counterclockwise from right) as

$$F = 1 - \frac{\int_0^{R_\star} \int_0^{2\pi} I(r,\theta)\ \Gamma(r,\theta) r\ d\theta\ dr}{\int_0^{R_\star} \int_0^{2\pi} I(r,\theta)\ r\ d\theta\ dr} \tag{3.1}$$

where $I(r,\theta)$ is the flux per unit area of the particular (r, θ) location on the stellar disk, and $\Gamma(r,\theta)$ is a function that denotes the location of the transiting object by yielding 1 for blocked locations and 0 everywhere else. Functionally we evaluate the θ portion of the integral by finding both limbs of the planet at distance r by use of a root-finding routine and then integrating $I(r,\theta)$ between these known limb locations.

We fit this model to the *Kepler* data using a Levenberg-Marquardt χ^2 minimization algorithm (Press et al., 2007). Because of the need for explicit numerical integrals, each fit takes several days to complete.

3.5 Results

We measured seven different parameters for KOI-368 by fitting its *Kepler* transit light curve. We measured the stellar and planet radii ($R_\star$ and R_p, respectively), the inclination of the orbit relative to the plane of the sky, i, the time of inferior conjunction, T_0, the out-of-transit normalized stellar flux, F_0, the sky-projected spin-orbit alignment, λ, and the stellar obliquity, ψ, measured as the tilt of the stellar north pole away from the *Kepler* field of view.

We also derive three parameters based off of our best-fit values. We calculated the impact parameter, b, the stellar rotation period, P_{rot}, and the stellar oblateness $f_{KOI-368}$. The impact parameter was derived using the orbital inclination angle. The stellar rotation period was derived using our assumed $v\sin(i)$ value and the stellar obliquity. The stellar

oblateness was derived from $R_\star$ and P_{rot}. We held our limb-darkening parameter c_1 constant at 0.49, as explained In §5. We list the best-fit and derived values along with their 1σ uncertainties in Table 2.

We display the orbital inclination i, sky-projected spin-orbit alignment λ, and stellar obliquity ψ in Figure 3.2. With the stellar obliquity and sky-projected spin-orbit alignment constrained, we calculated the spin-orbit alignment using

$$\cos(\varphi) = \sin(\psi)\cos(i) + \cos(\psi)\sin(i)\cos(\lambda) \tag{3.2}$$

(Barnes et al., 2011). We calculated its uncertainty using a Monte Carlo numeric error propagator.

Parameter	Best Fit Values
χ^2_{reduced}	1.41
$R_\star$	$2.28 \pm .02$ $R_\odot$
R_p	1.83 ± 0.02 R_Jup
$\frac{R_\text{p}}{R_\star}$	0.0823
i	$89.221^\circ \pm 0.013^\circ$
b	0.697
c_1	0.49
T_0	7520550 ± 40 s
F_0	$1.000024 \pm 5 * 10^{-6}$ s
λ	$10^\circ \pm 2^\circ$
ψ	$3^\circ \pm 7^\circ$
φ	$11^\circ \pm 3^\circ$
P_{rot}	30.73 hr
$f_\star$	0.0275

Table 3.2: Transit parameters for the KOI-368 system. R_p is in units of equitorial Jupiter radii at one bar level. The time at the center of transit, T_0, is measured in seconds after BJD 2454900, after Borucki et al. (2011). Throughout the fitting process, the limb-darkening coefficient and gravity-darkening parameter were held constant at $c_1 = 0.49$ and $\beta = 0.25$ to remove further degeneracies from our model (see Figure 3.4).

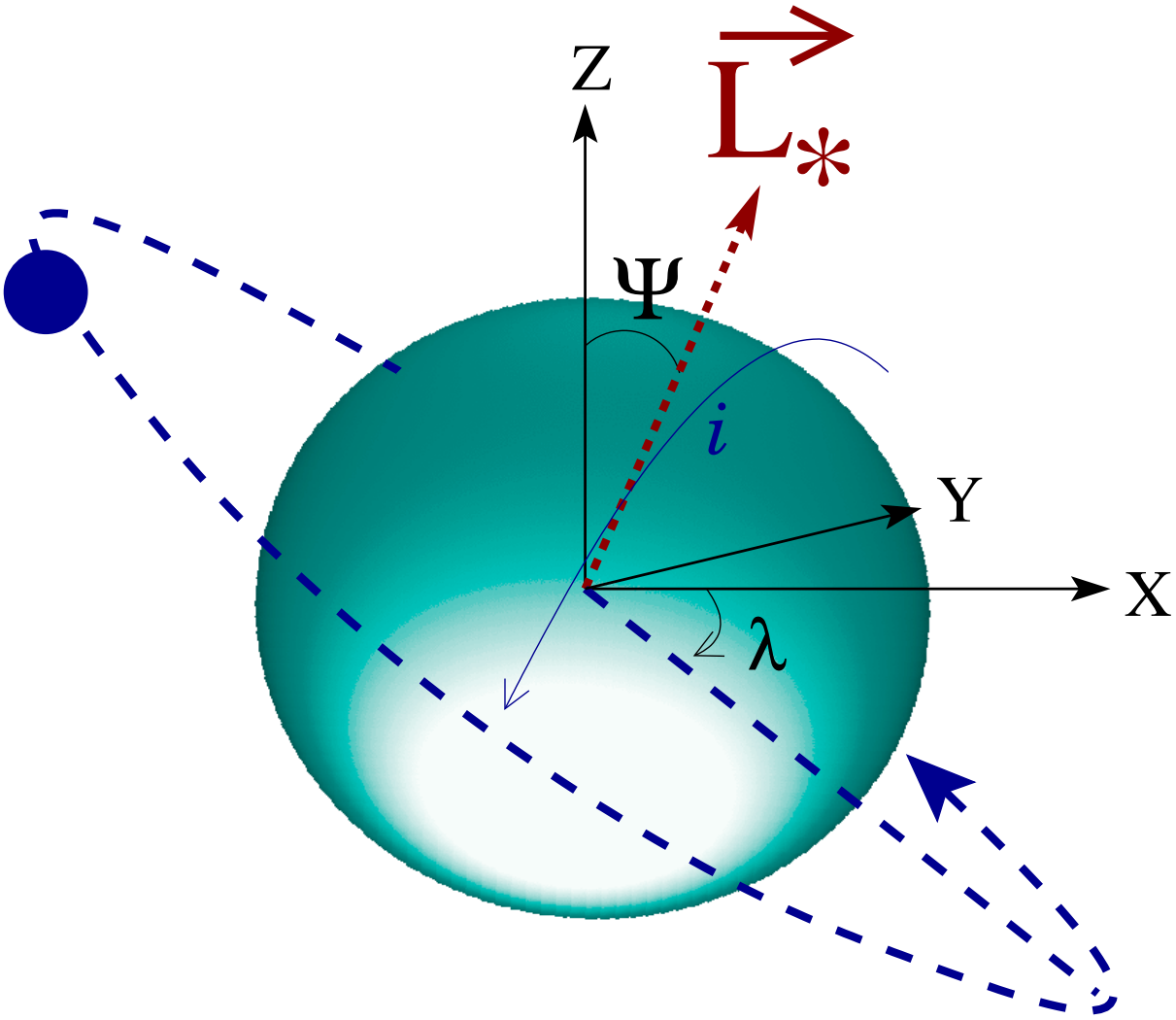

Figure 3.2: Definitions of angular geometric quantities. The planet candidates's projected orbital inclination is i. The candidates's projected spin-orbit angle is λ, as measured clockwise from stellar east. The coordinate system axes are provided, where Y is the direction of the observer's view. The stellar obliquity, ψ, is measured as the angle that the north stellar pole is tilted away from the plane of *Kepler's* view.

The fitted data are plotted in Figure 3.3, along with the residuals. While the light curve appears relatively symmetric, we know that the star is rotating with a $v\sin(i) = 90$ km/s, which implies that there must be some gravity-darkening occurring. It does not show in the light curve due to the transit geometry, which we demonstrate in Figure 3.4.

3.6 Discussion

KOI-368.01 has the longest period of any candidate with measured spin-orbit alignment, and is second overall next to HD 80606 (Pont et al., 2009). Our results show that KOI-368.01 has the longest orbit that has been proven to be spin-orbit aligned (Albrecht et al., 2012), as HD 80606 is misaligned. This work opens up a whole new population of planets that could be studied via gravity-darkening. In particular, we provide a method to determine the possible ways that candidates such as these evolved. It could be that KOI-368 formed in its present location, or it could have migrated inward by some mechanism, while its spin-orbit alignment was left unaffected. This work is the first step in establishing a trend for the evolution and formation of late-type stars, giant planets, and brown dwarfs orbiting hot stars.

Based on how large the $R_\star$ and R_p values are, it is also possible that our fit is assuming that KOI-368.01 was transiting during apoapsis, thus assuming that the candidate was having to transit across a larger star in order to still hold the $v\sin(i)$ at a constant of 90 km/s. We can compensate for this by assuming it is in an eccentric orbit. For instance, with an eccentricity of 0.1, we see an $R_\star = 2.4864 R_\odot$ and $R_p = 2.0435 R_\mathrm{Jup}$. When we assume an eccentricity of 0.3, we see an $R_\star = 3.0633$ and $R_p = 2.5176$. Finally, if we were to assume an eccentricity of 0.5, we see an $R_\star = 3.1374$ and $R_p = 2.4363$. However, for our best-fit model, we assumed negligible eccentricity and assumed the transiting companion to be an M-Dwarf star, following Zhou & Huang (2013).

We represented the stellar limb-darkening with a single limb-darkening parameter, c_1, equal to the sum of the two quadratic limb-darkening parameters such that $c_1 = u_1 + u_2$, following Brown et al. (2001). In our best fit model, we held c_1 constant in order to obtain an accurate measure of the stellar obliquity because if c_1 were allowed to float, the degeneracy between it and the stellar obliquity would cause the stellar obliquity's uncertainty to greatly increase (Barnes, 2009). By holding c_1 constant, we were able to better constrain the stellar obliquity. While fitting, we used assumed c_1 values that varied from 0.43 to 0.56 and found that the best-fit values for the floating parameters varied by

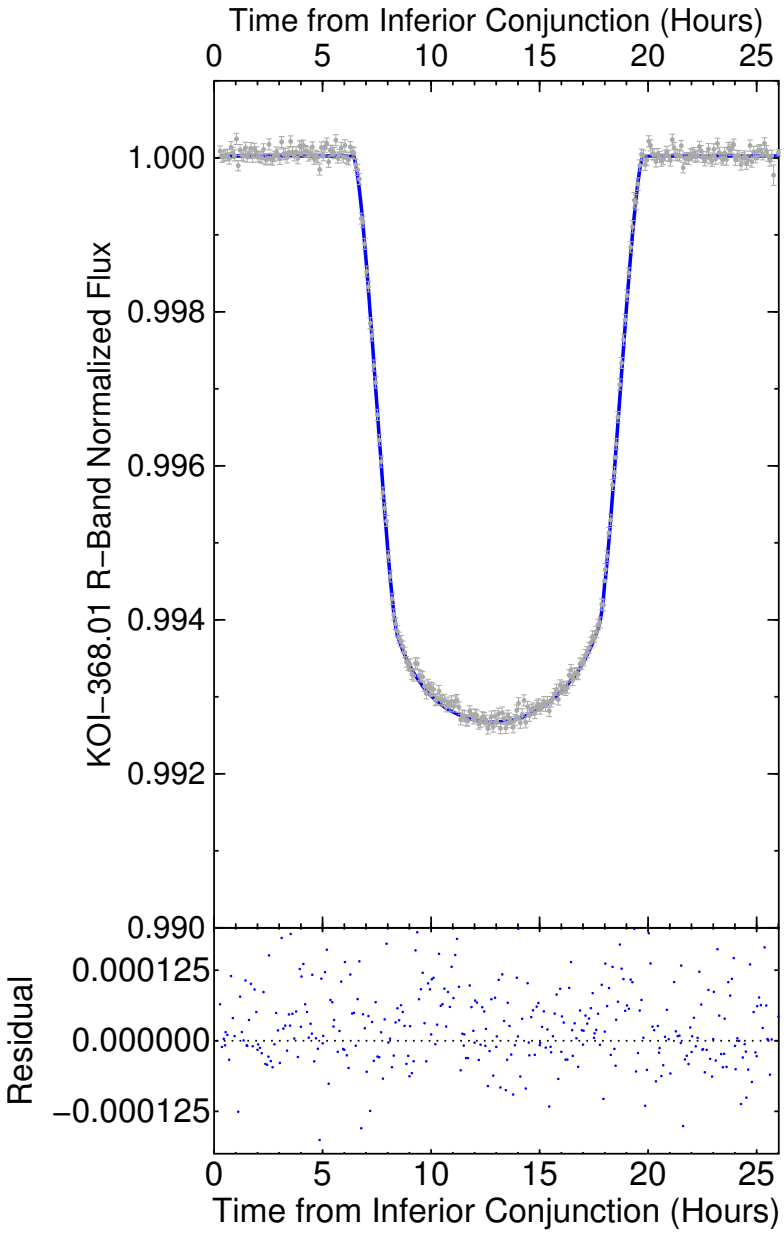

Figure 3.3: Photometry and fits for the 2013 KOI-368 light curve. We plot the data on top with the gravity-darkened fit in blue. The residuals of this fit are shown below. We recognize a slight asymmetry in the light curve, as first identified by Zhou & Huang (2013). Our gravity-darkened model does a reasonable job of reproducing ingress and egress at the bottom of the light curve. The residuals from the fit are shown at the bottom. The gravity-darkened model does a reasonable job of reproducing the ingress and egress at the bottom of the light curve.

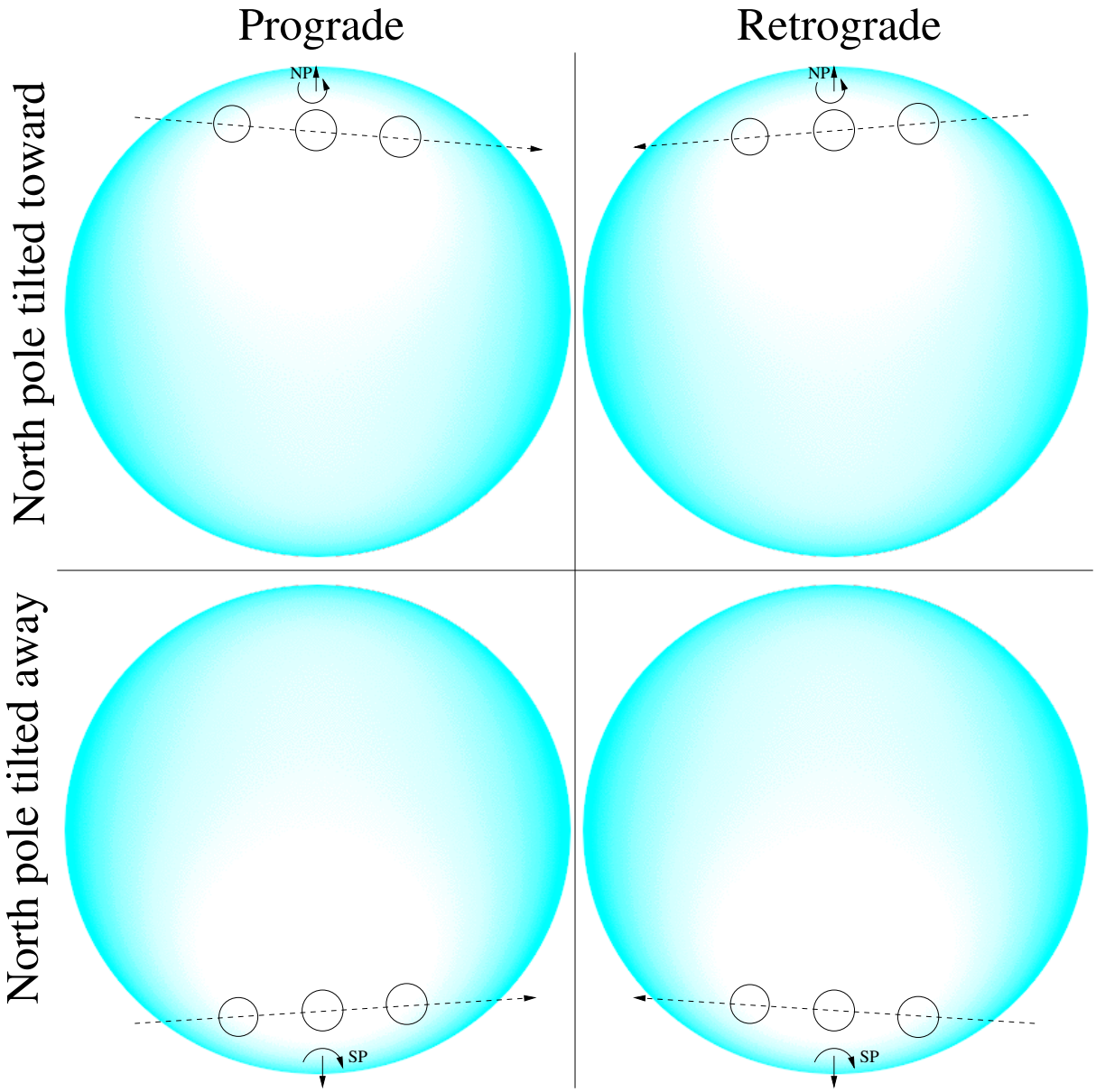

Figure 3.4: The four possible transit geometries of the KOI-368 system. We enhance the effects of gravity-darkening and limb-darkening to make the varying surface luminosity more evident. All four scenarios produce identical transit light curves; therefore, these geometries are perfectly degenerate. This arises from the inability to differentiate between prograde and retrograde values for the sky-projected spin-orbit alignment (λ) and the stellar obliquity (ψ). Conservatively, we assume prograde values with the north pole tilted toward our point of view (upper left image).

less than 1σ. We found that our reduced χ^2 value was lowest at $c_1^2 \approx 0.50$, and thus chose $c_1 = 0.49$ based off of the similarity between the stellar radii and temperatures of KOI-386 and KOI-13 (Barnes et al., 2011).

We intend to use this technique to survey other systems with intermediate period orbits, and attempt to constrain their spin-orbit alignments. This will allow us to see if KOI-368 is a good model for these types of systems, or if it is atypical. As future work we will expand the types of systems we analyze, such as smaller radius exoplanets and multiplanetary systems.

3.7 Comparison To Zhou & Huang (2013)

Zhou & Huang (2013) recently published constraints for the KOI-368 system using a gravity-darkened model, based off of Barnes (2009). However, Zhou & Huang (2013) claims that the KOI-368 system is significantly misaligned (φ=$69^{+9^\circ}_{-10^\circ}$), which is contrary to our result that the system is close to alignment.

This discrepancy may arise from differences between the Zhou & Huang (2013) model and ours. Most notably is our handling of the gravity-darkening parameter (β), which relates the effective local gravity to the effective local temperature of a star by Maeder (2009):

$$T = T_{pole} \left(\frac{g}{g_{pole}} \right)^{\beta} \tag{3.3}$$

β represents the strength of the stellar gravity-darkening: higher β values allow for larger variations in luminosity between the pole and equator given the same stellar parameters. We use $\beta = 0.25$ for our fit, which represents blackbody radiation. Zhou & Huang (2013) used a dynamic fit for β that arrived at $\beta = 0.05$, removing virtually all gravity-darkening effects. With such a low β value, the stellar obliquity and sky-projected alignment can drastically vary without causing significant asymmetry in a best-fit model.

The sky-projected alignment, stellar obliquity, limb-darkening coefficient, and the gravity-darkening parameter are interdependent parameters. *Kepler* photometric data of the KOI-368 system are not sufficiently precise to allow for constraint of all four, so we held β constant at 0.25 and c_1 constant at 0.49 during the fitting process.

To show the effects of β on the fit, we also held β constant at other values and constrained λ and ψ, as shown in Figure 3.5. This figure shows that the sky-projected alignment and stellar obliquity do not vary extensively except at very low values of β.

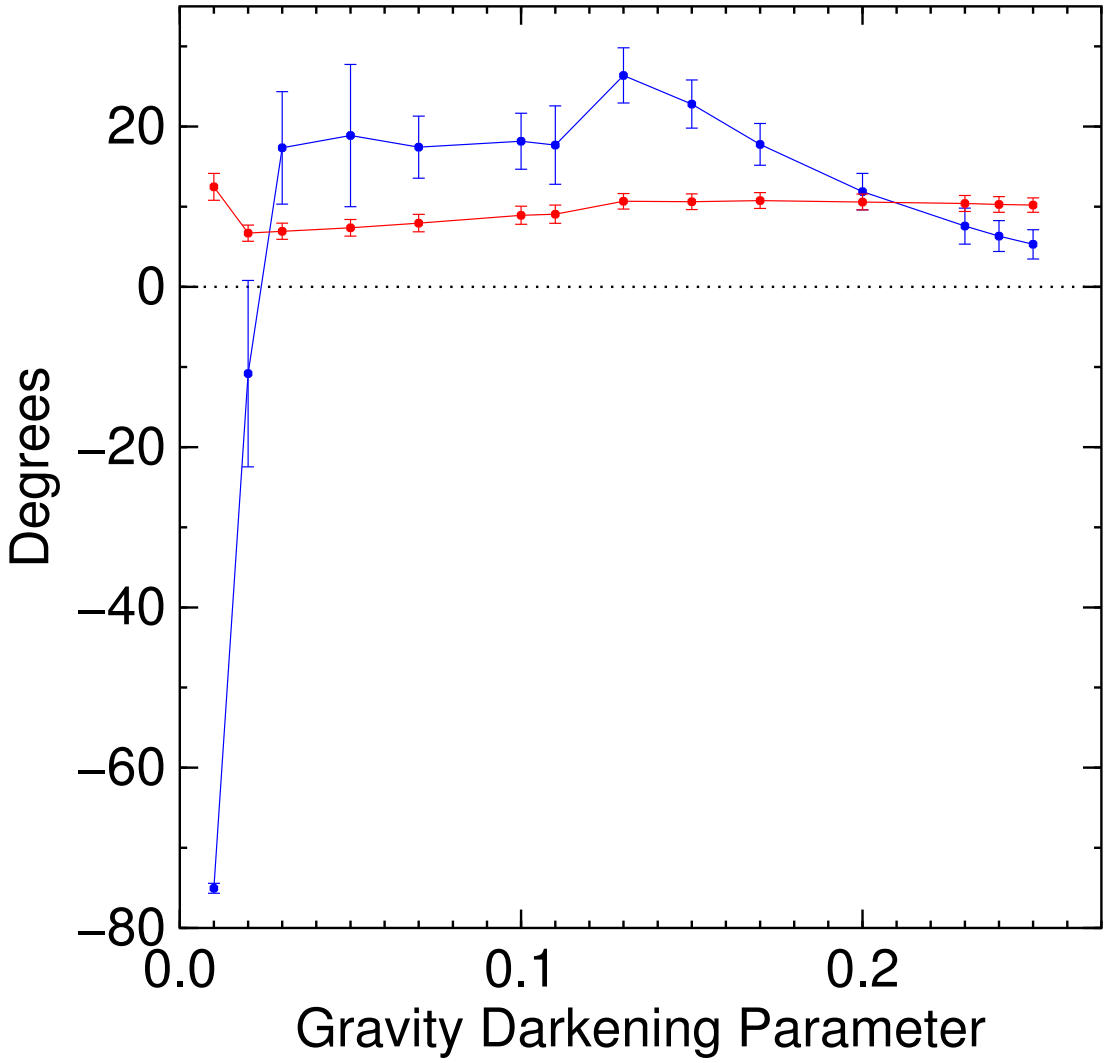

Figure 3.5: This figure shows the β dependence of the sky-projected alignment (in red) and of the stellar obliquity (in blue). Doppler tomography of KOI-368 will determine β, which will allow for better constraint of the spin-orbit alignment. The error bars were determined using constant χ^2 boundaries as confidence limits.

Even at $\beta = 0.05$, we find a relatively aligned system, which is fundamentally different from Zhou & Huang (2013) due to c_1.

Our assumption of $\beta = 0.25$ is based off of Barnes et al. (2011), which compares the best-fit model of KOI-13 using the theoretical value of $\beta = 0.25$ (Von Zeipel, 1924) and the experimental value of $\beta = 0.19$ (Monnier et al., 2007). Barnes et al. (2011) found that the best-fit values varied less than 1σ between the two β values. Barnes et al. (2011) and Figure 3.5 suggest that our gravity-darkened model is not significantly varied for small changes in β. We used the theoretical β value, as there currently is no experimental β value for the KOI-368 system. A better determination of the star's mass could help to constrain β empirically in the future. Various outside measurements would also help to constrain the system, such as a Rossiter-Mclaughlin measurement of the sky-projected alignment, and an asteroseismic determination of the stellar obliquity.

The Zhou & Huang dynamical fit for both limb-darkening and gravity-darkening parameter β represents an overfit to the *Kepler* data for KOI-368. The resulting fit is unphysical and unreproducible given that Zhou & Huang do not report the limb-darkening parameters that they used. Barnes (2009) showed that transits of an aligned planet around a gravity-darkened star lead to anomalies in the best-fit limb-darkening coefficients — particularly the quadratic coefficient u_2.

Our fit is grounded in the Barnes (2009) model, which has been shown to to agree with Doppler tomography in the case of KOI-13 (Barnes et al., 2011; Johnson, 2013). Barnes et al. (2011) constrained the spin-orbit alignment to $\lambda = 24^\circ \pm 4^\circ$, and Johnson (2013) constrained it to be $\lambda = 21.3^\circ \pm 0.2^\circ$. With an outside confirmation of our model, we think that our measurement of KOI-368 is robust. Future Doppler tomography of KOI-368 could confirm our result.

3.8 Conclusion

By fitting all available short and long-cadence *Kepler* photometry for KOI-368.01, we measured a sky-projected spin-orbit alignment of $\lambda = 10^\circ \pm 2^\circ$ and a stellar obliquity of $\psi = 3^\circ \pm 7^\circ$. While the limb-darkening parameter is assumed to be $c_1 = 0.49$ (Barnes et al., 2011), other fits using different assumed c_1 limb-darkening values while holding β constant show that the spin-orbit angle, $\varphi = 11^\circ \pm 3^\circ$, is not substantially affected by plausible limb-darkening variations.

The gravity-darkened model allows for determination of the true spin-orbit alignment

of a system, not just its sky-projected spin-orbit alignment. This work presents one of the first extrasolar systems to have its spin-orbit alignment constrained (Winn et al., 2007; Sanchis-Ojeda & Winn, 2011; Nutzman et al., 2011). The spin-orbit alignment of KOI-368.01 does not suggest that bodies orbiting more massive stars are more likely to be spin-orbit misaligned, contrary to (Winn et al., 2010).

We show that KOI-368.01 is well aligned with a spin-orbit alignment $\varphi = 11^\circ \pm 3^\circ$. KOI-368 is a rapidly rotating star, and therefore the light curve displays the effects of gravity-darkening. However, because our system is well aligned, KOI-368.01 transits across lines of equal brightness; therefore, the light curve displays only nominal asymmetry.

This system could have formed via one of several mechanisms. The most likely is fragmentation, in which the protostellar disc fragments due to rotational instabilities. This mechanism allows for spin-orbit aligned binary systems of less than 1 AU (Bonnell & Bate, 1994). The formation of close-in binary systems is still somewhat unexplained (Bonnell & Bate, 1994; White & Ghez, 2001); the ability to constrain the spin-orbit alignment of such systems will contribute to understanding them.

The unique nature of the KOI-368 system allows for new insight in studying photometric light curves. With the high precision of *Kepler* photometry, we are for the first time able to constrain systems such as these, which provides new understanding of the formation of extrasolar systems. The knowledge we gained from this system will be applicable to a wide variety of transiting objects in the future.

Chapter 4: Spin-Orbit Misalignment of Two-Planet-System KOI-89 Via Gravity-darkening

"Spin-Orbit Misalignment of Two-Planet-System KOI-89 Via Gravity-darkening." *The Astrophysical Journal*, vol. 814, no. 1, 2015, pp. 67-78.

This project, led by me and co-authored by thesis advisor Jason Barnes and Rory Barnes (University of Washington), focused on constraining the formation and evolution history of two-planet-system KOI-89 (now named Kepler-462). Specifically, we measured the spin-orbit alignment values of both planets and tested our results against existing hypotheses to explain misalignment. This work served as one of the only multiplanet systems to date to have its alignment value measured and provided one of the first ever tests of possible misalignment mechanisms.

4.1 abstract

We constrain the true spin-orbit alignment of the KOI-89 system by numerically fitting the two *Kepler* photometric light curves produced by transiting planets KOI-89.01 and KOI-89.02. The two planets have periods of 84.69 days and 207.58 days, respectively. We find that the two bodies are low-density giant planets with radii 0.45 ± 0.03 R_{jup} and 0.43 ± 0.05 R_{jup} and spin-orbit misalignments $72° \pm 3°$ and $73^{\circ+11}_{-5}$, respectively. Via dynamic stability tests, we demonstrate the general trend of higher system stability with the two planets close to mutual alignment and estimate their coalignment angle to $20° \pm 20°$ – i.e. the planets' orbits are misaligned with the star but may be aligned with each other. From these results, we limit KOI-89's misalignment mechanisms to star-disk-binary interactions, disk warping via planet-disk interactions, planet-planet scattering, Kozai resonance, or reorientation of the star's rotation via gravity waves.

4.2 Introduction

Recent studies show that exoplanetary systems around early-type stars display a wide diversity in planet radii, planet densities, periods, eccentricities, and inclinations. (Brandt et al., 2014; Borucki, 2012; Howard, 2013). Exoplanet orbits exhibit a wide variety of spin-

orbit alignments, with highly misaligned and even retrograde orbit geometries (Bourrier & Hébrard, 2014; Albrecht et al., 2012; Winn et al., 2011). At the time of this work, most known misaligned systems are short-period; only HD80806b (Naef et al., 2001), Upsilon Andromedae (Deitrick et al., 2015), and Kepler 56 (Huber et al., 2013) have periods ≥ 10 days.[1] This work adds to the list of long-period spin-orbit misaligned planets KOI-89.01 and KOI-89.02.

There are several methods for constraining a system's alignment, including gravity-darkening (J. Barnes et al., 2011; Ahlers et al., 2014), the Rossiter-McLaughlin effect (Ohta et al., 2005), Doppler tomography (Gandolfi et al., 2012), asteroseismology (Chaplin et al., 2013; Van Eylen et al., 2014), photometric amplitude distribution (Mazeh, 2015), and stroboscopic starspots (Désert et al., 2011; Hirano et al., 2012). We applied the gravity-darkening method first suggested by J. Barnes (2009) and later applied to Kepler Object of Interest (KOI) 13 (J. Barnes et al., 2011) and KOI-2138 (J. Barnes et al., 2015). This method constrains both the star's polar tilt toward/away from the observer (stellar obliquity) and the planet's misalignment angle as seen relative to the observer (sky-projected alignment).

The gravity-darkening effect, first predicted by Von Zeipel (1924), results in a pole-to-equator gradient in stellar luminosity driven by rotation. As an object transits a gravity-darkened star, it can move across areas of unequal brightness; this luminosity gradient can affect the light curve in various ways, depending on its transit geometry (J. Barnes, 2009). J. Barnes et al. (2011), J. Barnes et al. (2013), Zhou & Huang (2013), and Ahlers et al. (2014) all showed that the asymmetry in such light curves (or lack thereof) can be utilized to constrain the spin-orbit alignment of a transiting system.

The causes of frequent misalignment around fast rotators are still under investigation. Planets probably do not form with initially misaligned orbits – their angular momenta must be conserved with the stellar nursery they formed in. In this case, such planets must migrate to their misaligned positions. KOI-89 is one such system that does not conform to the traditional nebular hypothesis with two planets whose orbits are severely misaligned from the spin axis of their host star.

There are several ideas for processes that might create spin-orbit misalignment. Lai et al. (2011) and Spalding & Batygin (2014) demonstrated that magnetic torques can push the stellar spin axis away from the circumstellar disk's angular momentum vector over very long timescales. This would specifically explain spin-orbit migration in very young

systems with low-mass stars ($M_\star \leq 1.3 M_\odot$), where exterior stellar magnetic fields are strongest. Rogers et al. (2012) showed that internal gravity waves can produce angular momentum transport between the convective interior and radiative exterior of early-type stars that turn the stellar spin axis away from the system's invariant plane.

There are also several ideas that explain how spin-orbit migration might develop via more dynamic means. Libert & Tsiganis (2009) discussed Kozai resonance in a 2-planet system and its effects on mutual inclination between the planets. This is almost certainly the origin of misalignment for HD 80806b (Naef et al., 2001). Chatterjee et al. (2008), Ford et al. (2005), Raymond et al. (2008), and Nagasawa et al. (2008) all demonstrated how planet-planet scattering can drive misalignment in a multiplanet system. Levison et al. (1998) showed that planet-embryo collisions during planet formation can lead to high mutual inclination. Terquem (2013), Teyssandier et al. (2013), and Batygin (2012) analyze gravitational disk-warping events that lead to misalignment.

On the observational side, Winn et al. (2010) showed a correlation between hot stars ($T_{\rm eff} \gtrsim 6250$) and misalignment. Batygin & Adams (2013) showed an interdependence between stellar rotation rates and spin-orbit misalignments. These works imply that a large number of planets orbiting early-type stars are commonly misaligned.

Huber et al. (2013) employed asteroseismology to measure the stellar obliquity of multiplanet system Kepler 56 and showed that spin-orbit misalignment is possible in multiplanet systems with low-mass, long-period planets. Benomar et al. (2014) found mild misalignment in Kepler-25 via a joint analysis of asteroseismology, light curve analysis, and the Rossiter-Mclaughlin effect.

This work provides another example of a long-period multiplanet system with significant misalignment: KOI-89. In §4.3, we outline our data preparation process and list previously known system characteristics. In §4.4, we introduce new techniques to the J. Barnes et al. (2011) fitting method. In §4.5, we show our best-fit parameters and constraints on misalignment. We test KOI-89's dynamic stability and constrain the coalignment angle between the two orbits in §4.6. In §4.7, we discuss possible formation and migration mechanisms for the KOI-89 system and test the dynamical stability of the system in order to constrain the planets' mutual alignment.

4.3 Observations

4.3.1 Data Preparation

The Mikulski Archive for Space Telescopes (MAST) Kepler Input Catalog (KIC) provided the *Kepler* photometry that we analyze for the KOI-89 system. We employ each of the 16 available quarters of KIC data, combining them into a single dataset. We incorporate only long-cadence data (30-minute integrations) because both planets have transit durations of over 12 hours. Therefore, ingress and egress are well-sampled by the 30-minute time cadence, and inclusion of short (1-minute) cadence data would not provide additional constraints.

After concatenating all available long-cadence photometry, we apply a median box filter with a window of 44 hours (three times KOI-89.01's transit duration) to reduce long-term astrophysical and instrumental variability. Figure 4.1 displays the filtered time-series. We then identify which transits correspond to which transiting body based on their KIC orbital periods, and separate them accordingly into individual datasets.

We adjust the center-of-transit times of each transit light curve according to their measured transit timing variations (TTV) (Rowe et al., 2014) in our phase-folding process. We perform this adjustment for each measured TTV in Rowe et al. (2014), including thirteen transits for KOI-89.01 and five transits for KOI-89.02. These transits exclude the double transit identified in Figure 4.1.

With all TTV accounted for and the individual transits evenly separated by 84.69 days and 207.58 days, respectively, we fold all KOI-89.01 transits on top of the epoch 34960800$\pm$ 400 s transit and fold all KOI-89.02 transits on top of the epoch 25041400 ± 700 s transit. We then combine the two resulting light curves back in a single dataset. With the *Kepler* photometry represented by a single light curve with two transit events, we bin the data at 15 minutes to improve the computation time of our fit. We determine the error bars of the binned data from the standard deviation of the flux values in the bin.

4.3.2 Previously Measured KOI-89 Parameters

We build our work upon previous research of the KOI-89 system. We obtain the KOI-89 stellar mass, stellar temperature, and transit periods from the Community Follow-up Observation Program (CFOP). Figure 4.2 shows the spectroscopic determination of $v \sin(i)$. We list these and other relevant system parameters in Table 4.1.

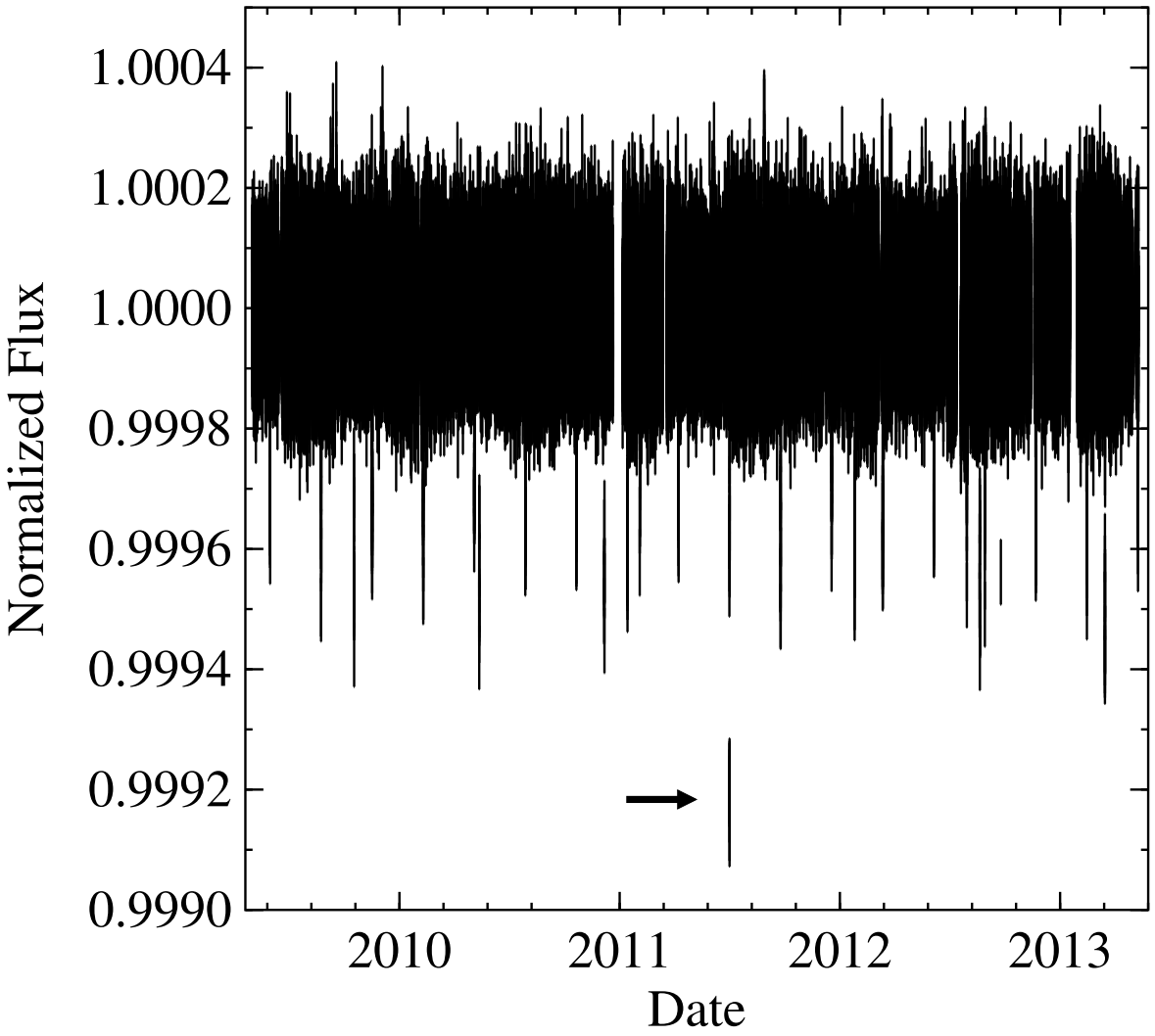

Figure 4.1: *Kepler* photometry of the KOI-89 system. The vertical lengths of the data points represent their uncertainties. Transits of two planets are visible, displaying periodicities of 84.69 days and 207.58 days, respectively. In mid-2011 (arrow), both planets transited simultaneously.

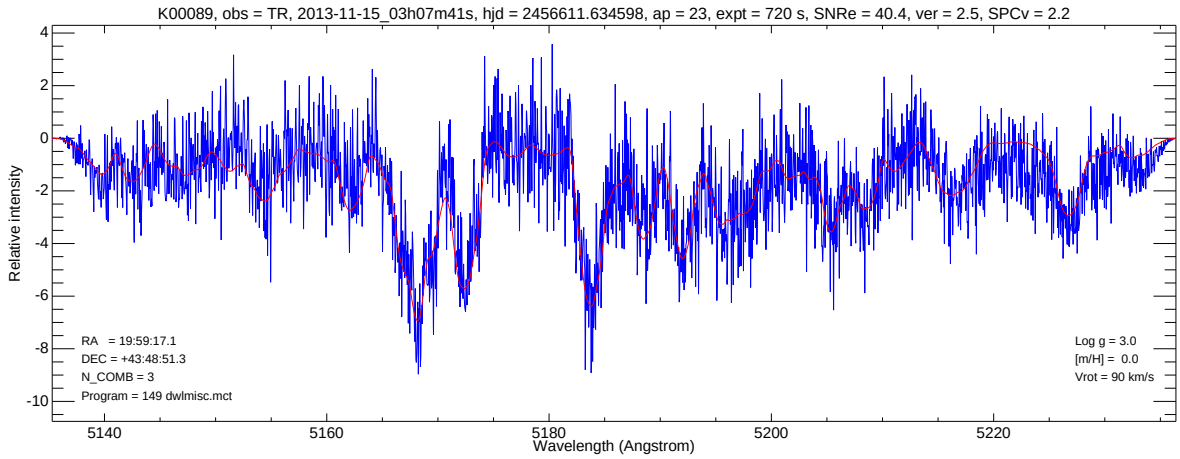

Figure 4.2: Spectroscopic determination of $v \sin(i)$ for the KOI-89 system, measured with the Tillinghast Reflector Echelle Spectrograph on the 1.5 m telescope at the Whipple observatory. These data were provided by David Latham of the *Kepler* Science Team and retrieved from the Community Follow-up Observing Program (CFOP).

Rowe et al. (2014) confirmed 715 new systems – including KOI-89 – via multiplicity. The two planets have a period ratio near the 5:2 mean-motion resonance (2.45). Follow-up observations of these phenomena could confirm/deny the existence of additional orbiting bodies, and could further constrain this system's formation and evolution.

4.4 Model

We update the `transitfitter` program (J. Barnes, 2009) to fit multiple-planet transiting systems. The Levenburg-Marqhardt χ^2 minimization technique remains the fitting method, but now `transitfitter` can constrain the orbital parameters of additional transiting bodies. These extra parameters cause an increased sensitivity to the photometric signal-to-noise ratio, so χ^2 minimization must be approached with additional caution.

The individual parameters of additional planets have the same degeneracies as a single-planet fit. There is a degeneracy between eccentricity and stellar radius, for instance: an eccentric orbit can have the same transit duration as a circular orbit around a smaller star. Also, fitting transit light curves in isolation cannot determine stellar mass, so we apply an assumed stellar mass from CFOP and fit the eccentricity around it. A transit around a fast-rotator has degenerate limb-darkening and gravity-darkening effects in the case of high stellar obliquity. We discuss this degeneracy further in §4.5.

Fitting for both planets simultaneously rather than fitting each light curve separately

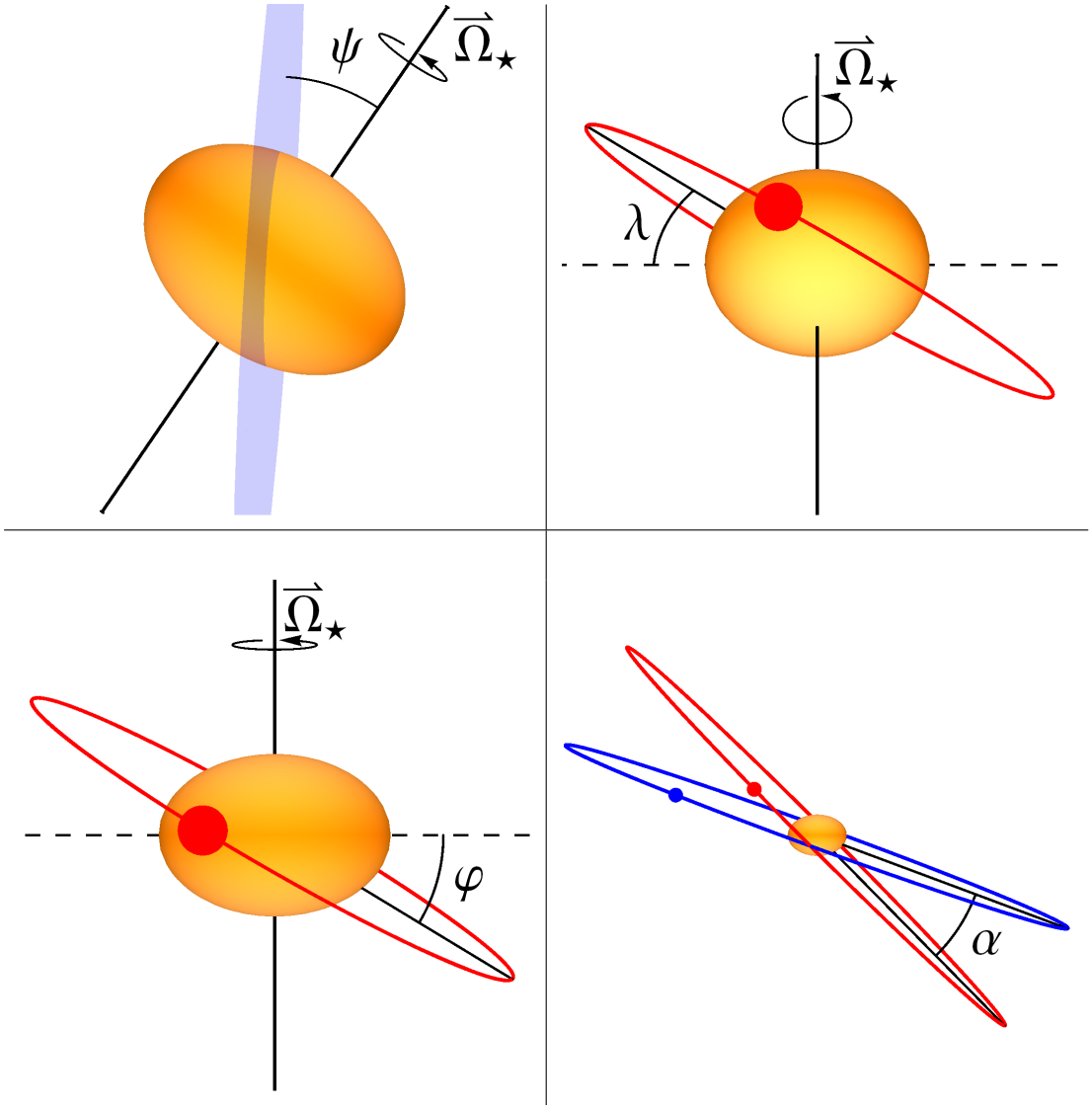

Figure 4.3: Top left: The stellar obliquity ψ is defined as the axial tilt toward/away the plane of the sky. Top right: the sky-projected alignment λ is the misalignment angle seen from *Kepler's* point of view. Bottom left: the spin-orbit alignment φ is the angle between the plane of an orbit and the star's equatorial plane. Bottom right: the coalignment angle α is the angle between two orbit planes.

Parameter	Values
P_1	84.69 days
P_2	207.58 days
$T_{\rm eff}$	7717 ± 225 K
$M_\star$	1.965 ± 0.256 $M_\odot$
$v \sin(i)$	90 km/s
$V_{\rm mag}$	11.731
KOI-89.01 SNR	93.8
KOI-89.02 SNR	68.1

Table 4.1: Previously measured parameters of the KOI-89 system. We incorporated all parameters as assumed values when fitting the KOI-89 light curve.

forces the stellar radius $R_\star$ and the stellar obliquity ψ (shown in Figure 4.3) to agree for both planets, which has two advantages. First, a simultaneous two-planet fit requires two fewer parameters to be fit, increasing the overall accuracy and decreasing computation time of the other parameters. Second, it applies light curve geometries of both planets toward the constraint of $R_\star$ and ψ, producing a coherent physical system. In our fitting model, ψ is particularly sensitive to the light curve geometry; using multiple light curves simultaneously allows ψ to be constrained by more data points, decreasing its uncertainty.

4.5 Results

4.5.1 Light curve Fits

The light curves of KOI-89.01 and KOI-89.02 (Figure 4.4) display unusual shapes. KOI-89.01 has the asymmetry expected of a misaligned body orbiting a fast-rotator (J. Barnes, 2009) . KOI-89.02 does not display this asymmetry, possibly due to lower photometric precision. Both transits show sloped ingresses/egresses and entirely non-constant transit depths, producing dominant V-shaped light curves. A typical light curve is symmetric with a steep ingress and egress with a relatively flat bottom, rounded only by limb-darkening.

KOI-89's V-shaped light curves can arise in one of two ways. First, planets only grazing their star during transit rather than fully eclipsing it block constantly changing

sky-projected areas. This effect creates sloped ingresses/egresses. However, this situation is improbable for KOI-89 as both planets would require similar, high impact parameter values despite having significantly different semi-major axes.

The second way KOI-89 could generate V-shaped light curve geometries is by having a gravity-darkened star with a very high stellar obliquity ψ – i.e. pole-on. In this case, the planets transit near a stellar pole and the gravity-darkened equator surrounds the outer edge of the star. The limb-darkening and gravity-darkening effects combine together to create a significant center-to-edge luminosity gradient. At ingress, the planet blocks a continuously increasing total flux as it moves closer toward the center of the star, and vice versa during egress. This produces a V-shaped transit light curve for each planet (J. Barnes (2009), Figure 4), consistent with the lack of the typical ingress-egress asymmetry expected in a misaligned gravity-darkened transit. We test for the possibility of grazing transits by fitting the system with impact parameters nearly at and slightly above 1.0. We find that we cannot match the system's light curve with grazing transits: such an event can not reproduce the proper ingress-egress asymmetry seen in KOI-89.01.

Figure 4.4 shows our best-fit light curve using grazing transits in blue. We apply grazing transits to both spherical and gravity-darkened models. We hold the stellar obliquity at zero in the gravity-darkened model to test the system for possible spin-orbit alignment. The poor fit of $\chi^2_{\rm reduced} = 1.94$ (adjusted to account for holding the stellar obliquity constant) motivates us to investigate a model with a high stellar obliquity and rapid stellar rotation.

Using the Levenberg-Marqhardt χ^2 minimization technique, we fit for thirteen parameters:

- The stellar equatorial radius ($R_\star$)
- The stellar obliquity (ψ)
- The stellar normalized flux (F_0)
- The radii of KOI-89.01 and KOI-89.02 (R_{p_1}, R_{p_2})
- The orbital inclinations of KOI-89.01 and KOI-89.02 (i_1, i_2)
- The sky-projected alignments (λ_1, λ_2)
- The orbital eccentricities (e_1 , e_2)

- The center-of-transit times (T_{0_1}, T_{0_2})

We display the best-fit light curve of our gravity-darkened model in Figure 4.4 as the red line.

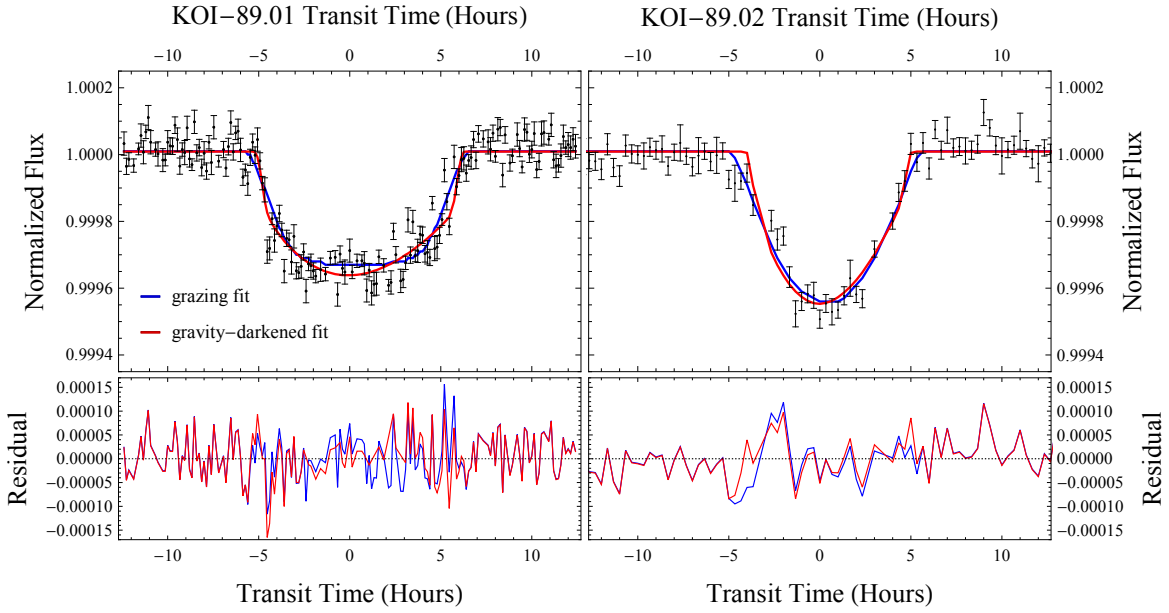

Figure 4.4: Best-fits and residuals of the KOI-89.01 and KOI-89.02 light curves. Red represents the gravity-darkened model, and blue represents grazing transits in the spherical model. The KOI-89.02 data are significantly noisier because of KOI-89.02's much longer orbital period, resulting in fewer total transits. We fit the two light curves simultaneously, resulting in a single best-fit line. The two light curves were placed side-by-side for visual comparison.

4.5.2 Testing For TTV Systematics

We test the *TTV* ephemeris reported in Rowe et al. (2014) for systematic errors by fitting the KOI-89 series as two epochs. The first epoch is comprised of KOI-89.01's first seven transits and KOI-89.02's first two transits. The second epoch is comprised of KOI-89.01's remaining six transits and KOI-89.02's remaining three transits. For each half, we adjust all transits with respect to their *TTV* and fold the transits in the same fashion as described in §4.3.1.

We apply our gravity-darkening model to both epochs and find that the resulting parameters of each fitted dataset have overlapping 1σ values with our best-fit values

Parameter	**Best Fit Values**
$\chi^2_{\rm reduced}$	1.52
$R_\star$	2.3 ± 0.2 R$_\odot$
ψ	$69^\circ \pm 3^\circ$
c_1 (fixed)	0.56
c_2 (fixed)	-0.15
β (fixed)	0.25
F_0	$1.000009 \pm 3 * 10^{-6}$
$P_{\rm rot}$ (derived)	$8.81^{+1.9}_{-1.8}$ hr
$f_\star$ (derived)	$0.19^{+0.04}_{-0.03}$
$R_{\rm p_1}$	0.45 ± 0.03 R$_{\rm jup}$
$R_{\rm p_2}$	0.43 ± 0.05 R$_{\rm jup}$
$e_1 \geq$	0.056 ± 0.019
$e_2 \geq$	0.50 ± 0.09
i_1	$89.340^\circ \pm 0.05^\circ$
i_2	$90.64^\circ \pm 0.06^\circ$
b_1 (derived)	$0.61^{+0.08}_{-0.07}$
b_2 (derived)	$-0.57^{+0.12}_{-0.14}$
T_{0_1}	34960800 ± 400 s
T_{0_2}	25041400 ± 700 s
λ_1	$-32^\circ \pm 11^\circ$
λ_2	$-32^\circ \pm 40^\circ$
φ_1 (derived)	$72^\circ \pm 3^\circ$
φ_2 (derived)	$73^{\circ +11}_{-5}$

Table 4.2: Best-fit results for the KOI-89 system. We calculated stellar period of rotation P_{rot} from $v \sin(i)$, $R_\star$, $M_\star$, and ψ. We derived the stellar oblateness f from the Darwin-Radau relation. The impact parameters b_1 and b_2 were found using P_1 and P_2, i_1 and i_2, and $R_\star$. We set our limb-darkening parameters $c_1 = u_1 + u_2$ and $c_2 = u_1 - u_2$ according to Sing (2010).

using the full timeseries (Table 4.2). We therefore detect no evidence of systematics in the TTV ephemeris listed in Rowe et al. (2014).

4.5.3 Testing Limb-darkening Assumptions

Results fro mthe gravity-darkening technique are especially susceptible to uncertainties in limb-darkening. Via Doppler Tomography, Johnson et al. (2014) measured the sky-projected alignment of KOI-13.01 and found it to differ significantly from the gravity-darkening measurement performed in J. Barnes et al. (2011). Masuda (2015) proposed a solution to this discrepancy by demonstrating that the gravity-darkening model produces concurring measurements with Doppler Tomography when using a nonzero second quadratic limb-darkening term (c_2). This limb-darkening term is also a possible explanation for KOI-368's different spin-orbit misalignment values measured in Zhou & Huang (2013) (Ahlers et al., 2014). These works motivated us to update our gravity-darkening model to include both quadratic terms, c_1 and c_2.

KOI-89's very high stellar obliquity brings about an additional challenge in resolving limb-darkening. With the stellar pole near the center of the sky-projected stellar disk, the gravity-darkening and limb-darkening luminosity gradients behave nearly identically and are essentially additive. The resulting combined effects on a transit light curve are therefore degenerate with a stellar obliquity near 90°.

KOI-89's spectroscopically-determined effective temperature of 7717 ± 225 K corresponds to an approximate range of 0.55 to 0.57 for c_1 and -0.165 to -0.135 for c_2 (Sing, 2010). We test the robustness of our assumed limb-darkening values by refitting using $(0.55, -0.135)$ and $(0.57, -0.165)$ for c_1 and c_2, respectively.

Applying the (c_1, c_2) values $(0.55, -0.135)$, we measure a slight increase in KOI-89.02's impact parameter; however, this increase vanishes when adjusting the gravity-darkening value β to match Altair's value of 0.19 (Monnier et al., 2007). We detect no significant changes in our best-fit results when employing the limb-darkening values $(0.57, -0.165)$. We cannot resolve the accuracy of our limb-darkening parameters without higher precision data, and therefore elect to apply the assumed values of $\beta = 0.25$ (Von Zeipel, 1924) and (c_1, c_2) values of $(0.56, -0.15)$ (Sing, 2010).

4.5.4 Eccentricities

We constrain the lower limits of eccentricity to 0.056 ± 0.019 and 0.50 ± 0.09, respectively. We address the degeneracy between eccentricity and argument of periapsis

following Price et al. (2015). Our eccentricities do not vary significantly for $|\omega| \leq 150°$ away from center-of-transit, consistent with Price et al. (2015) and J. Barnes (2007). To find the lower limit for eccentricity, we set the center-of-transit at periapsis for both planets fit for the eccentricities using our gravity-darkened model. We analyze the plausibility of our eccentricity values in §4.6.2.

4.5.5 Spin-Orbit Alignment

Our gravity-darkened model results in a degeneracy in the sky-projected alignments between the values λ and $180 - \lambda$ (Ahlers et al., 2014). We assume a prograde orbit for KOI-89.01, constraining λ to a single value. This allows us to produce single, nondegenerate values for the obliquity (ψ) and each planet's inclination (i) in our best-fit model, which we allow to float in the full range of $0° - 360°$.

We find that KOI-89 is highly misaligned with a stellar obliquity ψ of $69° \pm 3°$, inclinations i_1 and i_2 of $89.340° \pm 0.05°$ and $90.64° \pm 0.06°$ respectively, and sky-projected alignments λ_1 and λ_2 of $-32° \pm 11°$ and $-32° \pm 40°$ respectively. The high uncertainty of λ_2 is due to the apparent lack of asymmetry in KOI-89.02's light curve because of its photometrically imprecise data. We show our constraint of λ_2 in §4.6, which removes prograde/retrograde degeneracy via dynamic stability tests.

With these constraints we calculate the true spin-orbit misalignments φ_1 and φ_2 from the equation (Winn et al., 2007),

$$\cos(\varphi_i) = \sin(\psi)\cos(i_i) + \cos(\psi)\sin(i_i)\cos(\lambda_i) \tag{4.1}$$

modified for our parameter definitions. We calculate spin-orbit alignment angles of $72° \pm 3°$ and $73^{\circ+11}_{-5}$ for the two planets, respectively. Table 4.2 lists all of KOI-89's parameter constraints.

4.5.6 Double Transit

KOI-89.01 and KOI-89.02 simultaneously transit halfway through 2011, causing a significantly larger transit depth. We indicate this event with the arrow in Figure 4.1 and show the double transit and its synthetic light curve in Figure 4.5. Our best-fit parameters produce a synthetic light curve that adequately models this event. We do not find evidence of a mutual event in the *Kepler* dataset.

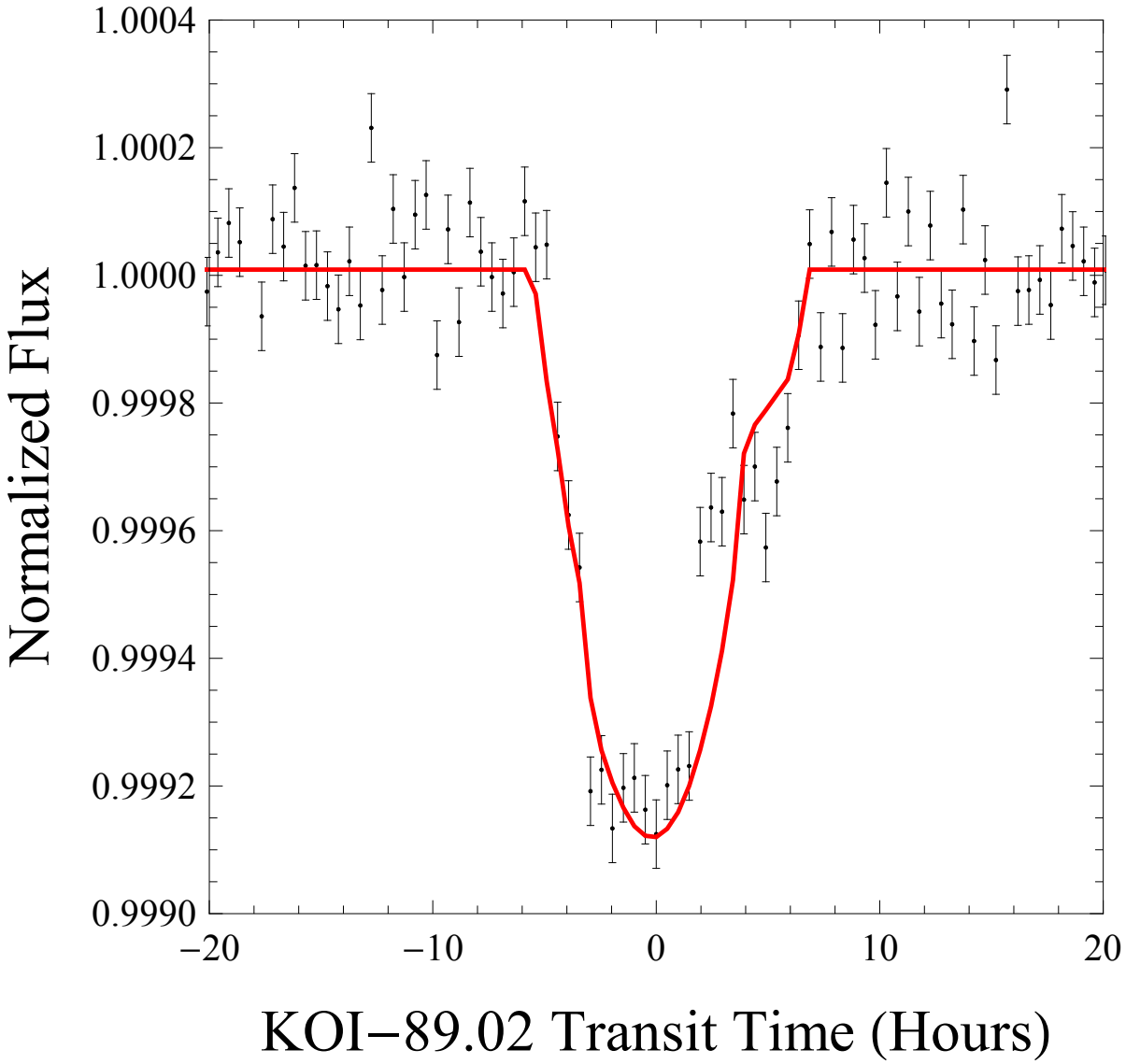

Figure 4.5: Light curve of both planets transiting simultaneously. During the double transit, the depth is roughly double of a typical transit. Our best-fit model (in red) correctly reproduces the time of this event and the general shape of the light curve.

4.5.7 Oblateness

We test the feasibility of KOI-89's oblateness value of $0.19^{+0.04}_{-0.03}$ by analyzing its breakup rotation period,

$$P_{rot} = 2\pi\sqrt{\frac{R_\star^3}{GM_\star}}, \tag{4.2}$$

We find that the star is rotating at $55\% - 76\%$ of its break-up speed by calculating its rotation period, listed in Table 4.2:

$$P_\star = \frac{2\pi R_\star \cos(\psi)}{v \sin(i)}, \tag{4.3}$$

This explains KOI-89's highly oblate shape and its gravity-darkened gradient, which are discussed in §5.3. This star's oblateness is comparable to the fast-rotator Achernar with oblateness ~ 0.36 (Carciofi et al., 2008) or other well-known oblate stars such as Altair (~ 0.2) (Monnier et al., 2007). Hence, our model produces physically plausible stellar parameters.

4.6 Dynamic Stability

4.6.1 Coalignment Integrations

Equation 4.1 gives a planet's spin-orbit alignment φ_i dependence on the sky-projected alignment λ_i. We fit for KOI-89's λ_i in our gravity-darkening model but are unable to resolve λ_2 due to its low photometric resolution and the host star's high stellar obliquity ψ. With gravity-darkening-driven asymmetry absent in KOI-89.02's light curve, we could not fully constrain its transit geometry.

To estimate KOI-89.02's sky-projected alignment, we tested the system for dynamic stability for various transit geometries. Using our gravity-darkening model, we constrained KOI-89's orbital elements with various assumed λ_2 values. We then used the orbit integrator `Mercury` from Chambers (1999) to test each orbit geometry for dynamic stability.

Using `Mercury`, we perform mixed-variable symplectic (MVS) integrations of KOI-89 over 10^8 years using 0.5 day timesteps. Using a spherical star allows for physically sound integrations that obey the conservation of angular momentum with minimal sacrifice; the stellar $J2 \sim 10^{-4}$ value (calculated following Murray & Dermont (2008)), coupled with

the planet's long orbital periods, cause nodal precession on a timescale that would not significantly affect the system's stability. We assume ice-giant densities of $\rho = 1.64$ g/cm^3 for both planets.

We define an angle α of coalignment between the two orbits, defined relative to their angular momentum vectors:

$$\alpha \equiv \cos^{-1}\left(\frac{\vec{L}_1 \cdot \vec{L}_2}{|\vec{L}_1||\vec{L}_2|}\right) \tag{4.4}$$

Figure 4.6 shows the survival time of KOI-89 as a function of the coalignment angle α and conjuction longitude. By varying KOI-89.02's longitude of periapsis, we vary the conjuction longitude between the two planets. We define system instability as a planet ejection or collision event. None of our 360 simulations produced a stable orbit for 10^8 years, indicating we have not found a physically viable system yet. In general, survival times are longer for lower α, but the longest-lived architectures are non-planar.

The coalignment angle α is approximately the difference between the two planets' sky-projected alignment angles. Using the results of our orbital integrations, we estimate the difference between the sky-projected alignment angles $\alpha \approx |\lambda_2 - \lambda_1|$ to be $20^\circ \pm 20^\circ$. This is a conservative estimate based on our results in Figure 4.6; follow-up observations would provide a much better calculation of this parameter.

Our 1332 orbit integrations resulted in a maximum survival time of 5.1×10^7 years. The lack of stable configurations suggests that this system is not yet fully understood. If the system is in resonance and is non-planar, it may evolve chaotically (R. Barnes et al., 2015), and hence long-lived configurations may only exist in small "islands" of parameter space. Alternatively, KOI-89's stability could be brought about by unknown additional bodies in the system. We show in §4.6.2 that KOI-89 could be stable if KOI-89.02's eccentricity is lower than our best-fit value of 0.50 ± 0.09. A better characterization of this system's stability could be understood via *TTV* analysis or Rossiter-McLaughlin measurements, but such work is outside the scope of this project.

4.6.2 Eccentric Integrations

In addition to our coalignment/mean longitude stability tests, we also test the stability of KOI-89.02's eccentricity of 0.50 ± 0.09 in a coplanar configuration. Van Eylen & Albrecht (2015) demonstrated that, in general, multiplanet systems have low eccentricities, making KOI-89 a potential exception to the rule. See §4.5.4 for an explanation of our treatment

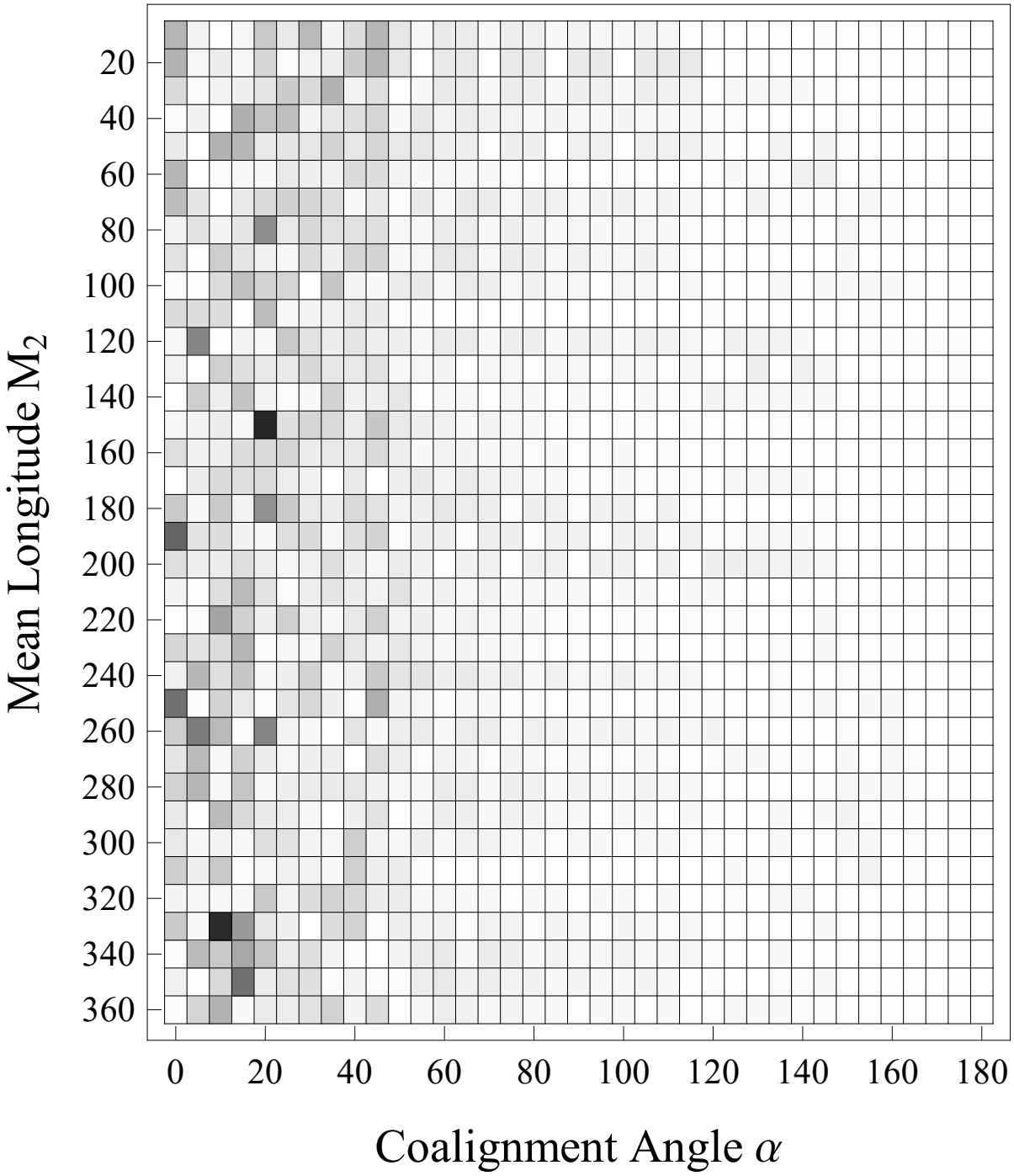

Figure 4.6: Survival times for various initial configurations of the KOI-89 system. Darker color indicates longer survival time, with the longest survival time 5.1×10^7 years. Beyond $\alpha = 20°$, ejection/collision events occur very quickly for all initial configurations, suggesting that the KOI-89 system is more stable near coalignment.

of longitude of periapsis.

We perform a series of integrations in `Mercury` (Chambers, 1999) using assumed e_2 values ranging from 0.0 to 0.95 and a 0.05 step size. All $e_2 \leq 0.35$ are stable, roughly consistent with Petrovich (2015). We show the results of these integrations in Figure 4.7.

Not surprisingly, lower e_2 values yield longer lifetimes and overall higher stability. This result suggests three possibilities. The first (and least likely) possibility is that this system is in fact not coplanar. If the fitted e_2 value of 0.50 ± 0.09 is correct, then perhaps higher stabilities are found in slightly non-coplanar orbits. While higher stability in such a configuration is counterintuitive, it does at least reduce the odds of a close encounter between the two planets, limiting the chances of a violent collision/ejection event.

The second possibility is that our eccentricity measurement contains systematics. A grazing transit would reduce the transit duration time similarly to an eccentric orbit transiting near periapsis, and could produce a V-shaped light curve like we see in Figure 4.4. KOI-89.02's low signal-to-noise ratio, coupled with the degeneracy between impact parameter and planet radius that arises in all grazing transits, prevents us from resolving whether KOI-89.02 is in fact fully eclipsing its host star. KOI-89.02's TTVs could also drive up our eccentricity measurement if they are not fully accounted for (Van Eylen & Albrecht, 2015). High-precision follow-up photometry could better determine KOI-89.02's orbit parameters, including its eccentricity.

The third possibility is that unknown bodies in the system provide stability to these orbits. Antoniadou & Voyatzis (2015) demonstrated that highly eccentric orbits in or near mean-motion resonance can exhibit long-term stability. Additional bodies could help stabilize KOI-89.01 and KOI-89.02, explaining why our best-fit parameters do not display dynamic stability through 10^8 years in our orbit integrations.

4.7 Discussion

The KOI-89 system is highly misaligned with spin-orbit alignment angles of $72^\circ \pm 3^\circ$ and $73^{\circ}{}^{+11}_{-5}$ for the two planets respectively. Our preliminary dynamical analysis of the system §4.6 failed to find a stable solution, so at this time we cannot rigidly constrain the mutual inclination. However, we recognize that survival times are longer in general for lower α.

Of ten misalignment mechanisms suggested in the literature, five are consistent with our results. We rule out the other five mechanisms based on three criteria:

1. Consistency with KOI-89's fundamental parameters such as orbital period, stellar

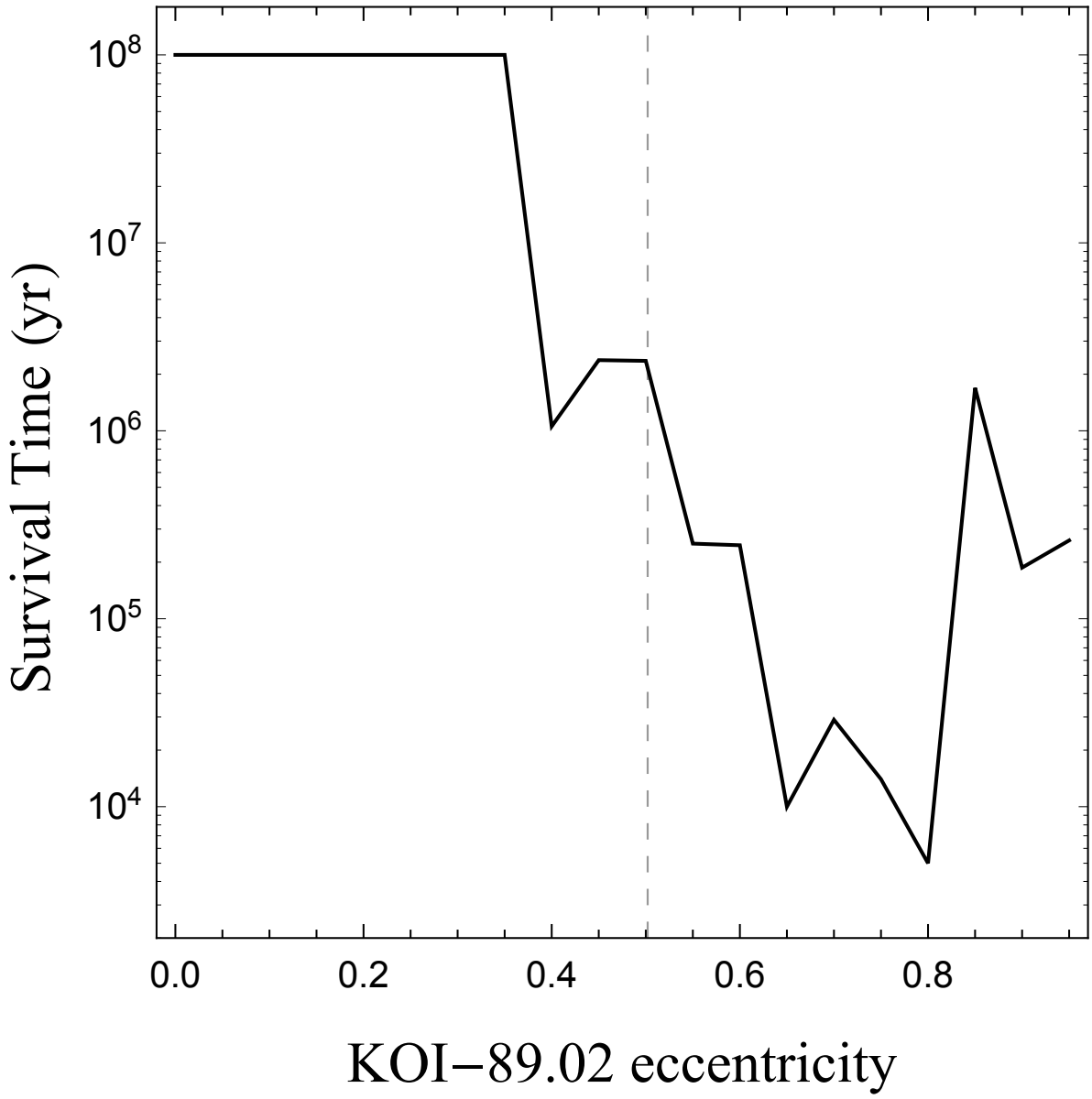

Figure 4.7: KOI-89 survival times using various assumed e_2 values in a coplanar configuration. Our N-body integrations are stable through 10^8 years for all $e_2 \leq 0.35$, which is less than two σ of our best-fit value. The dashed line marks our best-fit value of 0.50 ± 0.09.

radius, etc.

2. The capability to cause extreme misalignment

3. Conformance with mutually aligned planets

We compare our results to each mechanism in Table 4.3.

Mechanism	Relevant Works	Criterion 1	Criterion 2	Criterion 3
Star-disk-binary interactions	Lai (2014), Xiang-Gruess & Papaloizou (2014), Batygin (2012)	Yes	Yes	Inconclusive
Inclination driven by a warped disk	Terquem (2013)	Yes	Yes	Inconclusive
Planet-planet scattering	Chatterjee et al. (2008), Ford et al. (2005), Raymond et al. (2008), Nagasawa et al. (2008)	Yes	Yes	Inconclusive
Kozai resonance	Libert & Tsiganis (2009), Thies et al. (2011), Payne et al. (2010) Kaib et al. (2011)	Yes	Yes	Inconclusive
Internal Gravity Waves	Rogers et al. (2012), Fuller et al. (2015)	Yes	Yes	Inconclusive
Planet-embryo collisions	Levison et al. (1998), Charnoz et al. (2001)	Yes	No	No
Chaotic evolution of stellar spin	Storch et al. (2014), Valsecchi & Rasio (2014)	No	Yes	Yes
Magnetic torquing	Lai et al. (2011), Spalding & Batygin (2014)	No	Yes	Yes
Coplanar high-eccentricity migration	Petrovich (2014)	Yes	No	Yes
Inclination Resonance	R. Barnes et al. (2015)	No	Yes	Inconclusive

Table 4.3: Possible spin-orbit misalignment mechanisms for the KOI-89 system. We list ten possible causes of spin-orbit misalignment that have been put forward in the literature and rule out five of them based on our best-fit results and our estimation of the two planets' orbital coalignment. The three criteria are: (1) consistency with KOI-89's fundamental parameters, (2) the capability to cause extreme misalignment, and (3) the production of mutually aligned planets.

4.7.1 Star-Disk-Binary Interactions

Batygin (2012) first showed that a stellar companion could warp a star's protoplanetary disk into misalignment. Planets could then form in the plane of the disk, resulting in primordial spin-orbit misalignment (Lai, 2014; Xiang-Gruess & Papaloizou, 2014; Batygin, 2012). This mechanism requires a binary companion in the KOI-89 system, which has not been reported, but fundamentally agrees with our results in that it could produce highly misaligned, coplanar orbits.

4.7.2 Inclination Driven By A Warped Disk

A planet in the potential of a warped protoplanetary disk can be driven to very high misalignment values (Terquem, 2013). Teyssandier et al. (2013) found that Jupiter-mass planets misaligned from a warped disk experience dynamic friction that realigns the planet in timescales shorter than the lifetime of the disk. However, Neptune-mass planets can remain misaligned and have their eccentricities driven up by orbital perturbations from the disk's gravitational potential. This mechanism has only been considered for single-planet systems, so criterion 3 is inconclusive. However, this mechanism agrees with the first two criteria and cannot be ruled out based on our results.

4.7.3 Planet-Planet Scattering

Our results cannot entirely rule out planet-planet scattering, which is orbit migration due to close encounters between high-mass objects (e.g. Chatterjee et al., 2008; Ford et al., 2005; Raymond et al., 2008; Nagasawa et al., 2008). With KOI-89's net orbital angular momentum highly misaligned from the star's spin angular momentum, conservation of angular momentum would require additional planet(s) to scatter the two transiting planets. In this scenario it is highly unlikely that the two planets would end up near mutual alignment. However, if a sufficiently large unknown body exists in this system, then our orbit integrations may not accurately represent the system and our coalignment constraint for this system is invalid. We therefore deem this mechanism consistent as a possible cause of KOI-89's misalignment. Further studies of KOI-89's $TTVs$ could confirm the existence of additional planets.

4.7.4 Kozai Resonance

Kozai resonance in the KOI-89 system requires an unknown body that is significantly misaligned with the planets' orbital plane (Libert & Tsiganis, 2009; Thies et al., 2011; Payne et al., 2010). Such an event would likely not produce coplanar orbits for KOI-89.01 and KOI-89.02. However, Kaib et al. (2011) suggests that coplanar, inclined orbits might arise as a result of this mechanism. We therefore deem this method consistent.

4.7.5 Internal Gravity Waves

Rogers et al. (2012) showed that angular momentum transport between the convective interior and radiative exterior of hot, early-type stars can change the observed stellar spin axis, resulting in spin-orbit misalignment. This misalignment mechanism happens independently of orbiting bodies and does not affect coplanarity. The 2-D simulations performed in Rogers et al. (2012) found that this mechanism can occur on a timescale as short as tens of years and can explain retrograde orbits. Whether this mechanism can produce spin-orbit misalignments near 90° is still under investigation.

4.7.6 Planet-Embryo Collisions

Planet-embryo collisions can occur in any standard formation model, and they can drive migration in various ways (Levison et al., 1998; Charnoz et al., 2001). However, this mechanism can produce large spin-orbit misalignment angles only for small rocky bodies and does not apply to the highly misaligned giant planets KOI-89.01 and KOI-89.02. Additionally, this mechanism likely could not produce coplanar misaligned orbits because the collisions driving this mechanism are unique to each planet.

4.7.7 Chaotic Evolution of Stellar Spin

Storch et al. (2014) and Valsecchi & Rasio (2014) demonstrated that strong tidal dissipation can cause chaotic evolution of stellar spin. This mechanism requires hot Jupiters with periods $\lesssim 3$ days. Such a body in the KOI-89 system would have to be drastically misaligned from the plane of the other two orbits; therefore, this mechanism cannot be the standalone cause of misalignment because some other mechanism would have to misalign the hot Jupiter. If there was a non-transiting hot Jupiter that were misaligned, it could torque the star into misalignment with the other planets. If said hot Jupiter fell into its host star because of tidal decay, it could change both KOI-89's rotation axis and rotation

rate (Jackson et al., 2009). However, early-type stars such as KOI-89 are thought to have weak tidal interactions in general (Ogilvie & Lin, 2007).

4.7.8 Magnetic Torquing

Magnetic torquing between a stellar magnetic field and a protoplanetary disk can cause misalignment by torquing the disk away from the star's equatorial plane (Lai et al., 2011; Spalding & Batygin, 2014). KOI-89 is an early-type star with a weak magnetic field (Bagnulo et al., 2002), so this mechanism likely could not cause KOI-89's high misalignment. We note that the magnetic fields of fast-rotators are still under investigation (Ibañez-Mejia & Braithwaite, 2015); a better understanding of these magnetic fields may reveal this to be a possible misalignment mechanism for KOI-89.

4.7.9 Coplanar High-Eccentricity Migration

Coplanar high-eccentricity migration can occur in mutually aligned multiplanet systems with at least one highly eccentric orbit. Secular gravitational effects excite the inner planet's eccentricity to very high values, and planetary tidal dissipation during periapsis reduces the orbit's semi-major axis. This mechanism occurs primarily in the planets' orbital plane, predominantly maintaining the system's original spin-orbit alignment angles (Petrovich, 2014).

4.7.10 Inclination Resonance

If the planets are in resonance and possess a mutual inclination, then the orbital inclinations can be driven to very large values (R. Barnes et al., 2015). In that case we may expect to find at least one planet in a misaligned orbit. This phenomenon can also produce very large eccentricities. However, this mechanism depends on stellar torquing from tidal interactions for both planets to be discovered in a misaligned state. Such tidal interaction is weak around early-type stars (Ogilvie & Lin, 2007). While this is a possible cause of KOI-89's extreme misalignment, it requires an external mechanism to bring about an initial mutual inclination. More work is needed to understand if this scenario is possible and could apply to KOI-89.

4.8 Conclusion

We constrain the individual spin-orbit alignments of multiplanet system KOI-89. With our gravity-darkened model, we found significant spin-orbit misalignment with angles of

$72^\circ \pm 3^\circ$ and $73^{\circ+11}_{-5}$ for KOI-89.01 and KOI-89.02, respectively. We also constrain other fundamental parameters of the KOI-89 system and estimate the mutual alignment between KOI-89.01 and KOI-89.02. We show these results in Table 4.2.

While our measurements alone do not uniquely assign a misalignment mechanism to KOI-89, the large spin-orbit alignment angles φ_i and low coalignment angle α of this system limit the possible mechanisms for planet migration. These values, the measured $TTVs$, the near 5:2 resonance, and the fast rotation of the star itself all imply a dynamic formation history.

KOI-89 is of of particular interest because it can experimentally constrain the numerous outstanding hypotheses that have been proposed to generate misalignment. We limit possible causes to star-disk-binary interactions, disk warping via planet-disk interactions, planet-planet scattering, or internal gravity waves in the convective interior of the star. Follow-up observations searching for additional bodies could provide evidence for any of these hypotheses, including internal gravity waves if no additional bodies are found.

Much could still be learned about the KOI-89 system. Asteroseismic determination of the star's oscillation modes could confirm various stellar properties such as stellar radius, mass, and obliquity. Doppler tomographic observations could constrain the individual ascending nodes of the two planets. Analysis of the TTV could confirm/deny the existence of undiscovered planets in the system. High-precision photometry could better constrain the two planets' eccentricities and impact parameters and help resolve the degeneracy between limb-darkening and gravity-darkening. Any of these follow-up observations would shed new light on the formation of solar systems dissimilar to our own.

The constraints provided in this work add to the sample of known misaligned systems – particularly misaligned multiplanet systems, of which only a small number are currently known. The unique nature of the KOI-89 system provides new insight for studying system formation and evolution. It also adds to the surprising diversity of exosystems discovered to date. Future studies can apply the knowledge gained from this work to a wide variety of misaligned and dynamic systems.

We would like to thank the *Kepler* Science Team for making this work possible – particularly Dr. David Latham for providing the $v \sin(i)$ measurement of this system. JPA and JWB are funded by NASA Proposal #13-ADAP13-213. RB acknowledges support from NSF grant AST-1108882.

Chapter 5: Gravity-Darkened Seasons: Insolation Around Rapid Rotators

"Gravity-Darkened Seasons: Insolation Around Rapid Rotators" *The Astrophysical Journal*, vol. 832, no. 1, 2016, pp. 93-101.

I carried out this sole-author project as a preliminary exploration of the atmospheric and surficial processes occurring on planets orbiting high-mass stars. While studying Kepler-462, I wondered about what it would be like to stand on the surface of one of the planets in that system. I realized that, for those planets, the sun in the sky would change in shape and color throughout their year due to the star's oblate shape and the planets' tilted orbits. This idea struck me as curious, as that situation likely has huge effects on a planet's climate and no previous works had ever explored this idea. I built an insolation model to take a preliminary look at what I call "gravity-darkened seasons"; the following manuscript serves as an introduction to the in-depth planetary science analysis to be done on planets orbiting rapid rotators.

5.1 abstract

I model the effect of rapid stellar rotation on a planet's insolation. Fast-rotating stars have induced pole-to-equator temperature gradients (known as gravity-darkening) of up to several thousand Kelvin that affect the star's luminosity and peak emission wavelength as a function of latitude. When orbiting such a star, a planet's annual insolation can strongly vary depending on its orbit inclination. Specifically, inclined orbits result in temporary exposure to the star's hotter poles. I find that gravity-darkening can drive changes in a planet's equilibrium temperature of up to $\sim 15\%$ due to increased irradiance near the stellar poles. This effect can also modify a planet's exposure to UV radiation by up to $\sim 80\%$ throughout its orbit as it is exposed to an irradiance spectrum corresponding to different stellar effective temperatures over time.

5.2 Introduction

A planet's climate is heavily influenced by the type of star it orbits. For example, stellar type determines a planet's exposure to cosmic rays and UV radiation (Bruzual A & Charlot, 1993; Grießmeier et al., 2009), as well as the system's ice line and habitable zone (Traub, 2011). Planetary atmospheric and climatic behaviors are driven by

insolation patterns, which in the right circumstances can result in seasons unlike any in our solar system. This work models insolation around fast-rotating early-type stars and demonstrates potential effects rapid rotation can have on a planet's climate.

Early-type stars with effective temperatures $\geq$ 6200K possess radiative exteriors and almost no magnetic field. As a result, their primordial rotation rates are not magnetically damped (Albrecht et al., 2012). Early-type stars therefore often rotate rapidly, which induces pole-to-equator temperature gradients of up to several thousand Kelvin (Harrington & Collins, 1968; Frémat et al., 2005). This gradient affects both the star's luminosity and peak emission wavelength as a function of stellar latitude (Von Zeipel, 1924).

When orbiting such a star, a planet's seasonal insolation pattern can strongly vary depending on orbit geometry. Specifically, an inclined orbit results in more exposure to the host star's hotter poles, affecting temperature variations over the course of the planet's year. The pole-to-equator stellar flux gradient, called gravity-darkening, can also affect chemical processes in a planet's atmosphere as it is exposed to irradiance corresponding to different stellar effective temperatures over time. This effect could play a major role in the thermal structure, photochemistry, and photoionization of planetary atmospheres (Lammer et al., 2003; Ribas et al., 2005; Yung, 2005).

Exoplanets orbiting early-type stars are frequently misaligned from their host star's rotation plane (Winn et al., 2010; Barnes, 2009; Ahlers et al., 2014; Ahlers et al., 2015). Therefore, gravity-darkened seasons likely occur on a significant number of exoplanets orbiting early-type stars. Understanding this phenomenon is an important step in revealing exoplanet atmospheric and surficial properties in the regime of early-type systems.

In this Chapter, I demonstrate how spin-orbit misalignment and gravity-darkening can combine to produce unusual seasonal patterns. In §5.2, I derive the insolation model, in §5.3, I calculate the insolation of a spin-orbit misaligned planet orbiting a gravity-darkened star and demonstrates its effects on planet equilibrium temperature and received UV flux, and in §5.4, I discuss implications for climate and atmospheric behavior.

5.3 Model

I model gravity-darkened seasons by including the gravity-darkening effect (Von Zeipel, 1924) in my insolation model and test a planet's insolation in various orbit configurations. I use traditional blackbody radiation as the star's emission function because early-type, fast-rotating stars have radiative exteriors and are well-modeled as blackbody radiators

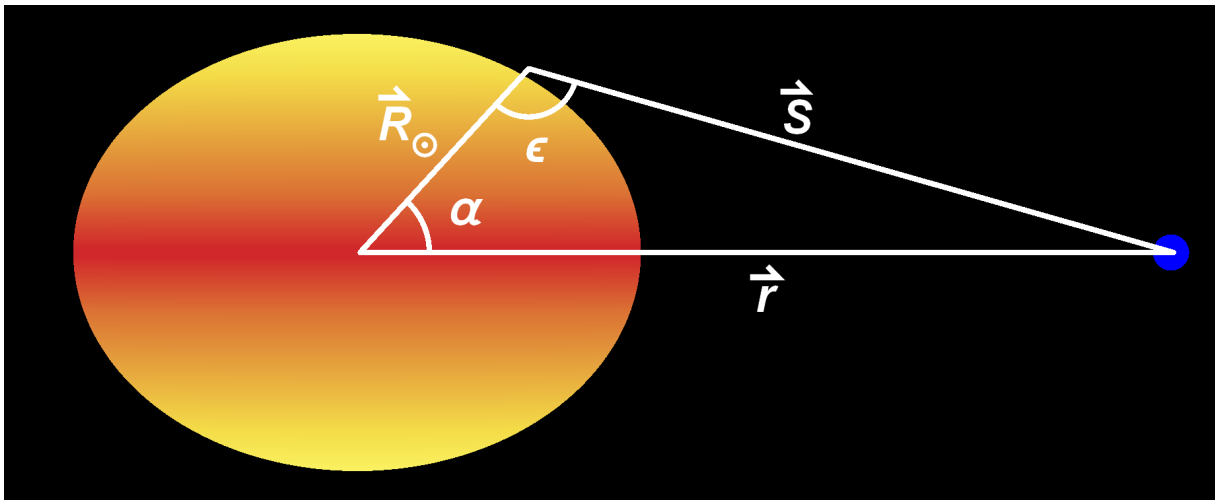

Figure 5.1: Definitions of vectors and angles used in the derivation of Equation 5.1. The stellar surface vector ($\vec{R}_\odot$) is not constant in magnitude due to the star's oblateness. The angle ($\pi - \epsilon$) describes the angle between the planet's line-of-sight vector ($\vec{S}$) a given location on the stellar surface, which appears in the limb-darkening and rectilinear projection terms in Equation 5.1.

(Albrecht et al., 2012). The total irradiance as a function of wavelength on a planet at any given time is,

$$K(\lambda) = \int_\phi \int_\theta B(\lambda, T(\theta)) \frac{I(\mu)}{I(1)} \mu R_\odot \sin^2(\theta) d\theta d\phi \tag{5.1}$$

where $B(\lambda, T(\theta))$ is the stellar emission function, $I(\mu)/I(1)$ is the normalized stellar limb-darkening profile, and μ is a factor to represent the star as a projected disk in the plane of the planet's sky. The integral limits ϕ and θ are traditional azimuthal and polar angles, respectively, with the XY plane defined as the stellar equator. A two-dimensional integral with proper limits of azimuthal angle ϕ and polar angle θ yields the instantaneous stellar output per wavelength as seen by the orbiting planet. I explain how to handle each element of the above equation in the following subsections and in §5.6 and list static values of the model in Table 5.1.

5.3.1 Stellar Emission

The stellar emission function $B(\lambda, T(\theta))$ is the function most appropriate to the star being modeled (e.g. blackbody radiation). The type of emission function in Equation 5.1 can be interchanged straightforwardly because the star's gravity-darkening effect is

handled entirely within the effective temperature function $T(\theta)$.

A star's rotation induces a pole-to equator gradient in effective surface gravity due to centrifugal force. For fast-rotators, the centrifugal force is enough to significantly lessen the effective gravity near the equator, resulting in oblate stars. This change in surface gravity also produces a temperature gradient across the surface, described by the von Zeipel theorem:

$$T(\theta) = T_{\rm pole}\left(\frac{g(\theta)}{g_{\rm pole}}\right)^{\beta} \tag{5.2}$$

where $g(\theta)$ is the effective surface gravity as a function of latitude, $g(0) \equiv g_{pole}$ is the surface gravity at the rotation pole, and β is the so-called gravity-darkening parameter. This parameter is 0.25 for ideal blackbody radiators and decreases toward zero depending on the radial extent of a star's convective envelope. I derive the stellar temperature function $T(\theta)$ in §5.6.1.

Stars of spectral type ∼F6 or earlier are expected to have radiative exteriors and are well-modeled by blackbody emission; hence, $\beta = 0.25$ is a reasonable assumption. However, recent observations suggest that β can deviate significantly from theory. For example, Monnier et al. (2007) measured Altair's gravity-darkening parameter at 0.190 ± 0.012.

5.3.2 Limb-Darkening

Stellar limb-darkening is a brightness effect that stems from the star's optical depth and scale height, which results in the outer limb of a star appearing dimmer than the the center for a given point of view. This effect is well-reproduced with the emperical formula

$$\frac{I(\mu)}{I(1)} = 1 - \sum_{k=1}^{\infty} a_k(1-\mu^{k/2}), \tag{5.3}$$

where $\mu = \cos(\pi - \epsilon)$ describes the angle between the line of sight and the normal vector of the star's surface (see Figure 5.1). The constants a_k represent limb-darkening coefficients unique to each star; however, several works provide estimates of these coefficients as functions of stellar effective temperature (Sing, 2010; Claret & Bloemen, 2011; Claret et al., 2013).

Typically, linear or quadratic approximations of Equation 5.3 are employed in stellar models. As long as μ is known, then any limb-darkening law can be used in Equation 5.1.

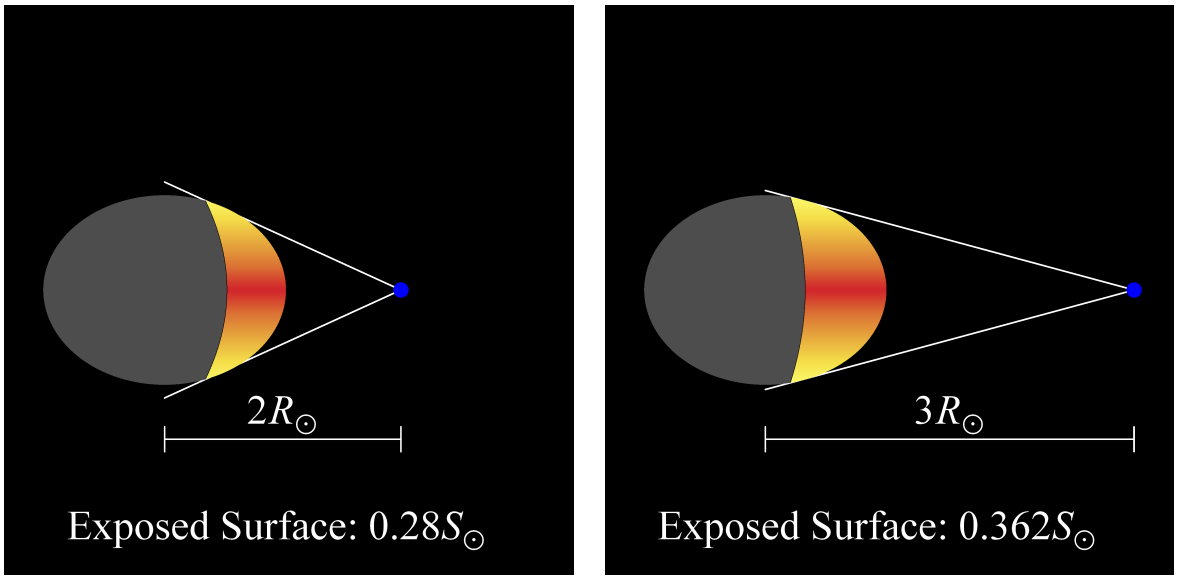

Figure 5.2: Example of how the total stellar surface area exposed to the planet changes for different orbital distances. The colored region of the star represents the area that contributes to the planet's instantaneous irradiance. The border of this area is defined by the region where the line-of-sight vector $\vec{S}$ is tangential to the stellar surface. At $2R_\odot$, the planet is exposed to 28% of the stellar surface ($S_\odot$), and at $3R_\odot$ the planet is exposed to 36%.

I derive μ for my chosen coordinate system in §5.6.2.

5.3.3 Integral Limits

Evaluating Equation 5.1 depends sensitively on the choice of the integral limits (ϕ, θ). The rotation-induced asymmetry of the star adds two-fold difficulty to a traditional insolation model: the star is no longer spherically symmetric and its effective temperature varies as a function of stellar latitude. Figure 5.2 shows how the planet's location in the system determines what part of stellar surface must be integrated. In general, the limits of integration are set by all (ϕ, θ) that satisfy the inequality,

$$\vec{R}_\odot \cdot \vec{r} \geq R_\odot^2 \tag{5.4}$$

which I derive in §5.6.3. This inequality is valid for any position in any orbit configuration, except for the limit of extremely close-in orbits ($r/R_\odot \lesssim 2.2$), where the planet's size becomes relevant in determining insolation by latitude.

5.4 Results

I apply the gravity-darkened insolation model to a synthetic system using the parameters listed in Table 5.1. I demonstrate how gravity-darkened seasons are affected by stellar rotation rate in Figure 5.3. I demonstrate possible seasonal patterns for various orbit configurations in Figure 5.4 and show how the planet's irradiance by wavelength can change in Figure 5.6.

Planets experiencing gravity-darkened seasons exhibit two insolation characteristics unique from planets orbiting solar-type stars. First, nonstandard patterns in the planet's total received solar flux and equilibrium temperature occur throughout its year; the nature of these patterns depends on the planet's inclination and direction of axial tilt, or precession angle. Second, the insolation's spectral energy distribution varies over time due to being exposed to emission corresponding to the hotter stellar poles or cooler equator.

Using a blackbody emission function and quadratic limb-darkening, I find that the equilibrium temperature for a planet on an inclined orbit can vary by as much as $\sim 15\%$ throughout the course of its orbit. This would, for example, correspond to variations in equilibrium temperate between $\sim 300\text{K} - 345\text{K}$ on a planet near the habitable zone. Figure 5.3 shows how stellar rotation rate drives planetary temperature change for inclined orbits. This change in temperature is caused purely by gravity-darkening and stellar oblateness;

Stellar Parameters	**Value**
$M_{\odot}$	2.0 $M_{\star}$
$R_{\rm eq}$	2.1 $R_{\star}$
$T_{\rm pole}$	7700 K
a_1	0.19
a_2	0.36
ζ	0.23
β	0.25
Planet Parameters	**Value**
a	0.5AU
e	0
i	90°
ω	0°
Ω	0°
A	0

Table 5.1: Static parameters (unless otherwise indicated) used when calculating the planet's insolation in Figures 5.3, 5.4, and 5.6. §5.7 lists definitions of all variables. The planet's semimajor axis and inclination and the star's rotation rate are listed with each simulation. The stellar limb-darkening coefficients a_1 and a_2 follow Sing (2010).

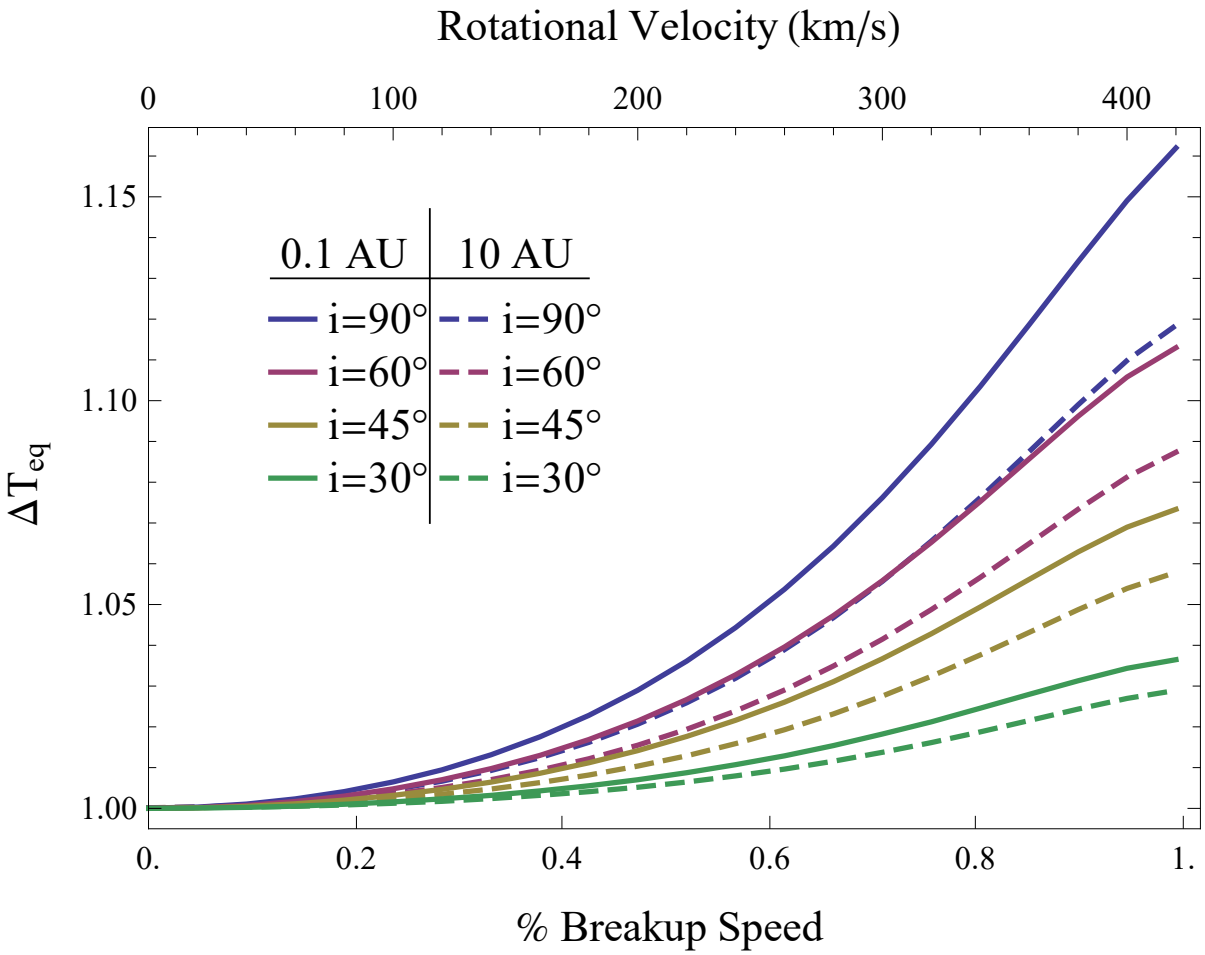

Figure 5.3: Fractional change in the planet's equilibrium temperature versus stellar rotation rate throughout the course of the planet's orbit for various inclinations and orbit distances. The fractional change in temperature corresponds to the planet being primarily exposed to the hotter poles or cooler equator due to its orbit geometry. In general, close-in, highly inclined planets experience the strongest induced temperature changes, but even modestly inclined planets in the outer solar system can undergo significant temperature variations. Early-type stars frequently rotate near their break-up speed; for example, Vega and Regulus both rotate at near 90% of their break-up speeds (Yoon et al., 2010; McAlister et al., 2005).

effects such as planet albedo or orbital eccentricity were not considered in this study.

The gravity-darkening effect can combine with traditional seasonal effects brought about by a nonzero planet obliquity, resulting in more complex seasons. Traditionally, a planet's obliquity causes more/less light exposure for a given latitude throughout its orbit. However, planets on inclined orbits around gravity-darkened stars receive more total irradiance each time they pass over one of the stellar poles – twice per orbit. Gravity-darkening produces planetary temperature changes at twice the frequency of the planet's traditional seasons. These two effects combined can result in unusual seasonal behaviors (Figure 5.4). I compare gravity-darkened seasons with obliquity-driven seasons in Figure 5.5 and derive the relevant calculations in §5.6.5.

The rotation-induced temperature gradient across the stellar surface results in the planet receiving different emission intensities throughout its orbit. This shift is especially evident in the ultraviolet for early-type stars. Figure 5.6 displays an inclined planet's normalized wavelength-dependent insolation when exposed to the stellar equator and stellar pole.

5.5 Discussion & Conclusion

5.5.1 Climate Effects

The equilibrium temperature of an inclined planet around a gravity-darkened star can vary by as much as $\sim 15\%$ throughout its year due to changing total solar irradiance. This effect is additive with traditional seasons – hemispherical temperature changes brought about by a planet's obliquity. Traditional seasons occur once per orbit, but gravity-darkened seasons occur twice per orbit – how these two effects coincide plays a large role in determining the planet's seasonal behaviors.

Ultimately, the nature of gravity-darkened seasons is driven by the phase difference between the planet's precession angle and longitude of ascending node. If traditional summer/winter occurs near the stellar poles, the planet experiences hot summers and mild winters. If traditional summer/winter instead occur near the stellar equator, mild summers and extreme winters occur, with unusually warm spring/autumn seasons. In fact, Figure 5.3 shows that the gravity-darkening effect can overpower seasonal temperature changes caused by obliquity such that traditional spring and autumn are hotter than a hemisphere's summer, producing two distinct peak heating seasons.

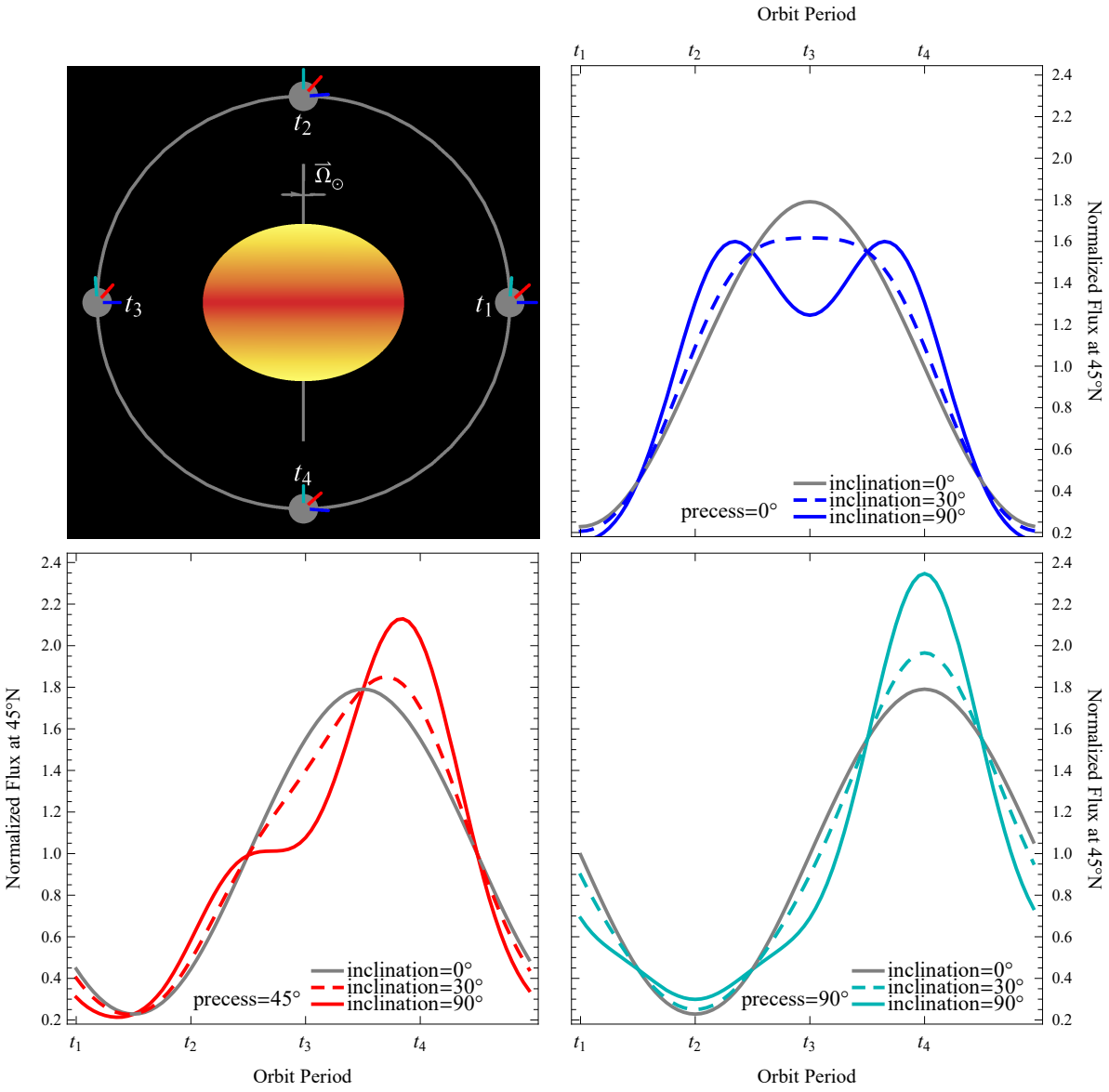

Figure 5.4: Insolation at 45° north latitude throughout an orbit for different precession angles. The blue, red, and cyan plots respectively correspond to precession angles of 0°, 45°, and 90° relative to the planet's longitude of ascending node. All three configurations have obliquities of 30° and include gravity-darkening induced changes in flux for orbit inclinations of 0°, 30°, and 90°. For all configurations, variations away from traditional insolation patterns scale with inclination and stellar rotation rate (see Figure 5.3). The different precession angles produce significantly different seasonal patterns due to combining with the gravity-darkening effect at different phases. A precession angle of 90° results in mild winters and extreme summers, while a precession angle of 0° produces mild summers and extreme winters and, at high inclinations, two distinct hottest times of the year. Figure 5.5 demonstrates the effect of multiple insolation peaks at different planet obliquities.

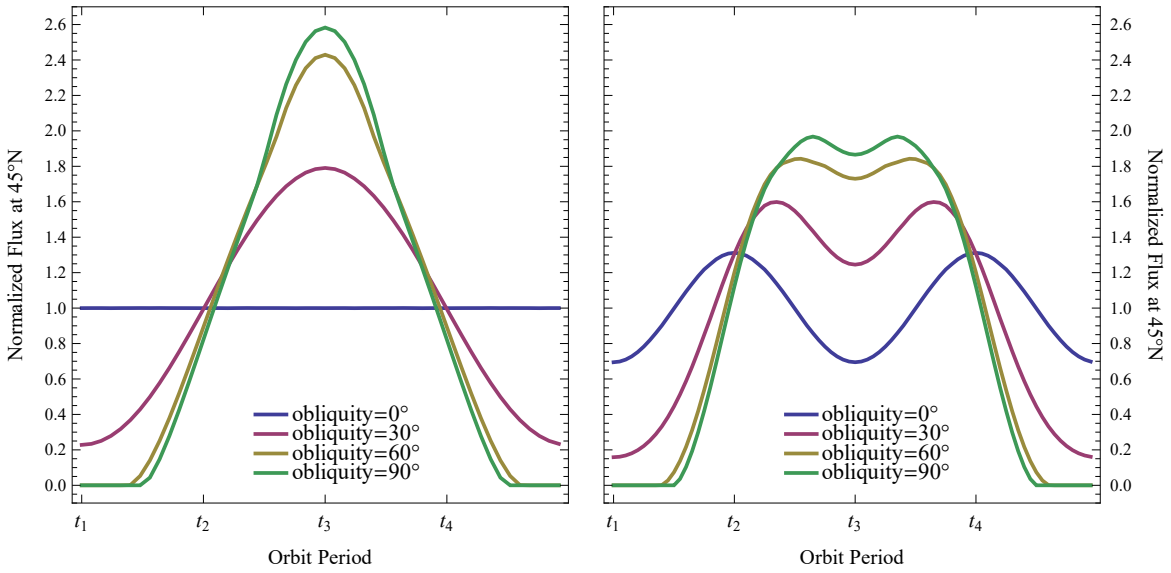

Figure 5.5: Annual normalized flux at 45° North latitude excluding (left) and including (right) gravity-darkening effects. Both plots include yearly insolation values with respect to 0°, 30°, 60°, and 90° planet obliquity values. For both sets of integrations, I set the planet's precession angle at $\rho = 0°$ and inclination at $i = 90°$ (see Figure 5.4). The left plot shows traditional insolation patterns around a spherically symmetric star. The right plot demonstrates that gravity-darkened seasons occur at all obliquity values. At low obliquities, irradiance varies as a sinusoid, effectively producing seasons at twice the orbit frequency.

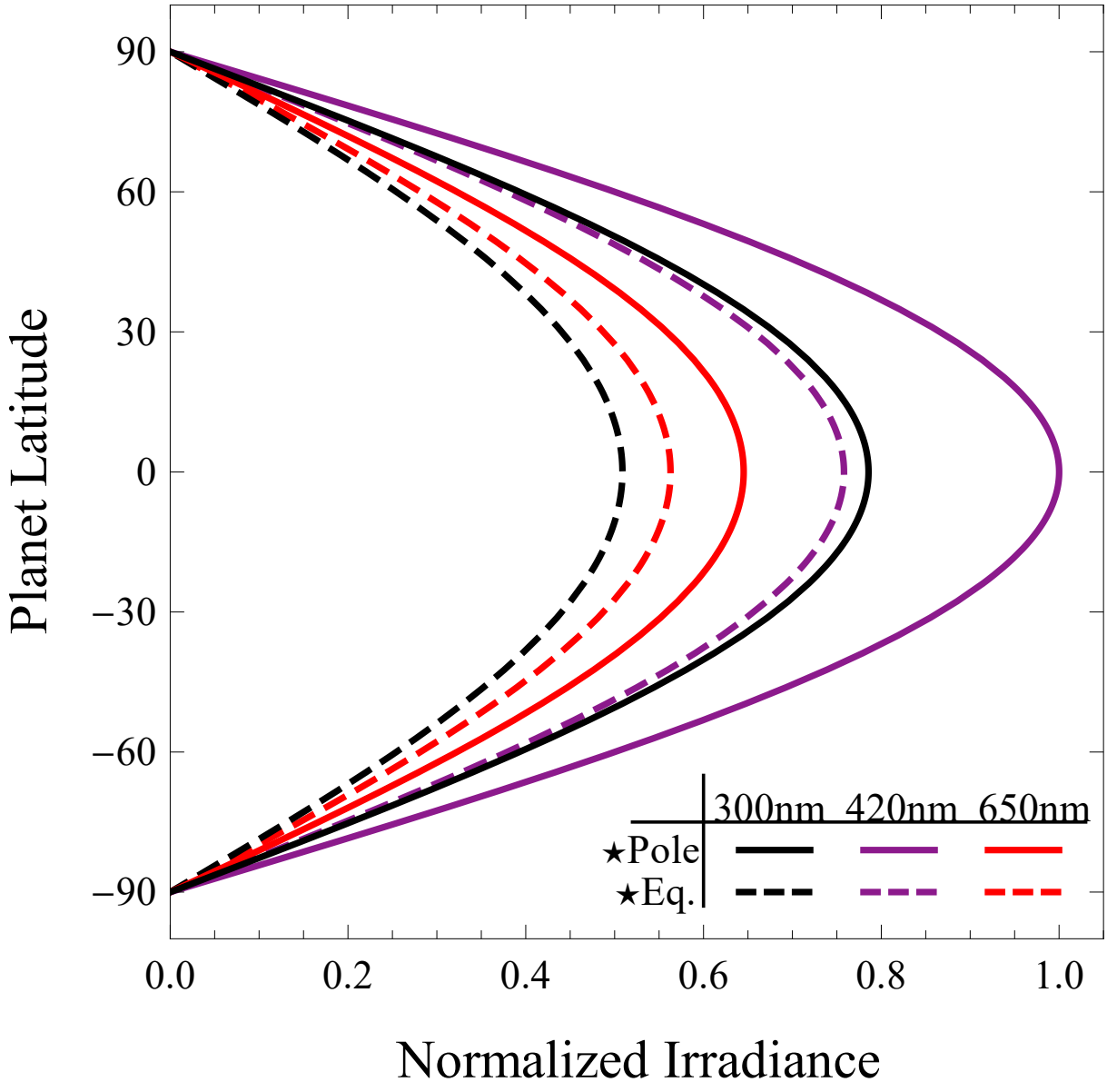

Figure 5.6: Normalized irradiance across the surface of a planet undergoing gravity-darkened seasons. The solid and dashed lines show irradiance by planet latitude when closest to the stellar pole and stellar equator, respectively. The incoming stellar flux is less at all wavelengths when the planet is near the stellar equator. The most drastic change in flux is in UV wavelengths, where intensity can change by as much as 80% throughout the planet's orbit. These changes in UV irradiance occur at twice the orbit frequency.

This temporal heterogeneity in total solar irradiance would likely drive radiative forcing on an Earth-like planet, directly impacting its sea surface temperature and hydrological cycle. For example, as the climate warms, its atmosphere would hold more water vapor, increasing greenhouse gases and further increasing the planet's temperature (Held & Soden, 2000; Forster et al., 2007). The reverse would hold true when the climate cooled. Changes in total irradiance could also affect giant planet deflation/inflation rates (Podsiadlowski, 1993; Fortney et al., 2011). This starkly contrasts with insolation in our solar system, where total solar irradiance varies by only $\sim 0.2\%$ over 11-year cycles (Haigh, 2007).

The equilibrium temperature changes due to gravity-darkening shown in Figure 5.3 are maximum values – in reality, this effect would be mitigated by the planet's albedo, thermal inertia, and atmosphere. The planet would likely not be able to circulate heat globally as quickly as its total irradiance changed, especially for close-in planets. For example, 55 Cancri e is an exoplanet with observed poor global heat transport (Demory et al., 2016). However, the general trends in Figure 5.3 would still be driven by the planet's changing exposure to sunlight intensity.

Figures 5.4 and 5.5 demonstrate how a planet's precession angles and obliquities can affect seasonal insolation patterns when orbiting a gravity-darkened star. These values can change throughout a planet's lifetime. For example, Earth's rotation axis precesses every 26,000 years and oscillates in magnitude every 41,000 years (Lissauer et al., 2012; Barnes et al., 2016a). A spin-orbit misaligned planet undergoing these changes in axial tilt would be driven through the different insolation scenarios in Figure 5.4 on its precession timescale. Obliquity variations could drive Milankovich cycles whose nature depends on orbit geometry. Future studies of these phenomena could help reveal planetary processes driven by gravity-darkened seasons for the first time.

Recent works on habitable planet Proxima Centauri b (Anglada-Escudé et al., 2016) offer a path for characterizing exoplanets in detail. By constraining the planet's formation and migration history, high-energy irradiance, incoming stellar particle winds, and tidal interactions, along with the host star's evolution history, one can estimate the planet's atmospheric loss rate, its water budget, and its overall climate regime (Ribas et al., 2016; Turbet et al., 2016). Barnes et al. (2016b) and Meadows et al. (2016) demonstrate that a planet's geologic behavior can be explored by modeling its orbit evolution and tidal history, as well as heavy element abundances in the planets core. Such works provide

possible next steps toward characterizing the nature of exoplanets in early-type systems.

5.5.2 Atmospheric Effects

Figure 5.6 shows how the irradiance by wavelength on a spin-orbit misaligned exoplanet orbiting a gravity-darkened star can vary throughout its orbit. These changes occur at all wavelengths, with the strongest variations occurring at wavelengths lower than the peak emission wavelength (near UV-violet for early-type stars). The total UV irradiance can vary by as much as 80% throughout an exoplanet's year, with the changes occurring near-sinusouidally at twice the orbit frequency.

Variations in a planet's UV irradiance play a significant role in its photochemistry (Forster et al., 2007). UV light drives the production of ozone in the Earth's stratosphere (Caldwell & Flint, 1994). UV irradiation also plays a significant role in the atmosphere of Saturn's moon Titan, driving much of the organic chemistry in its atmosphere and producing large amounts of aerosols (Szopa et al., 2006). Extreme UV irradiation can drive loss processes in an exoplanet's atmosphere. Hydrogen-rich exoplanets under extreme ultraviolet radiation may evaporate down to their cores (Lammer et al., 2003).

Forster et al. (2007) shows how even very small changes in UV irradiation on the Earth can have significant impacts on the structure of its atmosphere. Gravity-darkening can cause massive changes in UV irradiance throughout an inclined planet's orbit; future photochemical and radiative tranfer models could reveal the full impact of gravity-darkening on a planet's atmopshere.

5.5.3 Conclusion

With rapid stellar rotation and planet spin-orbit misalignment common in early-type systems (Winn et al., 2010; Albrecht et al., 2012), gravity-darkened seasons likely occur in a significant number of exoplanets. This work quantifies how this phenomenon scales with stellar rotation rate, planet inclination, and semi-major axis and shows that a planet's equilibrium temperature can nominally vary by as much as 15%.

Such a planet's total solar influx varies at twice its orbit frequency. This work shows how traditional seasons caused by planet obliquity can combine with its changing irradiance and demonstrates how planet obliquity and gravity-darkening can combine to produce unusual seasonal patterns. In early-type systems, these effects are strongest in UV irradiance, which can have profound impacts on a planet's atmosphere.

The insolation patterns modeled in this work represent a preliminary investigation into

the nature of planets orbiting fast-rotating stars. As planet detection and characterization techniques improve, more and more planets undergoing gravity-darkened seasons will likely be revealed. Future atmospheric models could reveal how gravity-darkened seasons can affect a planet's climate and photochemistry, shedding new light on planets orbiting stars dissimilar to our own.

5.6 Derivations

5.6.1 Effective Temperature Function

To second order, the stellar effective surface gravity is the gradient of the total surface potential,

$$\vec{g} = -\vec{\nabla}\left[\frac{-GM_\odot}{R_\odot}\left(1 - \frac{J_2 R_{eq}^2 P_2(\mu)}{R_\odot}\right) - \frac{1}{2}\Omega_\odot^2 R_\odot^2 \sin^2(\theta)\right] \tag{5.5}$$

where R_{eq} is the star's equatorial radius, J_2 is the second-order gravitational harmonic term dictated by the star's oblateness, $P_2(\mu)$ is a second-order Legendre polynomial, and Ω is the star's rotation rate. This gradient produces a two-component vector:

$$\vec{g} = g_r \hat{r} + g_\theta \hat{\theta} \tag{5.6}$$

Converting these terms to Cartesian coordinates,

$$\begin{aligned} g_x &= g_r \cos(\phi)\sin(\theta) - g_\theta \sin(\theta) \\ g_y &= g_r \sin(\phi)\sin(\theta) + g_\theta \cos(\theta) \\ g_z &= g_r \cos(\theta) \end{aligned} \tag{5.7}$$

The total effective gravity does not depend on the azimuthal angle ϕ, so $g \equiv g(\theta) = \sqrt{g_x^2 + g_y^2 + g_z^2}$. With $g(\theta)$, the star's effective temperature distribution is known through Equation 5.2. The expression for temperature can then be inserted into any stellar emission function.

5.6.2 Limb-Darkening and Rectilinear Projection

Figure 5.1 shows the angle ϵ between the planet's line of sight and a given location on the stellar surface. The law of cosines gives $\mu = \cos(\pi - \epsilon)$ as

$$\mu = \frac{r^2 - R_\odot^2 - S^2}{2R_\odot S} \tag{5.8}$$

The planet's orbit vector is:

$$\vec{r} = r \begin{pmatrix} \cos(\Omega)\cos(\omega + f) - \sin(\Omega)\sin(\omega + f)\cos(i) \\ \sin(\Omega)\cos(\omega + f) + \sin(\Omega)\sin(\omega + f)\cos(i) \\ \sin(\omega + f)\sin(i) \end{pmatrix} \tag{5.9}$$

Modeling the star as an oblate spheroid gives the stellar radius:

$$\vec{R_\odot} = \frac{Req}{\sqrt{\sin^2(\theta) + \frac{cos^2(\theta)}{(1-\zeta)^2}}} \begin{pmatrix} \cos(\phi)\sin(\theta) \\ \sin(\phi)\sin(\theta) \\ \cos(\phi) \end{pmatrix} \tag{5.10}$$

where ζ is the star's oblateness and R_{eq} is the star's equatorial radius. The stellar oblateness can be derived via the Darwin-Radau relation (e.g., Bourda & Capitaine, 2004). S can be expressed in terms of r and $R_\odot$ via,

$$S = r^2 + R_\odot^2 - 2rR_\odot\cos(\alpha) \tag{5.11}$$

where

$$\cos(\alpha) = \frac{\vec{r} \cdot \vec{R_\odot}}{|\vec{r}||\vec{R_\odot}|} \tag{5.12}$$

Backsolving, the limb-darkening angle μ can be expressed in terms of the stars polar and azimuthal angles (ϕ, θ) and the planet's orbital elements. This same factor μ appears again in Equation 5.1 outside of the limb-darkening term. This extra factor projects the stellar area of the parameters as a rectilinear disk in the plane of the planet's sky, and is necessary to properly represent the stellar projected area exposed to the planet at any given moment.

5.6.3 Integral Limits

The limits of (ϕ, θ) are determined by the line-of-sight vector $\vec{S}$. From the planet's point of view, the stellar edge of visibility is set according to where $\vec{S}$ is tangential to the stellar surface ($\vec{S} \cdot \vec{R} = 0$). The angle $(\pi - \epsilon)$ is constrained to $-\pi/2 \leq \pi - \epsilon \leq \pi/2$. With $|\pi - \epsilon| \geq \pi/2$, the following inequality

$$r^2 \geq R_\odot^2 + S^2 \tag{5.13}$$

is true for the region of the star exposed to the planet. Using the law of cosines,

$$S^2 = r^2 + R_\odot^2 - 2(\vec{r} \cdot \vec{R_\odot}) \tag{5.14}$$

Inputting Equation 5.14 into Equation 5.13, a useable inequality describing the limits of (ϕ, θ) is obtained (Equation 5.4). Equations 5.9 and 5.10 can be employed to evaluate this inequality. Depending on the type of numerical integrator being used, this inequality can be applied to Equation 5.1 as a boolean statement or, more elegantly, by inserting dynamic functions $(\phi(\theta), \theta(\phi))$ as limits of integration.

5.6.4 Planet Equilibrium Temperature

Traditionally, a planet's equilibrium temperature is straightforward to calculate. However, the gravity-darkening effect can cause a planet to be exposed to different stellar effective temperatures and stellar projected areas throughout the course of its orbit – therefore, the stellar luminosity (as seen by the planet) can change over time. An approximate value of the instantaneous "effective" stellar luminosity can be expressed as an integral of Equation 5.1 over all wavelengths of the exposed part of the star,

$$\widehat{L}_\odot = \int_0^\infty K(\lambda) d\lambda \tag{5.15}$$

The integral limits given by Equation 5.4 apply to this integral. The total effective luminosity as seen by the planet is then,

$$L_\odot = \widehat{L}_\odot \frac{S}{\widehat{S}} \tag{5.16}$$

where S is the total stellar surface area of the oblate spheroid and $\widehat{S}$ is the stellar surface area exposed to the planet. The effective luminosity can then be used to approximate the planet's equilibrium temperature for a given part of its orbit,

$$T_{eq} \simeq \left(\frac{L_{\odot}(1-A)}{16\sigma\pi r^2} \right)^{1/4} \tag{5.17}$$

where A is the planet's albedo and σ is the Stefan-Boltzmann constant.

5.6.5 Insolation and Planet Obliquity

Figures 5.4 and 5.5 show normalized irradiance at 45° north latitude for different orbit geometries and axial tilts. I account for planet obliquity (η) and precession angle (ρ) by adopting the derivation from McGehee & Lehman (2012). I start with a point u on the surface of the planet in spherical coordinates,

$$u = \begin{pmatrix} \cos(\varphi)\cos(\gamma) \\ \cos(\varphi)\sin(\gamma) \\ \sin(\varphi) \end{pmatrix} \tag{5.18}$$

where φ is planet latitude and γ is planet longitude. I rotate this point on the surface by planet obliquity η and planet precession angle ρ,

$$\hat{u} = \begin{pmatrix} \cos(\rho) & -\sin(\rho) & 0 \\ \sin(\rho) & \sin(\rho) & 0 \\ 0 & 0 & 1 \end{pmatrix} \begin{pmatrix} \cos(\eta) & 0 & \sin(\eta) \\ 0 & 1 & 0 \\ -\sin(\eta) & 0 & \cos(\eta) \end{pmatrix} u \tag{5.19}$$

which gives the incident angle of any point on the planet's surface. I combine the effective luminosity seen by the planet at any time with its obliquity to find the incoming flux $F(\varphi, \gamma)$ of the planet as a function of planet latitude and longitude via,

$$F(\varphi, \gamma) = \int \frac{L_{\odot}(\hat{r} \cdot \hat{u})}{4\pi r^2} \mathrm{d}\gamma \tag{5.20}$$

where $L_{\odot}$ is given by Equation 5.16 and $\hat{r}$ is the unit vector of the planet's orbit, given by Equation 5.9.

To generate Figure 5.4, I set the planet latitute to 45° and integrate equation 5.20

with respect to all longitudes receiving irradiation. I perform this calculation at different points in the planet's orbit to find its normalized flux. Planet rotation rate does not affect this calculation because the integration includes all substellar longitudes.

5.7 Parameter Definitions

Parameter	Definition	Parameter	Definition
A	Planet's albedo	β	Gravity-darkening parameter (Eq. 5.2)
a	Planet's semi-major axis	γ	Planet's longitude (Eq. 5.18)
$B(\lambda, T(\theta))$	Stellar emission function	ϵ	angle between $\vec{S}$ and $\vec{R_\odot}$ (Fig. 5.1)
e	Planet's eccentricity	ζ	Star's oblateness
f	Planet's true anomaly	η	Planet's obliquity (Eq. 5.19)
$I(\mu)$	Stellar limb-darkening profile	θ	Star's polar angle
i	Planet inclination (spin-orbit misalignment)	λ	Stellar emission wavelength
J_2	Gravitational harmonic constant	μ	Rectilinear projection factor (Eq. 5.8)
$M_\odot$	Stellar mass	ρ	Planet's precession angle (Eq. 5.19)
$R_\odot$	Stellar radius (Eq. 5.10)	σ	Stefan-Boltmann constant
R_{eq}	Star's equatorial radius	ϕ	Star's azimuthal angle
u	Planet coordinates (Eq. 5.18)	φ	Planet's latitude (Eq. 5.18)
$\vec{r}$	Planet's orbit radius (Eq. 5.9)	Ω	Planet's longitude of ascending node
$\vec{S}$	Line-of-sight vector (Fig. 5.1)	$\Omega_\odot$	Star's angular rotation rate
$S_\odot$	The star's surface area	ω	Planet's argument of pericentre
α	angle between $\vec{r}$ and $\vec{R_\odot}$ (Fig. 5.1)		

Chapter 6: LASR-Guided Stellar Photometric Variability Subtraction: The Linear Algorithm For Significance Reduction

"LASR-guided stellar photometric variability subtraction - The Linear Algorithm for Significance Reduction", *Astronomy & Astrophysics*, vol. 615, no. 1, pp. 128-139

For this project, I took my research in a new direction out of necessity. I wanted to continue measuring spin-orbit alignment values around high mass stars; however, many of the most interesting unexplored Kepler *datasets were contaminated with stellar seismic activity. The star's varying brightness drastically affected the overall shape of the transit light curves I wanted to analyze, rendering them inaccessible. Instead of giving up on them, I decided to try subtracting the star's variable signal in order to separate the transit event from seismic activity. I first tried using existing programs for resolving stellar variability, but I found that with my chosen target system, KOI-976, these programs fell into degeneracies and could not properly fit the 100+ oscillations buried within the photometry. I therefore developed a tool specifically for subtracting stellar variability from rapidly-rotating pulsators such as δ-Scuti and γ-Doradus stars. This technique, which I call the Linear Algorithm for Significance Reduction – LASR – subtracts oscillations one at a time in frequency space, removing the issue of "too many frequencies". I publish this technique with the intent of using it to clean transit photometry around variable stars in the future in order to perform detailed analyses of the transit events.*

6.1 Abstract

We develop a technique for removing stellar variability in the light curves of δ-Scuti and similar variable stars. Our technique, which we name the Linear Algorithm for Significance Reduction (LASR), subtracts oscillations from a time series by minimizing their statistical significance in frequency space. We demonstrate that LASR can subtract variable signals of near-arbitrary complexity and can robustly handle close frequency pairs and overtone frequencies. We demonstrate that our algorithm performs an equivalent fit

as prewhitening to the straightforward variable signal of KIC 9700322. We also show that LASR provides a better fit to seismic activity than prewhitening in the case of the complex δ-Scuti KOI-976.

6.2 Introduction

Recent observing programs such as the *Kepler* mission have demonstrated that stellar variability in high mass stars often renders transit light curves unusable. (Basri et al., 2010). Additionally, high-mass stars often rotate rapidly, inducing an oblate shape and a pole-to-equator luminosity gradient across the stellar surface (Barnes, 2009; Barnes et al., 2011; Ahlers et al., 2015; Ahlers, 2016). These two effects add challenges to traditional light curve analysis, radial velocity measurements, Doppler tomography, and Rossiter McLaughlin measurements (Udry et al., 2007; Gimenez, 2006).

Approximately 60% of stars in the *Kepler* field of view display more stellar variability than the Sun (McQuillan, 2013). Such variability in transit light curves make traditional fitting challenging or impossible. Many of these targets are low-mass stars with variability caused by non-sinusoidal effects such as sunspots in their convective exteriors. Techniques for analyzing non-sinusoidal or non-periodic signals in the light curves such as the autocorrelation function (McQuillan et al., 2014) and Gaussian processes (Aigrain et al., 2016) produce strong results when applied to such stars. However, high-mass stars behave quite differently. At $\sim$ 6250K and hotter, stars invert to become radiative rather than convective at their surface (Winn et al., 2010). These stars have weak or nonexistent sunspots, and commonly rotate rapidly as a mostly-rigid body throughout their lifetimes. High-mass stars in the classical instability strip pulsate with radial and nonradial modes at high amplitudes. Therefore, analysis of stellar variability in the light curves of high-mass stars comes with a unique set of challenges and must be handled differently than variability in low-mass stars.

For classical pulsators such as Delta Scuti (δ-Scuti) and Gamma Doradus stars, the technique of "prewhitening" serves as the traditional method of asteroseismic analysis of transit light curves (e.g., Hernández et al., 2009; Poretti et al., 2009). Prewhitening fits sinusoids to photometry in an iterative process. This algorithm performs least-squares fits of several of the highest-amplitude oscillations in the time domain, determining approximate frequency, amplitude, and phase values for those oscillations. Prewhitening then fits several next-highest amplitude oscillations as a running total with the original

fit, repeating this process until stellar variability has been resolved.

Prewhitening often serves as an adequate method for removing stellar variability and determining the frequencies of oscillation in classical pulsators. However, we explore an alternate route out of necessity: we found that prewhitening provided an inadequate fit of the complex signal of Kepler Object of Interest (KOI) 976. KOI-976 is a high-amplitude, rapidly rotating δ-Scuti star with a complex variable signal. We tried to remove stellar variability from the transit light curve of KOI-976 by applying prewhitening, but we found that the complex signal contained too many oscillations for an accurate least-squares fit in the time domain. This roadblock led us to explore removing stellar variability in frequency-space instead through a new process that we call the Linear Algorithm for Significance Reduction (LASR).

In this paper we develop a frequency-domain method for removing the asteroseismic signal of high-mass pulsators. In §6.3 we detail the LASR technique. In §6.4 we apply LASR to a synthetic dataset and to δ-Scutis KIC 9700322 and KOI-976 to compare our technique against prewhitening. In §6.5 we discuss how LASR compares with existing techniques for analyzing variability in photometric data.

6.3 Methods

The Linear Algorithm for Significance Reduction (LASR) serves as an alternate method to prewhitening for signal reduction. It resolves a linear combination of oscillations in a time series by minimizing each oscillation's significance in the frequency domain. The algorithm operates iteratively: it reduces the highest-amplitude frequency, subtracts it from the time series, and then reduces the new highest-amplitude frequency.

The LASR technique has two primary advantages over traditional prewhitening. First, because it operates in frequency space, LASR's fitting process treats every oscillation as independent and avoids the degeneracies and complex parameter space that prewhitening encounters for datasets containing many oscillation modes. Second, the computer code behind LASR is extremely simple to run and requires very little knowledge of signal processing, making it an accessible technique for inexperienced researchers. In §6.3.1 we detail the algorithm for significance reduction. In §6.3.2 we discuss handling interdependent frequencies including close frequency pairs and integer-multiple frequencies. In §6.3.3 and §6.3.3, we detail our best-fit error analysis. In Appendix 6.7 we mathematically derive that LASR's straightforward approach to subtracting stellar oscillations is robust

for sinusoidal variability.

6.3.1 LASR Algorithm

LASR combines two well-known tools for signal processing: the Lomb-Scargle normalized periodogram, and the downhill simplex routine. To remove a single oscillation from a time series, LASR creates a window of the power spectrum of the time series around the peak of that oscillation (Figure 6.1). It then applies the downhill simplex routine to minimize that peak's significance.

We use the traditional Lomb-Scargle normalized periodogram (Press, 2007) for spectral analysis. The variations in brightness in high-amplitude δ-Scuti stars correspond to $\sim$5% variations in luminosity. We test whether these variations in uncertainty affect LASR by comparing the traditional Lomb-Scargle normalized periodogram with the generalized periodogram (e.g., Zechmeister & Kürster, 2009; Vio et al., 2010), which applies weights to each time bin according to its photometric uncertainty. We find no noticeable differences between the two methods for δ-Scuti stars KOI-976 and KIC 9700322. In the case of different noise properties and instrument systematics, more computationally expensive techniques that better handle time bin uncertainty may provide better results in the significance reduction process. Such systematics do not appear in this analysis; we therefore favor the traditional Lomb-Scargle periodogram,

$$P(\omega) = \frac{1}{2\sigma^2} \sum_{\phi=0,\frac{\pi}{2}} \frac{|\sum_j (h_j - \bar{h}) \sin(\omega(t_j - \tau) + \phi)|^2}{\sum_j \sin^2(\omega(t_j - \tau) + \phi)} \tag{6.1}$$

where h_j is the photometric flux value at time t_j, σ is the standard deviation in the dataset, ϕ is a phase offset that includes the values 0 and $\pi/2$, and $\omega = 2\pi f$ is the angular frequency being sampled. The offset τ is defined as,

$$\tan(2\omega\tau) = \frac{\sum_j \sin(2\omega t_j)}{\sum_j \cos(2\omega t_j)} \tag{6.2}$$

Several works exist to explain the statistical significance of frequency peaks in a periodogram (e.g., Press, 2007; Baluev, 2008). We represent the statistical significance of an oscillation in our dataset by sampling a window of frequencies around the peak. LASR evenly samples frequencies in a window approximately three times the full width of the peak.

LASR's adjustable window width depends on the width of frequency peaks; in general, a longer time series means narrower peaks in a periodogram. For KOI-976's short-cadence photometry discussed in §3, we sample $P(\omega)$ 40 times in a window width of 0.7μHz. We sum $P(\omega)$ values and use the resulting value to represent the significance $S_i(\omega, A, \delta)$ of the i^{th} oscillation in our dataset as a function of frequency ω, amplitude A, and phase δ.

The goal of LASR is to find the (w,A,δ) values that minimize $S(\omega, A, \delta)$. To do this, LASR uses a downhill simplex routine (Nelder & Mead, 1965; Press, 2007) to find the minimum of $S(\omega, A, \delta)$. We choose this minimization routine over more robust routines such as Powell's Method (Brent, 2013) because of the well-behaved parameter space that results from minimizing oscillations in the frequency domain (see Appendix 6.7). In Appendix 6.6.1, we list the necessary inputs to operate LASR and discuss computation times for running the algorithm, and in Appendix 6.6.2, we provide pseudocode for writing this routine in any computer programming language.

6.3.2 LASR and Interdependent Frequencies

In general, LASR removes oscillations from a dataset one at a time because they are linearly independent of one another. However, two scenarios arise where this assumption fails: close frequency pairs and overtone frequencies.

We define close frequency pairs as oscillations close enough together in frequency space that spectral analysis cannot resolve them individually (Figure 6.2), which can cause problems for prewhitening. If two frequencies exist close enough together that their periodogram windows (described in §6.3.1) overlap, then $S_i(\omega, A, \delta)$ cannot be properly minimized. Close frequency pairs are common both for complex datasets with many independent oscillations and for short time series that yield wide frequency peaks in their periodograms. LASR's solution, however, is simple: just remove both peaks at once. LASR can remove any number of peaks simultaneously by minimizing a combined $S_i(\omega, A, \delta)$ function that samples $P(\omega)$ values for all relevant peaks, and then minimizing that function within a single large simplex.

Overtone frequencies can be more challenging because they are not mathematically independent. The power spectrum of an oscillation can be changed dramatically by integer multiple frequencies. Therefore, minimizing $S_i(\omega, A, \delta)$ for a single frequency in this scenario will result in a poor determination of its (w,A,δ) values.

The solution is again to simply remove both peaks simultaneously. The underlying

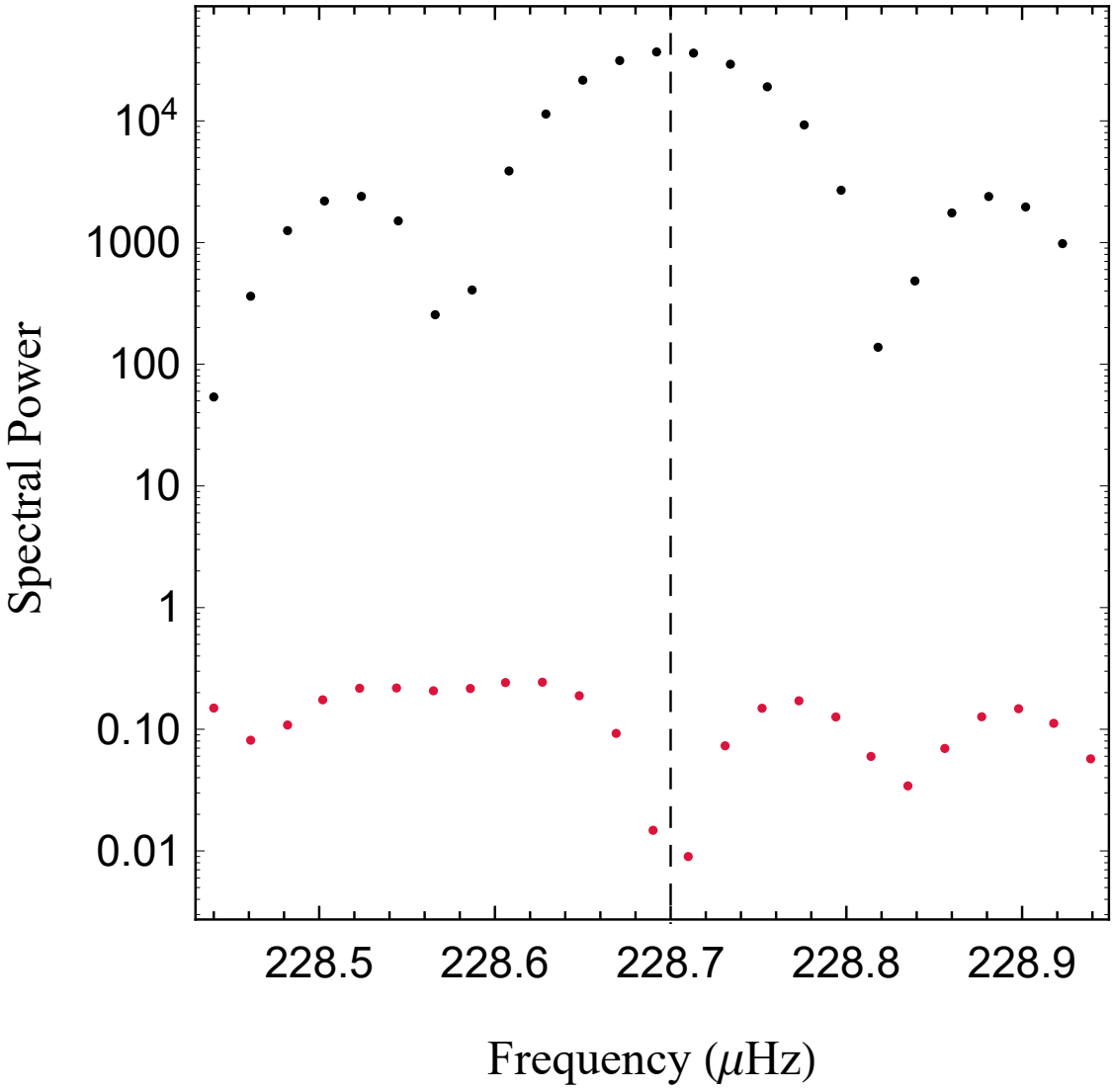

Figure 6.1: A periodogram window for the highest-amplitude peak in the synthetic time series discussed in §6.4.1. We set LASR to sample the spectral power of this peak 25 times. The black and red points show the $P_i(\omega)$ before and after LASR minimized the peak's significance. The unreduced oscillation shows a clear peak with aliasing on either side. The dashed line marks the true frequency of this oscillation. LASR successfully reduces this oscillation and yields correct measurements of its (w,A,δ) values (see Table 6.2.)

challenge stems from recognizing that this behavior is occurring in the first place. In our analysis of KOI-976, we identify all relevant frequencies through spectral analysis before applying the LASR technique to search for such resonances. We find scant evidence of this scenario arising in KOI-976, but we test simultaneous subtraction in an idealized dataset in §6.4.1 and show its successful determination of (w,A,δ) for overtone frequencies (Table 6.2).

Synthetic Time Series Quantity	**Value**
Length of synthetic dataset	90 days
Photometric cadence	1 min
Flux normalization constant	1.0
Transit gap start times	$\sum_{n=1}^{4} 20n$ days
Transit gap lengths	10 hr
Large gap start time	4.5×10^6 s
Large gap length	3.0×10^5 s
Gaussian uncertainty	5.0×10^{-4}
Lag correlation coefficient	0.5
Injected transit depth	1.2×10^{-4}
Injected transit period	15 days

Table 6.1: Global parameters of the synthetic data we generate to test LASR. We choose these parameters based on typical quantities of *Kepler* short-cadence photometry. The lag correlation coefficient sets the lag-1 autocorrelation between successive time samples, transforming Gaussian noise to correlated noise (Haykin, 2006).

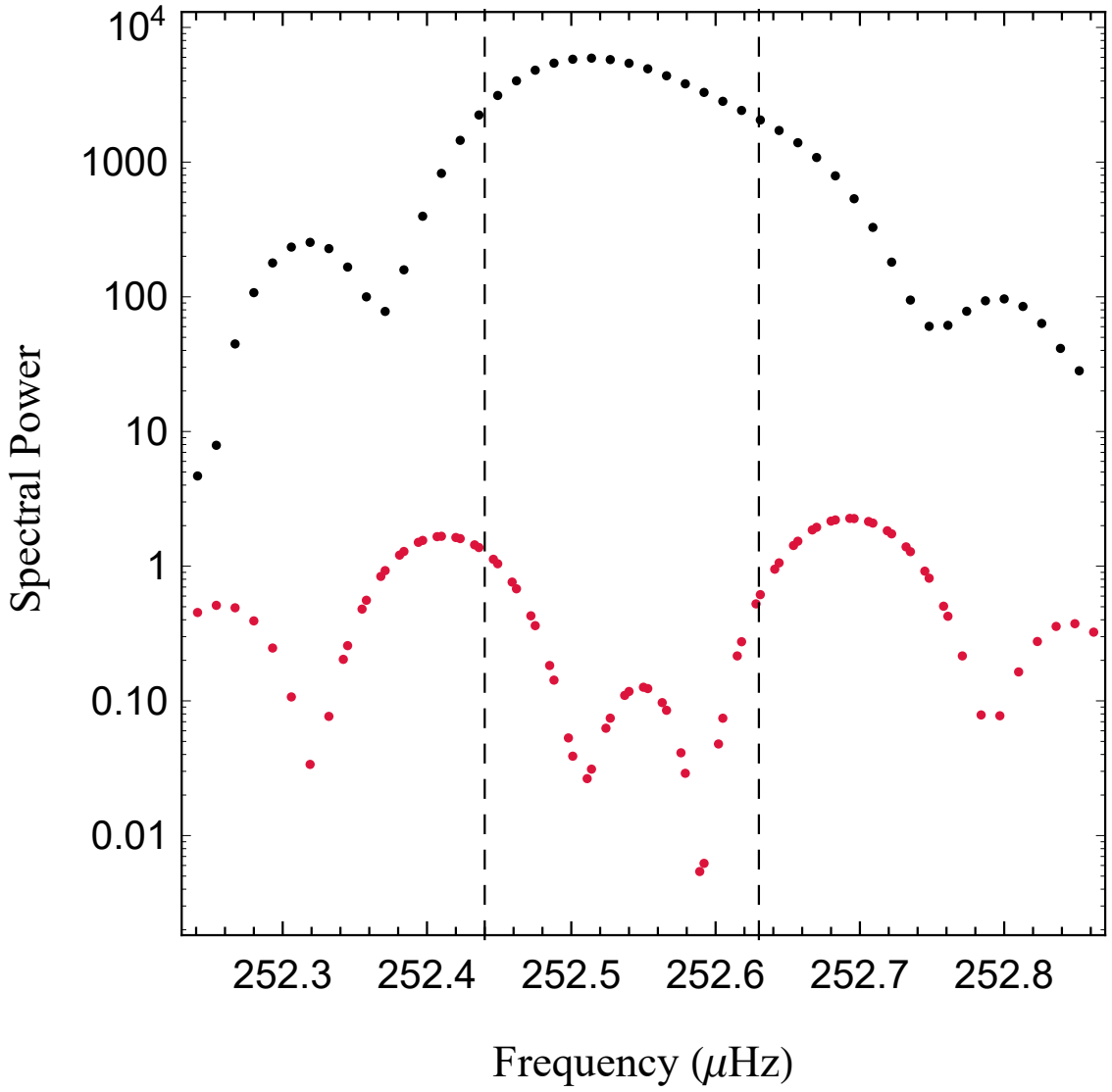

Figure 6.2: Log-scale plot of the power spectrum of two close frequencies (f_2 and f_3 in Table 6.2). The two oscillations appear in frequency space as a single asymmetric peak (black). LASR minimizes the significance of both peaks simultaneously (red) and accurately determines the (w,A,δ) of both oscillations. LASR samples frequencies of a periodogram window for each frequency; for close frequency pairs these two windows overlap.

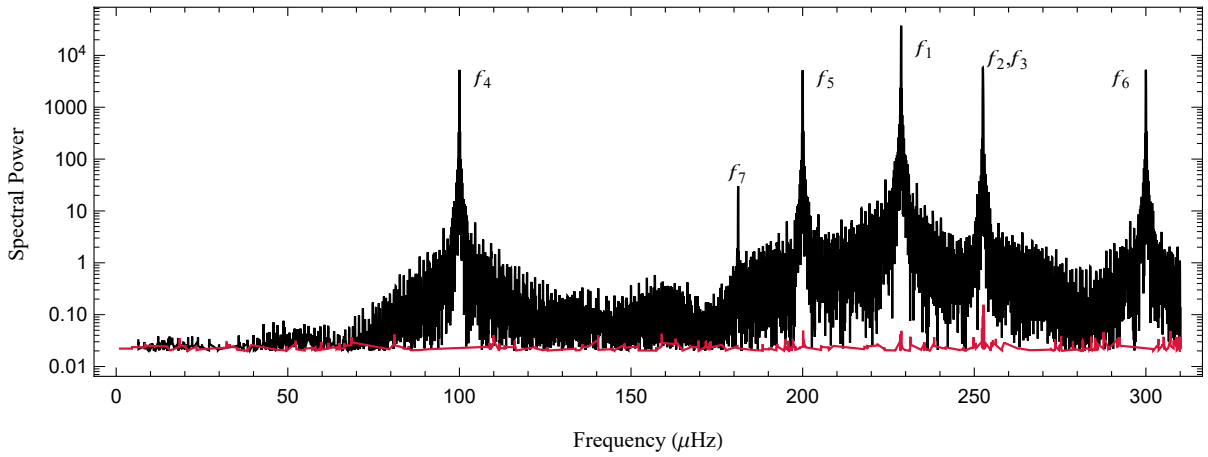

Figure 6.3: Total power spectrum of the synthetic time series before (black) and after (red) LASR reduction of its seven oscillations. As we show in Table 6.2, LASR reduces all oscillations by over 99.9% of their original significance and yields accurate (w,A,δ) values. The injected transit causes no noticeable effect on the power spectrum.

$f_{\#}$	$f_{\rm start}$ (μHz)	$f_{\rm result}$ (μHz)	$f_{\rm actual}$ (μHz)	$a_{\rm start}$ (10^{-3})	$a_{\rm result}$ (10^{-3})	$a_{\rm actual}$ (10^{-3})	$\delta_{\rm start}$	$\delta_{\rm result}$	$\delta_{\rm actual}$
1	228.68	228.7±5e-6	228.7	10.0	20.0013±0.0014	20.0	3.000	3.99998±0.00014	4.000
2	252.44	252.5±1.1e-5	252.5	1.0	7.5026±0.0015	7.5	3.000	2.9838±0.0003	3.00
3	252.63	252.6±1.7e-5	252.6	1.0	4.9985±0.0016	5.0	3.000	2.0011±0.0005	2.00
4	99.930	100.0±1.5e-5	100.0	1.0	7.4997±0.0014	7.5	3.000	0.0006±0.0004	0.000
5	199.965	200.0±1.3e-5	200.0	1.0	7.4993±0.0014	7.5	3.000	0.9987±0.0004	1.000
6	299.97	300.0±1.0e-5	300.0	1.0	7.4998±0.0014	7.5	3.000	2.0009±0.0003	2.000
7	181.194	181.1994±0.0002	181.2	0.1	0.4975±0.0014	0.5	3.000	5.013±0.006	5.000

Table 6.2: Oscillations added to a synthetic dataset to test LASR's ability to subtract variability. We list the seven oscillations in the order of: a single high-amplitude frequency (1), two close frequency pairs (2,3), three overtone frequencies (4,5,6), and a low-amplitude frequency whose amplitude matches the 1σ Gaussian noise of the dataset (7). For every oscillation, we list initial guesses, resulting best-fit values, and actual values for frequency (f), amplitude (A), and phase (δ). To simulate handling a real dataset, we set our starting frequency values to the peak values measured in frequency space. We set starting amplitudes to reasonable guesses based on the photometry, and we choose the random phase value 3.0 for all oscillations.

6.3.3 Error Analysis

We find the uncertainty in our best-fit parameters by calculating the covariance matrix of our dataset. Following Andrae (2010), we estimate that the likelihood function $\mathcal{L}$ of our model is nearly Gaussian at its maximum, allowing us to calculate the model's covariance matrix using the Fisher information matrix $\mathcal{I}$,

$$\mathcal{I}_{i,j} = \left(-\frac{\partial^2 \log \mathcal{L}}{\partial \theta_i \partial \theta_j} \right) \tag{6.3}$$

where θ_i is the i^{th} model parameter and $\log \mathcal{L} \propto \chi^2$. We numerically approximate these second derivatives in each element of the Fisher matrix as,

$$\mathcal{I}_{i \neq j} = \frac{\chi^2_{i+,j+} + \chi^2_{i-,j-} - \chi^2_{i+,j-} - \chi^2_{i-,j+}}{4 \Delta\theta_i \Delta\theta_j} \tag{6.4}$$

where $\chi^2_{i\pm,j\pm} = \chi^2(\theta_i \pm \Delta\theta_i, \theta_j \pm \Delta\theta_j)$ and $\Delta\theta_i$ is a very small step away from that parameter's best-fit value. In our calculations we use a frequency step size of $\Delta f = 10^{-10}$Hz, a normalized amplitude step size of $\Delta A = 10^{-6}$, and a phase step size of $\Delta p = 10^{-4}$.

We calculate the covariance matrix $\hat{\Sigma}$ of our best-fit model by taking the inverse of the Fisher matrix $\hat{\Sigma} = \mathcal{I}^{-1}$. We test whether $\hat{\Sigma}$ is positive definite by checking that all of its eigenvalues are positive. We take the diagonal elements of the covariance matrix to be the 1σ variance of our model parameters.

6.4 Results

We demonstrate the LASR technique by applying it to a synthetic time series and to δ-Scuti KOI-976's short-cadence *Kepler* photometry. We establish LASR's ability to measure the frequency, amplitude, and phase (w,A,δ) of oscillations in a time series containing Gaussian noise, time gaps, overtone frequencies, and close frequency pairs in §6.4.1. We demonstrate that LASR provides a much better fit to KOI-976's complex variable signal than traditional time-domain prewhitening in §6.4.3.

6.4.1 LASR Subtraction of Synthetic Oscillations

We create a synthetic time series containing seven oscillation modes commonly seen in a δ-Scuti variable star. We list the global parameters of the synthetic data in Table 6.1.

We create a 90-day time series with a 1-minute cadence and add Gaussian noise and data gaps that would commonly occur in *Kepler* photometry. We include five data gaps: four periodic gaps that represent masked-out transits, and one large gap representing the gaps commonly seen in short-cadence *Kepler* photometry. The synthetic time series includes correlated noise commonly seen in *Kepler* data. We generate Gaussian noise using a Box-Muller transform (Box & Muller, 1958; Press et al., 1992) and weight each uncertainty with a lag-1 autocorrelation between successive time samples (Haykin, 2006).

We include a small periodic transit in our synthetic time series to test its effects on our output code. The transit represents an Earth-radius planet orbiting a δ-Scuti star with a transit depth smaller than *Kepler's* detection limit. We list the transit parameters in Table 6.1. When testing its effects on our fitting process, we find this injected transit causes no significant influence on our results. In general, we find that transits do not influence the LASR algorithm until their transit depths grow larger than its photometric 1-σ uncertainty. At that limit, transits are readily visible in the time series and should be removed. We include this transit to show that low-amplitude transits at or below the detection limit do not noticeably effect our fitting results. In our algorithm, we treat removing time bins affected by transits as a standalone prerequisite before applying our significance reduction routine.

We add seven oscillation modes to the synthetic data to test LASR's capabilities. We include a single high-amplitude oscillation at 228.7μHz as an example of a stand-alone mode in the dataset. We add a close frequency pair at 252.5μHz and 252.6μHz to test LASR's ability to reduce oscillations that cannot be individually subtracted through spectral analysis. Additionally, we include three frequencies at integer multiples of one another to test LASR's ability to remove resonant, interdependent frequencies. We also add one oscillation whose photometric amplitude matches the synthetic data's 1σ uncertainty value to test our algorithm's ability to remove frequencies near the limit of statistical significance.

We subtract oscillations in order of highest-significance peak to lowest-significance (see Table 6.2 and Figure 6.3). LASR subtracts the single large peak (f_1) quickly and without difficulty. For the close frequency pair f_2 and f_3, we imitate a real time series by falsely identifying it as a single peak (see Figure 6.2). We tried a single starting frequency value of 252.53μHz and could not reduce the window's significance below 67.4%. We then set LASR to remove two close frequencies and immediately found the values listed in Table

6.2. LASR also yielded accurate (w,A,δ) values for the resonant f_4, f_5, and f_6 frequencies in a simultaneous fit.

6.4.2 LASR Comparison to Prewhitening: KIC 9700322

We subtract variability from the δ-Scuti star KIC 9700322 and compare our results to Breger et al. (2011), who fit stellar variability using the statistical package `period04`. Following Breger et al. (2011), we use incorporate *Kepler's* third quarter short-cadence photometry in our fit and measure 76 frequencies. We show our best-fit of the stellar variability in Figure 6.4 and compare the five highest-amplitude and five lowest-amplitude oscillations to Breger et al. (2011) in Table 6.3.

$f_{\#}$	$f_{\rm LASR}$ (μHz)	$f_{\rm PERIOD04}$ (μHz)	$a_{\rm LASR}$ (10^{-3})	$a_{\rm PERIOD04}$ (10^{-3})
1	145.473±1.8e-5	145.472	29.391±0.003	29.463
2	113.339±2e-5	113.339	27.268±0.003	27.266
3	258.811±8e-5	258.812	4.899±0.003	4.902
4	290.945±0.00015	290.945	2.665±0.003	2.663
5	32.1338±0.0002	32.133	2.637±0.003	2.633
...	...	...	...	...
72	727.361±0.014	727.362	0.015±0.003	0.019
73	263.59±0.02	263.588	0.014±0.003	0.015
74	392.96±0.02	393.002	0.0141±0.003	0.015
75	289.09±0.02	289.096	0.0135±0.003	0.016
76	598.96±0.02	598.982	0.0126±0.003	0.014

Table 6.3: Stellar frequencies and amplitudes of δ-Scuti KIC 9700322 measured using our algorithm and using the prewhitening program `period04` (Breger et al., 2011). We find that LASR and prewhitening produce almost identical results with little or no discrepancy between frequency and amplitude values. Breger et al. (2011) lists their frequency uncertainty as 0.001μHz and amplitude uncertainty as 0.003 for all modes of oscillation.

Our best-fit using LASR agrees almost completely with the frequencies and amplitudes found in Breger et al. (2011). We successfully model KIC 9700322's stellar variability throughout *Kepler's* Q3 short-cadence time series. We obtain a reduced χ^2 value of 1.13 for our fit; KIC 9700322's slightly reddened noise and its photometric outliers were the main causes for this value's deviation from unity. In the case of relatively straightforward

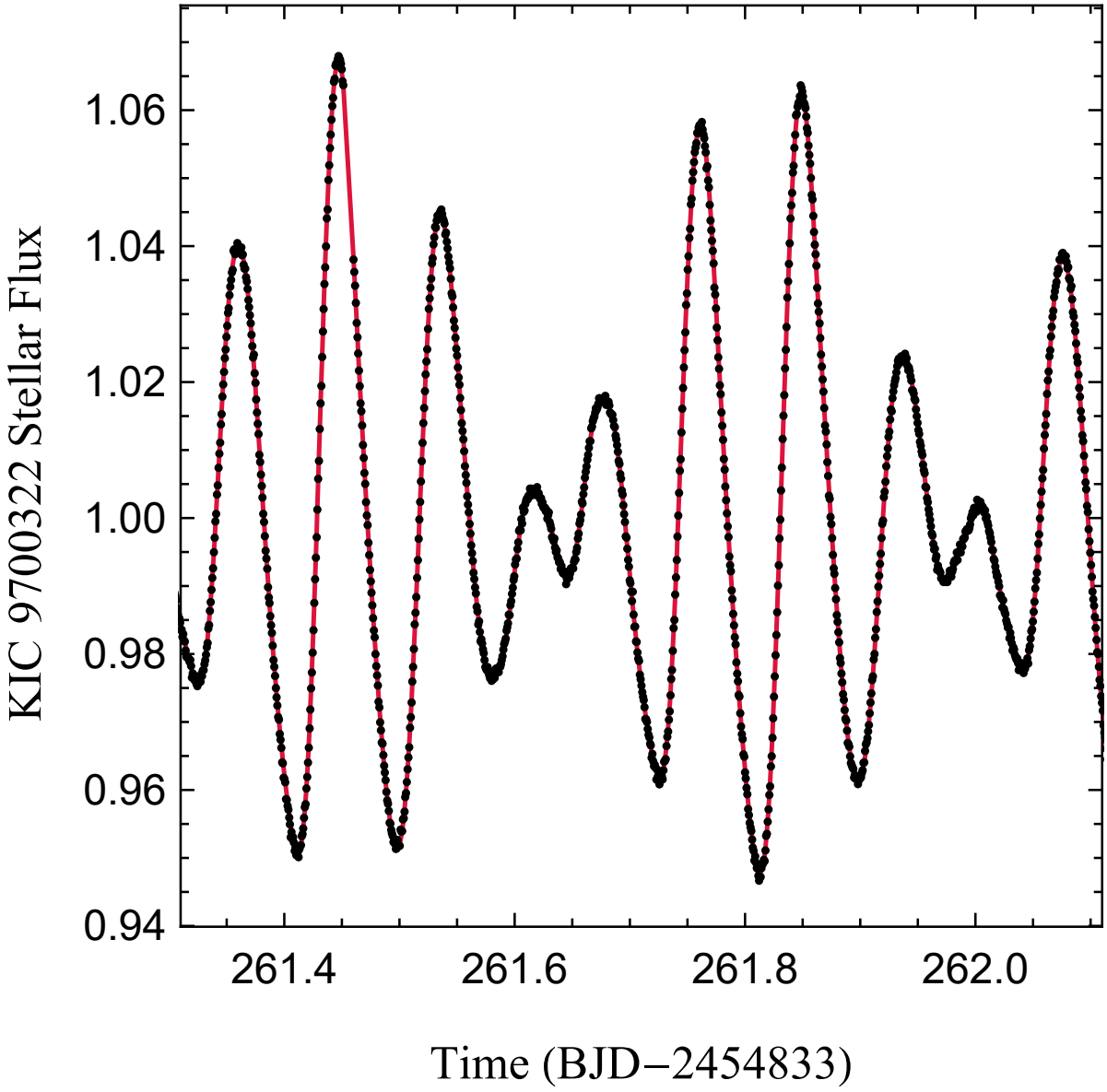

Figure 6.4: Sample of KIC 9700322's stellar variability (black) and our best-fit of the variable signal (red) using LASR. Our fit yields a reduced χ^2 value of 1.13.

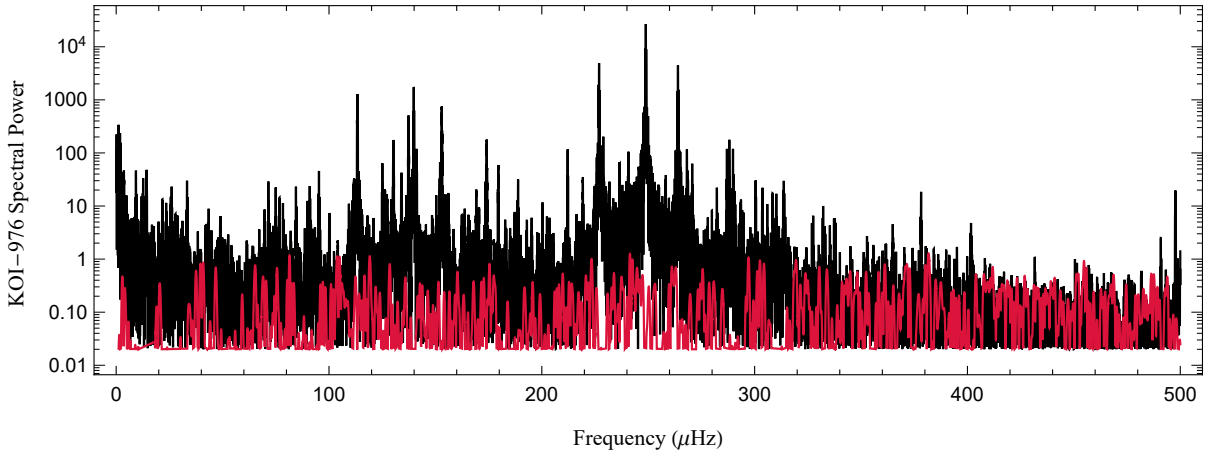

Figure 6.5: Lomb-Scargle Periodogram of KOI-976's short-cadence photometry before (black) and after (red) subtracting stellar variability. LASR reduced the spectral power of all oscillations from $\sim 10^4$ at the max to ~ 1.0. We reduce the representative significance of all subtracted oscillations by at least 98% and find that all significant oscillations are well-modeled as sinusoids.

variability, LASR and prewhitening are equally reliable, with the added bonus for LASR of only ever fitting a small parameter space at any time.

6.4.3 LASR Subtraction of KOI-976

We perform the same variability subtraction process as that described in §6.4.1 on Kepler Object of Interest (KOI) 976, a rapidly rotating δ-Scuti star that hosts an eclipsing binary companion. KOI-976 displays typical seismic activity for a δ-Scuti variable, possessing a few dominant nonradial modes between $\sim 100\mu\text{Hz} - 300\mu\text{Hz}$, as well as many low-amplitude oscillations spanning $\sim 0\mu\text{Hz} - 500\mu\text{Hz}$. In this analysis, we treat the star as a rigid rotator whose variable signal is well-modeled as a linear combination of sinusoids, which typically serves as an adequate assumption for δ-Scuti stars.

We perform this analysis on KOI-976's two available quarters of 1-minute *Kepler* photometry available on the Mikulski Archive for Space Telescopes. We use KOI-976's presearch data conditioning data (PDC) available through the *Kepler* analysis pipeline (Smith et al., 2012) and find no relevant differences between the PDC and raw-data versions of the photometry. KOI-976's time series contains a single transit by its stellar companion, as well as several significant data gaps. We mask out the transit and treat it as another gap in the time series. These gaps produce significant aliasing in periodograms. As we show in Figure 6.1, LASR subtraction of an oscillation removes both a peak and

its aliases, so even very large data gaps are surmountable through this technique.

We follow the process detailed in §6.3 and remove KOI-976's oscillations from the time series one at a time, except in the cases of close frequency pairs and overtone frequencies. We start with the highest-significance peak and work our way down to the significance detection limit based on KOI-976's photometric uncertainty of $\sim 10^{-4}$. In total, we subtract off 319 frequencies. Figure 6.5 shows the original and reduced frequency power spectrum of this dataset.

LASR successfully minimizes all significant frequencies present in KOI-976's short-cadence photometry. Figure 6.6 contrasts LASR with prewhitening and shows that LASR provides a better fit of KOI-976's oscillations than prewhitening through linear regression. We obtain a log-likelihood ratio between the two methods of $-2\log(\mathcal{L}_{PW}/\mathcal{L}_{LASR}) = 33806$, indicating a superior resolution of KOI-976's variability using our technique. We perform error analysis following §6.3.3.

6.5 Discussion & Conclusion

Our results show that LASR successfully removes stellar variability commonly seen in classical pulsators. Our technique can remove oscillations from photometry of arbitrary complexity so long as they are well-modeled as sinusoids. We find that for the rapidly-rotating δ-Scuti KOI-976, LASR serves as a superior method for variability subtraction over the traditional prewhitening approach of linear regression in the time domain. In particular, we find that LASR more accurately fits the frequencies of individual oscillations. It also better-resolves close frequency pairs that can be very difficult to identify when fitting in the time domain. Combined with LASR's reliability, relatively low computation cost, and ease-of-use, we consider our technique to be a useful tool for spectral analysis in asteroseismology.

We develop LASR out of necessity: we originally attempted to subtract variability from KOI-976 following traditional prewhitening methodology that has successfully resolved the oscillations of other δ-Scuti stars (Breger et al., 2011, 2012). We found, however, that for KOI-976, we could not obtain accurate frequencies using this technique. We observed several undesired aliasing effects occurring in the low-frequency range of our dataset due to these imperfect fits. We demonstrate that for this dataset, LASR successfully minimizes significant frequencies without producing aliasing effects (Figure 6.5) and provides a better fit of KOI-976's variable signal than prewhitening (Figure 6.6).

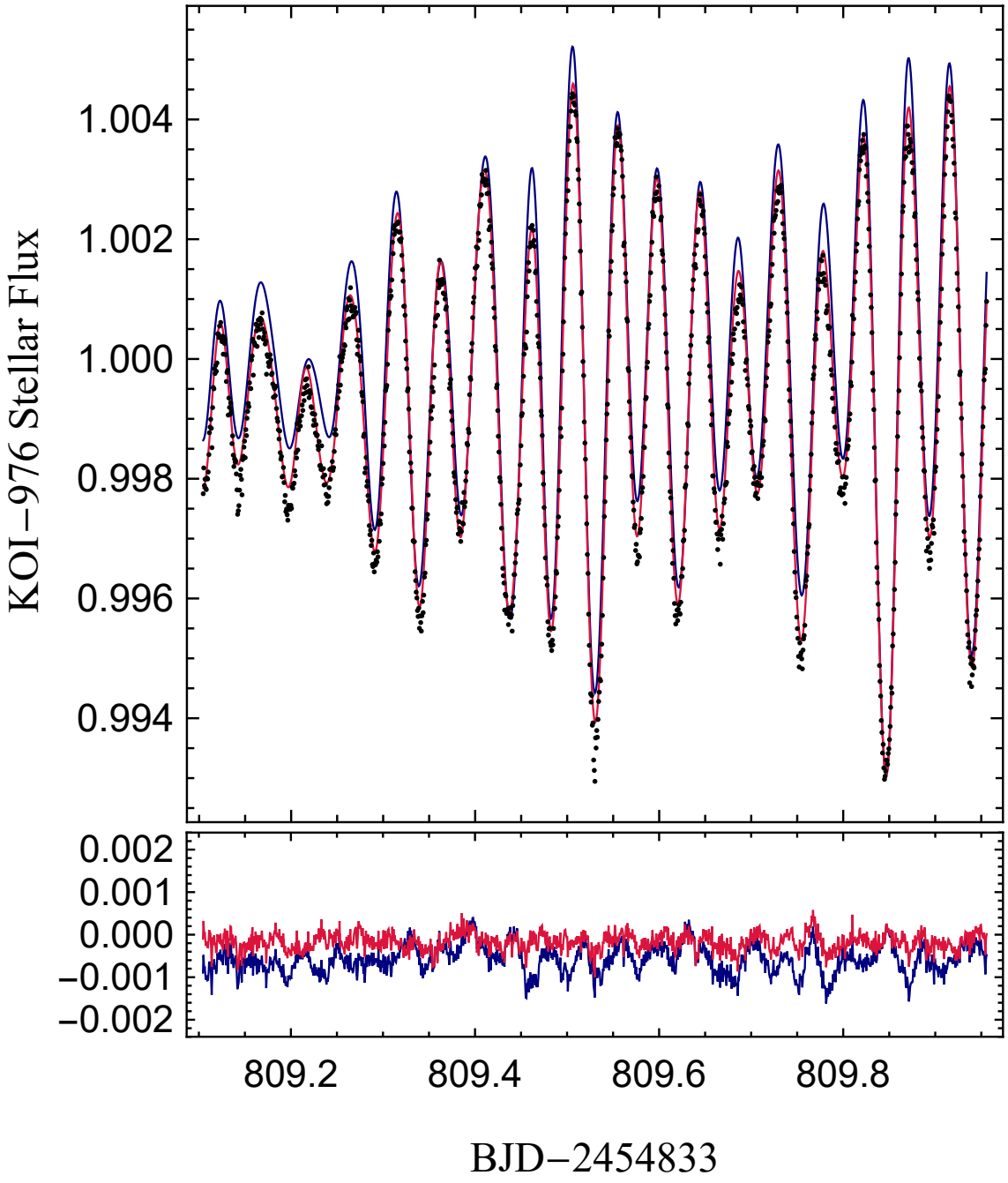

Figure 6.6: A comparison of variability subtraction using LASR (red) and traditional prewhitening (blue). We fit all KOI-976 short-cadence photometry and display a ~ 1 day sample of KOI-976's short-cadence photometry with best-fit (top) and its best-fit residuals (bottom). LASR produces a superior fit of KOI-976's seismic activity with a log-likelihood ratio of $-2\log(\mathcal{L}_{PW}/\mathcal{L}_{LASR}) = 33806$, which illustrates our motivation to create this technique, as it better-reduces complex seismic signals of classical pulsators.

We put forth LASR as one of many tools available for analyzing photometry. Existing tools such as Period04 (Lenz & Breger, 2004) and others (Akritas & Bershady, 1996; Vio & Wamsteker, 2002; Rohlfs & Wilson, 2013) provide robust and well-established techniques for signal processing of photometry. Additional techniques exist for analyzing stellar variability that contains non-sinusoidal or pseudo-periodic signals. These methods include modeling signals as multivariate random variables through Gaussian processes (MacKay, 1998; Rasmussen & Williams, 2006; Aigrain et al., 2016), detecting signals through autocorrelation functions (Edelson & Krolik, 1988; McQuillan et al., 2014), and analyzing time-variable signals through wavelet analysis. These techniques are important tools for transit detection, denoising signals, and removing pseudo-periodic stellar signals or oscillations that vary with time. They are particularly useful for analysis of dwarf stars, where solar flares, sunspots, and non-rigid stellar rotation produce complex variable signals in photometry that must be modeled as random events. These techniques produce reliable results in subtracting stellar variability but often come with the complications of being computationally expensive or from treating stellar variability as a random. The LASR routine serves as an inexpensive and straightforward tool for analyzing high-mass stars, which typically do not possess sunspots or flares (Didelon, 1984), whose surfaces behave as rigid rotators (Suarez et al., 2005), and whose oscillations commonly remain constant over long timescales when on the main sequence (Breger & Pamyatnykh, 1998).

LASR currently subtracts stellar variability that is well-modeled as a linear combination of sinusoids. Future works can expand this technique to combine LASR's significance reduction with Gaussian processes or wavelet analysis to analyze other forms of stellar variability. Such an approach could resolve a stellar signal without sacrificing information by treating seismic activity as a random process. Additionally, wavelet analysis could expand LASR's purview to the variable signal of heartbeat stars (Hambleton et al., 2013; Smullen & Kobulnicky, 2015) in the future.

6.6 LASR Algorithm

6.6.1 Inputs and Usage

LASR uses inputs to control its downhill simplex routine that customize its behavior to the target time series. We list the global parameters that typically remain constant throughout the subtraction process:

1. Frequency scale factor to set initial downhill step sizes. When working with KOI-976's high-precision photometry, we use a scale factor of $10^{-3}\mu$Hz.

2. Amplitude scale factor. Within an order of magnitude of the highest-significance oscillation's amplitude is typically adequate as an initial guess. This value can be set smaller as LASR subtracts smaller oscillations in the dataset.

3. Phase scale, typically set to 1.0.

4. Number of downhill steps for LASR to take. Convergence typically occurs within 50-100 steps for an independent oscillation but requires about twice as many steps for close frequency pairs or overtone frequencies.

5. The half-width of the peak of the highest-significance frequency in the dataset. This value determines the width of the periodogram window for LASR to sample during each subtraction. For KOI-976 we used a halfwidth of 0.35μHz.

6. The number of frequencies to sample in the periodogram window. We find that 10 points provide an adequate sampling of the periodogram window in our analysis, but because of LASR's relatively low computational cost, we use 25 points.

LASR requires the following inputs to subtract an oscillation:

1. Starting guess for frequency. Easily obtained via periodogram with sufficient accuracy.

2. Starting guess for amplitude. Order-of-magnitude values serve an adequate guess, as shown in Table 6.2.

3. Starting guess for phase. Any value between 0 and 2π typically suffices.

6.6.2 LASR Pseudocode

We write this algorithm in `c++` using established techniques for periodograms and downhill simplex routines following (Press, 2007). Our program includes proprietary optimization code and personalized libraries that make direct sharing of this program impractical. However, the LASR routine is straightforward to create. We provide an outline below that uses a periodogram window as a black-box function in a downhill

simplex routine to minimize significance and determine an oscillation's (w,A,δ) values. We also make an open-source version of our code available for download at `https://github.com/jpahlers/LASR`.

Data: $G = (T, U, \delta U)$ time series
Result: $G' = (T, V, \delta V)$ time series with highest-amplitude oscillation subtracted
Function: $S(G|\omega, A, \delta)$ calculates significance in periodogram window (§6.3.1) centered on frequency to subtract.
begin
  Remove all time bins affected by transits or other discrete events
  Set downhill simplex scale factors: $\{f_{\rm sc}, a_{\rm sc}, p_{\rm sc}\}$
  Set number of downhill steps to take: N
  Set number of samples in periodogram window: $npts$
  for # frequencies **do**
    Set starting guesses for of oscillation values to be fit: $\{f_{\rm start}, a_{\rm start}, p_{\rm start}\}$
    Calculate initial significance of periodogram window before subtraction
    for $n \in N$ **do**
      Take step in downhill simplex using $S(G|\omega, A, \delta)$ as black-box function (Press, 2007)
      Update (w,A,δ) best estimates
    end
    for $t \in T$ **do**
      Subtract oscillation from flux value: $V = U - A\sin(\omega x + p)$
    end
    $G \longleftarrow G'$
    Store best-fit (w,A,δ) results
  end
  Calculate best-fit confidence intervals (§6.3.3)
  Propagate uncertainty of oscillation subtraction into reduced timeseries.
end

6.6.3 Benchmark Results

We list benchmark performance results of the LASR routine below using the KOI-976 short-cadence data set. The computation time scales with the size of the time series and the desired precision, driven mainly by the cost of calculating periodogram significance values. To speed up our computation time, we compute trigonometric recurrences of the periodogram (Press, 2007) using two processors in parallel. In general, we find that $N = 100$ downhill steps is typically enough to determine the best-fit (w,A,δ) values of an oscillation to six significant figures and that 25 periodogram window samples robustly represents a frequency's significance.

Benchmark Quantity	**Value**
Number of downhill steps (N)	100
Time series data points	91235
Periodogram window samples	25
Computation time	12.58 s

Table 6.4: Quantities describing the LASR's computation time using KOI-976's short-cadence photometry. Our algorithm typically fits the frequency, amplitude, and phase of a single oscillation in a timeseries in approximately 100 downhill steps that each take ~ 0.1 seconds when applied to KOI-976's 91235 short-cadence time bins.

The computation time is primarily dedicated to calculating periodograms. Press (2007) shows how, depending on the choice of algorithm, Lomb-Scargle periodograms scale as $N \log(N)$, where N is the number of points in the time series. The fitting precision is controlled by the LASR's downhill simplex algorithm. The rate of convergence can vary largely between datasets, but we find that when fitting one oscillation (three parameters) in KOI-976's short-cadence photometry, we typically achieve four significance figures after ~ 50 downhill steps and six significant figures after ~ 100 downhill steps.

6.7 Derivation: One Minimum Per Parameter

The oscillation significance $S(\omega, A, \delta)$ is a black box function that represents the significance of the residuals of a subtracted oscillation. In this section we provide a derivation showing that $S(\omega, A, \delta)$ has only one minimum per parameter (i.e. that $S(\omega, A, \delta)$ is U-shaped in each dimension over all values) so long as the actual frequency and subtracted

frequency are relatively close ($|(\omega_1 - \omega_2)/(\omega_1 + \omega_2)| \lesssim 0.1$).

We start with two sine waves $\psi_1 = A_1 \sin(\omega_1 t + \delta_1)$ and $\psi_2 = A_2 \sin(\omega_2 t + \delta_2)$, where A_i, ω_i, and δ_i represent the amplitude, frequency, and phase of each function. A standard oscillation subtraction is therefore represented by,

$$\psi = \psi_1 - \psi_2 = A_1 \sin(\omega_1 t + \delta_1) - A_2 \sin(\omega_2 t + \delta_2) \tag{6.5}$$

Assuming $\omega_1 \approx \omega_2$, equation 6.5 can be expanded as,

$$\psi = A_1 \sin(\omega_1 t + \delta_1) - A_2 \sin(\omega_1 t + \delta_2) + A_2(\omega_1 - \omega_2) t \cos(\omega_2 t + \delta_2) + O((\omega_1 - \omega_2)^3) \tag{6.6}$$

Utilizing the Harmonic Addition theorem (e.g., Nahin, 2001), the zeroth-order terms $(A_1 \sin(\omega_1 t + \delta_1) - A_2 \sin(\omega_1 t + \delta_2))$ can be expressed as a single sine wave $A \sin(\omega_2 t + \delta)$, where

$$A = \sqrt{A_1^2 + A_2^2 - 2A_1 A_2 \cos(\delta_1 - \delta_2)} \tag{6.7}$$

and

$$\delta = \operatorname{atan}\left(\frac{A_1 \cos(\delta_1) - A_2 \sin(\delta_2)}{A_1 \sin(\delta_1) - A_2 \sin(\delta_2)}\right) \tag{6.8}$$

Therefore, this subtraction can be represented as,

$$\psi = A \sin(\omega_2 t + \delta) + A_2(\omega_1 - \omega_2) t \cos(\omega_2 t + \delta_2) + O((\omega_1 - \omega_2)^3) \tag{6.9}$$

Because $S(\omega, A, \delta)$ is roughly proportional to the square of the amplitude of ψ, minimizing Equation 6.9 minimizes $S(\omega, A, \delta)$. The oscillation residual ψ is minimized via minimizing A and $\omega_1 - \omega_2$. A is minimized via minimizing $A_1 - A_2$ and $\delta_1 - \delta_2$. These are the *only* minima that appear in ψ; therefore, only one global minimum per parameter exists.

Chapter 7: Summary and Conclusions

This dissertation summarizes my graduate research on exoplanets orbiting high-mass stars using NASA's *Kepler* telescope. The preceding chapters include a detailed explanation of the gravity-darkening technique used to measure orbit geometries from photometric datasets of planets transiting rapid rotators, as well as four publications relating to spin-orbit misalignment and planet formation.

In Chapter 2, I derive the phenomenon of gravity-darkening due to rapid stellar rotation. High-mass stars have weak external magnetic fields, allowing them to maintain their primordial rotation rates throughout their lifetimes and not slow down from magnetic braking the way low-mass stars do. These rapid rotators possess two stellar properties that can significantly affect transit light curves: an oblate spheroidal shape and a pole-to-equator luminosity gradient. I demonstrate the wide range of effects gravity-darkening can induce on transit photometry, and I describe how those effects can be used to constrain transit geometry. Ultimately, gravity-darkened transit light curves allow for the constraint of the angle between a planet's orbit normal and the star's spin axis (i.e., the system's spin-orbit alignment).

The gravity-darkening technique of measuring orbit geometries has several advantages, particularly that it depends primarily on transit photometry, the most readily available type of exoplanetary data to date. Exoplanet surveys such as NASA's *Kepler* mission have provided precision photometry of hundreds of thousands of stars, making this technique applicable to potentially hundreds of planets transiting high-mass stars (Barclay et al., 2018). Although the gravity-darkening signal in a transit light curve can often be quite subtle, Barnes et al. (2013) and others (Ahlers et al., 2014; Ahlers et al., 2015; Barnes et al., 2015; Masuda, 2015; Howarth & Morello, 2017) have demonstrated this technique's ability to measure transit geometry values from such anomalies.

The challenges of the gravity-darkening technique lie primarily with the parent star. Modeling the gravity-darkening and limb-darkening gradients across a stellar surface is not an exact science because neither stellar quality is fully understood; however, with more experience applying this technique and especially with more collaboration with alternate techniques for measuring orbit geometries such as asteroseismology or Doppler tomography, we will gain a better understanding of what gravity-darkening and limb-darkening coefficients best represent these A/F-type rapid rotators.

Chapter 3 measures the spin-orbit alignment value of Kepler Object of Interest (KOI) 368. This system is an eclipsing binary consisting of a rapidly-rotating A star and an eclipsing M dwarf and a mostly well-aligned configuration. This project established that the gravity-darkening technique can constrain spin-orbit angles for well-aligned systems by measuring the lack of gravity-darkening anomaly in their transit light curves. This work also provided a small step toward comparing spin-orbit misalignment in planets against spin-orbit misalignment in binary systems. With more analyses such as Barnes et al. (2011), the similarities and differences between planet formation and binary formation will become more clear, namely in whether one or the other more frequently produces spin-orbit misalignment.

Chapter 4 details the work in Ahlers et al. (2015), which measured the spin-orbit alignment value of a particularly interesting system in KOI-89 (now named Kepler-462). This system contains two Neptune-sized planets orbiting at 85 days and 207 days, respectively. The orbital planes of both planets are misaligned from their host star by about 70°, but are well-aligned with each other.

With Kepler-462's two planets misaligned but coplanar, the mechanism that caused misalignment in that system must have either affected both planets simultaneously or torqued the rotation axis of the host star itself. Only some of the proposed explanations for spin-orbit misalignment currently in the literature are capable of producing such a configuration. Planet-embryo collisions (Levison et al., 1998; Charnoz et al., 2001), chaotic evolution of stellar spin (Storch et al., 2014; Valsecchi & Rasio, 2014), magnetic torquing (Lai et al., 2011; Spalding & Batygin, 2014), coplanar high-eccentricity migration (Petrovich, 2014), and inclination resonance (Barnes et al., 2015) either cannot produce severe spin-orbit misalignment values, does not result in coplanar orbits, or disagrees with Kepler-462's fundamental parameters. Only star-disk-binary interactions (Lai, 2014; Xiang-Gruess & Papaloizou, 2014; Batygin, 2012), inclination driven by a warped disk (Terquem, 2013), planet-planet scattering (Ford et al., 2005; Chatterjee et al., 2008), Kozai resonance (Libert & Tsiganis, 2009; Thies et al., 2011), and internal gravity waves (Rogers et al., 2012; Fuller et al., 2015) are consistent with Kepler-462's present-day configuration. The Kozai and planet-planet scattering mechanisms are unlikely, but could not be ruled out in the event of additional planets in the system.

The Kepler-462 system exhibits significant transit timing variations (TTVs. Its two known planets are very near a 5:2 resonance (2.45), which may be the cause of its TTVs.

Additionally, with the orbits misaligned and the host star significantly oblate, the two planets likely precess on a timescale of tens-of-thousands of years. N-body integrations suggest that the system only appears stable in nearly-circular, coplanar orbital configurations.

Interestingly, a cursory examination of Kepler-462's known TTVs as observed by the *Kepler* telescope reveal them to be significantly non-sinusoidal, implying that additional bodies may be dynamically interacting with the two observed transiting planets. However, because Kepler-462c's orbital period is so long, *Kepler* only observed five transits for that planet. Working with advisor Barnes and Los Cumbres Observatory (LCO) team member Julian van Eyken, I was awarded observing time on the LCO global telescope network in the summer of 2016 to measure additional TTVs and hopefully perform an analysis to reveal additional planets in that system; unfortunately, the weather did not cooperate and Kepler-462 remains unsolved. This system is a promising target for follow-up observations to further explore its dynamic behavior.

Chapter 5 explores the influence of rapid stellar rotation on an exoplanet's climate. This sole-author project found that both stellar oblateness and the gravity-darkened stellar surface can majorly impact a planet's atmospheric and surficial processes. When in a spin-orbit misaligned configuration, an exoplanet is sometimes exposed to a rapid rotator's hotter poles or cooler equator throughout its orbit. If standing on the surface of such a planet, one would see the sun in the sky change both in shape and color throughout the year. Ahlers (2016) dubs the planetary effects brought about by orbiting such an extreme star "gravity-darkened seasons".

When a planet undergoing gravity-darkened seasons is located near its host star's equatorial plane, it is primarily exposed to the star's dimmer, cooler equator. Additionally, the projected disk of the star as seen by the planet is at its most oblate and therefore is smallest in projected surface area. When near the poles, the planet is more directly exposed to the hotter, brighter part of the stellar surface, and sees a less-oblate (and therefore larger) projected disk in the sky. As the planet revolves around its host star, its stellar irradiance changes drastically twice each orbit.

When combined with traditional seasons (i.e. seasons driven by planet obliquity), gravity-darkened seasons can produce yearly insolation patterns unlike anything seen in our solar system. One interesting gravity-darkened insolation pattern occurs when traditional summer and winter occur when the planet is near the stellar equatorial plane.

Around a slow rotator, the upper and lower hemispheres of the planet would receive the most/ the least stellar irradiance at this time, producing the hottest/ the coldest temperatures throughout its year. However, around a rapid rotator, the misaligned planet's traditional summer and winter occur near the dim stellar equator, when the planet receives the least stellar irradiance. The summer's high temperatures would therefore be mitigated, and the winter's low temperatures exaggerated. Also, in this configuration, traditional spring and autumn occur near the star's hotter poles, when the planet's stellar irradiance is highest. Both spring and autumn would therefore be much hotter than normally seen by traditional seasons. For planets orbiting extremely gravity-darkened stars, traditional spring and autumn could actually be significantly hotter than summer, producing two distinct hottest times of the year.

Ahlers (2016) showed that the nature of gravity-darkened seasons depends strongly on the planet's orbital configuration. When a planet is well-aligned with a rapid rotator, its irradiance as a function of time is not affected by its host star's asymmetric shape and experiences traditional seasons. The more misaligned a planet is, the higher the potential for gravity-darkened seasons to occur. Also, different planet obliquities force traditional seasons to combine with gravity-darkened seasons in different ways. For example, when traditional summer and winter occur near the stellar poles instead of its equator, summers can be extremely hot, and winters much warmer than usual. Additionally, misaligned planets orbiting rapid rotators would likely undergo axial precession for nonzero planet obliquities, causing the planet to be driven between various insolation scenarios over time.

One aspect of gravity-darkened seasons that certainly begs further exploration is that a star's emission spectrum changes with temperature. A rapid rotator's emission is much redder near its cooler equator than at its hotter, bluer poles. Interestingly, for hot high-mass stars with polar surface temperatures in the range of 7000k-9000k, the emission wavelength that changes the most in fractional intensity between the star's poles and its equator is in the ultraviolet range. A planet undergoing gravity-darkened seasons is not only much hotter near the star's poles, it specifically receives far more UV irradiation, which could destabilize a planet's ozone layer or drive other atmospheric proceses unlike anything observed in our solar system.

Further analysis of gravity-darkened seasons, such as applying global circulation or radiative transfer models to planets receiving these unusual insolation patterns, could better constrain the atmospheres, surfaces, and overall climatic effects of planets orbiting

high-mass stars.

Chapter 6 describes an additional tool for analyzing transit photometry of planets orbiting high-mass stars. In addition to often rapidly rotating, A/F-types stars commonly exhibit high-amplitude seismic activity that can obfuscate a transit light curve. Ahlers, John P. et al. (2018) developed a software tool specifically designed to subtract stellar variability from transit light curves of rapid rotators in order to allow for detailed analysis of the transit itself. The Linear Algorithm for Significance Reduction, or `LASR`, subtracts oscillations from a time series one at a time by fitting the frequency, amplitude, and phase of that oscillation in frequency space. It produces comparable or superior results in variability subtraction to commonly-used time-domain approaches in the scenarios of hundreds or more statistically significant oscillations embedded in a dataset and when dealing with correlated noise. Ultimately, `LASR` provides a new avenue for extracting information from transit light curves polluted by stellar seismic activity and allows for the gravity-darkening technique to be applied to transit light curves previously obstructed by stellar variability.

The content of this dissertation provides new techniques and observations for analyzing spin-orbit misalignment via transit photometry, and offers new insights to the formation, evolution, and current-day processes of planets orbiting high-mass, rapidly rotating stars. This subset of exoplanets remains largely unexplored, partially because of the observational challenges high-mass stars pose, and partially because the habitable zone of these stars are out at orbital periods we as a community are not yet adept at exploring. Their formation pathways and habitability remain largely unexplored, but current findings indicate that a diverse and interesting group of exoplanets wait to be discovered. At the advent of NASA's *TESS* mission, which will likely discover over a thousand exoplanets orbiting high-mass stars (Barclay et al., 2018), the discovery, characterization, and analysis of high-mass systems will undoubtedly flourish, continuing and expanding upon the works presented here.

References

Ahlers, J. P. 2016, Gravity-Darkened Seasons: Insolation Around Rapid Rotators, The Astrophysical Journal, 832, 93

Ahlers, J. P., Barnes, J. W., & Barnes, R. 2015, Spin-Orbit Misalignment of Two-Planet-System KOI-89 Via Gravity Darkening, Astrophysical Journal, 814, 67

Ahlers, J. P., Seubert, S. A., & Barnes, J. W. 2014, Spin-Orbit Alignment for 110 Day Period KOI368. 01 from Gravity Darkening, The Astrophysical Journal, 786, 131

Ahlers, John P., Barnes, Jason W., Horvath, Sarah A., Myers, Samuel A., & Hedman, Matthew M. 2018, LASR-guided stellar photometric variability subtraction - The Linear Algorithm for Significance Reduction, Astronomy & Astrophysics, 615, A128

Aigrain, S., Parviainen, H., & Pope, B. 2016, K2SC: flexible systematics correction and detrending of K2 light curves using Gaussian process regression, Monthly Notices of the Royal Astronomical Society, 459, 2408

Akritas, M. G., & Bershady, M. A. 1996, Linear regression for astronomical data with measurement errors and intrinsic scatter, arXiv preprint astro-ph/9605002

Albrecht, S., Winn, J. N., Johnson, J. A., et al. 2012, Obliquities of Hot Jupiter Host Stars: Evidence for Tidal Interactions and Primordial Misalignments, Astrophysical Journal, 757, 18

Alsubai, K., Parley, N., Bramich, D., et al. 2014, The Qatar Exoplanet Survey, arXiv preprint arXiv:1401.1984

Andrae, R. 2010, Error estimation in astronomy: A guide, arXiv preprint arXiv:1009.2755

Anglada-Escudé, G., Amado, P. J., Barnes, J., et al. 2016, A terrestrial planet candidate in a temperate orbit around Proxima Centauri, Nature, 536, 437

Antoniadou, K. I., & Voyatzis, G. 2015, Highly eccentric exoplanets trapped in mean-motion resonances, ArXiv e-prints

Bagnulo, S., Landstreet, J., Mason, E., et al. 2006, Searching for links between magnetic fields and stellar evolution-I. A survey of magnetic fields in open cluster A-and B-type stars with FORS1, Astronomy & Astrophysics, 450, 777

Bagnulo, S., Szeifert, T., Wade, G., Landstreet, J., & Mathys, G. 2002, Measuring magnetic fields of early-type stars with FORS1 at the VLT, Astronomy & Astrophysics, 389, 191

Bakos, G., Noyes, R., Kovács, G., et al. 2004, Wide-Field Millimagnitude Photometry with the HAT: A Tool for Extrasolar Planet Detection, Publications of the Astronomical Society of the Pacific, 116, 266

Baluev, R. V. 2008, Assessing the statistical significance of periodogram peaks, Monthly Notices of the Royal Astronomical Society, 385, 1279

Barclay, T., Pepper, J., & Quintana, E. V. 2018, A Revised Exoplanet Yield from the Transiting Exoplanet Survey Satellite (TESS), arXiv preprint arXiv:1804.05050

Barnes, J. W. 2007, Effects of orbital eccentricity on extrasolar planet transit detectability and light curves, Publications of the Astronomical Society of the Pacific, 119, 986

Barnes, J. W. 2009, Transit Lightcurves of Extrasolar Planets Orbiting Rapidly Rotating Stars, The Astrophysical Journal, 705, 683

Barnes, J. W., Ahlers, J. P., Seubert, S. A., & Relles, H. M. 2015, Probable Spin–Orbit Aligned Super-Earth Planet Candidate KOI2138, The Astrophysical Journal Letters, 808, L38

Barnes, J. W., & Fortney, J. J. 2003, Measuring the Oblateness and Rotation of Transiting Extrasolar Giant Planets, The Astrophysical Journal, 588, 545

Barnes, J. W., Linscott, E., & Shporer, A. 2011, Measurement of the Spin-Orbit Misalignment of KOI-13.01 from Its Gravity-darkened Kepler Transit Lightcurve, The Astrophysical Journals, 197, 10

Barnes, J. W., Quarles, B., Lissauer, J. J., Chambers, J., & Hedman, M. M. 2016a, Obliquity Variability of a Potentially Habitable Early Venus, arXiv preprint arXiv:1602.00053

Barnes, J. W., Van Eyken, J. C., Jackson, B. K., Ciardi, D. R., & Fortney, J. J. 2013, Measurement of Spin-orbit Misalignment and Nodal Precession for the Planet around Pre-main-sequence Star PTFO 8-8695 from Gravity Darkening, The Astrophysical Journal, 774, 53

Barnes, R., Deitrick, R., Greenberg, R., Quinn, T. R., & Raymond, S. N. 2015, Long-lived Chaotic Orbital Evolution of Exoplanets in Mean Motion Resonances with Mutual Inclinations, Astrophysical Journal, 801, 101

Barnes, R., Deitrick, R., Luger, R., et al. 2016b, The Habitability of Proxima Centauri b I: Evolutionary Scenarios, arXiv preprint arXiv:1608.06919

Basri, G., Borucki, W. J., & Koch, D. 2005, The Kepler Mission: A wide-field transit search for terrestrial planets, New Astronomy Reviews, 49, 478

Basri, G., Walkowicz, L. M., Batalha, N., et al. 2010, Photometric variability in Kepler target stars. II. An overview of amplitude, periodicity, and rotation in first quarter data, The Astronomical Journal, 141, 20

Batygin, K. 2012, A primordial origin for misalignments between stellar spin axes and planetary orbits, Nature, 491, 418

Batygin, K., & Adams, F. C. 2013, Magnetic and Gravitational Disk-Star Interactions: An Interdependence of PMS Stellar Rotation Rates and Spin-Orbit Misalignments, The Astrophysical Journal, 778, 169

Batygin, K., Bodenheimer, P. H., & Laughlin, G. P. 2016, In situ formation and dynamical evolution of hot Jupiter systems, The Astrophysical Journal, 829, 114

Batygin, K., & Brown, M. E. 2010, Early dynamical evolution of the Solar System: Pinning down the initial conditions of the Nice model, The Astrophysical Journal, 716, 1323

—. 2016, Evidence for a distant giant planet in the solar system, The Astronomical Journal, 151, 22

Benomar, O., Masuda, K., Shibahashi, H., & Suto, Y. 2014, Determination of three-dimensional spin-orbit angle with joint analysis of asteroseismology, transit lightcurve, and the Rossiter-McLaughlin effect: Cases of HAT-P-7 and Kepler-25, Publications of the Astronomical Society of Japan, 66, 94

Boehm, T., Holschneider, M., Lignieres, F., et al. 2015, Discovery of starspots on Vega-First spectroscopic detection of surface structures on a normal A-type star, Astronomy & Astrophysics, 577, A64

Boley, A. C., & Ford, E. B. 2013, The Formation of Systems with Tightly-packed Inner Planets (STIPs) via Aerodynamic Drift, arXiv preprint arXiv:1306.0566

Boley, A. C., Morris, M. A., & Ford, E. B. 2014, Overcoming the meter barrier and the formation of systems with tightly packed inner planets (STIPs), The Astrophysical Journal Letters, 792, L27

Bonnell, I. A., & Bate, M. R. 1994, The Formation of Close Binary Systems, The Astrophysical Journal

Borucki, W., Scargle, J., & Hudson, H. 1985, Detectability of extrasolar planetary transits, The Astrophysical Journal, 291, 852

Borucki, W. J. 2012, in American Astronomical Society Meeting Abstracts# 220, Vol. 220

Borucki, W. J. 2016, KEPLER Mission: development and overview, Reports on Progress in Physics, 79, 036901

Borucki, W. J., Koch, D. G., Dunham, E. W., & Jenkins, J. M. 1997, in ASP Conf. Ser. 119, 153

Borucki, W. J., Koch, D. G., Basri, G., et al. 2011, Characteristics of Planetary Candidates Observed by Kepler. II. Analysis of the First Four Months of Data, The Astrophysical Journal, 736, 19

Boss, A. P. 2002, Formation of gas and ice giant planets, Earth and Planetary Science Letters, 202, 513

Bourda, G., & Capitaine, N. 2004, Precession, nutation, and space geodetic determination of the Earth's variable gravity field, Astronomy & Astrophysics, 428, 691

Bourrier, V., & Hébrard, G. 2014, Detecting the spin-orbit misalignment of the super-Earth 55 Cancri e, Astronomy & Astrophysics, 569, A65

Box, G., & Muller, M. 1958, A note on the generation of normal random deviates, Annals of Mathematical Statistics, 29, 610

Brandt, T. D., McElwain, M. W., Turner, E. L., et al. 2014, An Analysis of the SEEDS High-Contrast Exoplanet Survey: Massive Planets or Low-Mass Brown Dwarfs?, arXiv preprint arXiv:1404.5335

Breger, M., & Pamyatnykh, A. 1998, Period changes of delta Scuti stars and stellar evolution, arXiv preprint astro-ph/9802076

Breger, M., Balona, L., Lenz, P., et al. 2011, Regularities in frequency spacings of δ Scuti stars: the Kepler star KIC 9700322, Monthly Notices of the Royal Astronomical Society, 414, 1721

Breger, M., Fossati, L., Balona, L., et al. 2012, Relationship between Low and High Frequencies in δ Scuti Stars: Photometric Kepler and Spectroscopic Analyses of the Rapid Rotator KIC 8054146, The Astrophysical Journal, 759, 62

Brent, R. P. 2013, Algorithms for minimization without derivatives (Courier Corporation)

Brown, T. M., Charbonneau, D., Gilliland, R. L., Noyes, R. W., & Burrows, A. 2001, Hubble Space Telescope time-series photometry of the transiting planet of HD 209458, The Astrophysical Journal, 552, 699

Brown, T. M., Charbonneau, D., Gilliland, R. L., Noyes, R. W., & Burrows, A. 2001, Hubble Space Telescope Time-Series Photometry of the Transiting Planet of HD 209458, The Astrophysical Journal, 552, 699

Bruzual A, G., & Charlot, S. 1993, Spectral evolution of stellar populations using isochrone synthesis, The Astrophysical Journal, 405, 538

Caldwell, M. M., & Flint, S. D. 1994, Stratospheric ozone reduction, solar UV-B radiation and terrestrial ecosystems, Climatic change, 28, 375

Campante, T., Lund, M., Kuszlewicz, J. S., et al. 2016, Spin–Orbit Alignment of Exoplanet Systems: Ensemble Analysis Using Asteroseismology, The Astrophysical Journal, 819, 85

Carciofi, A., De Souza, A. D., Magalhaes, A., Bjorkman, J., & Vakili, F. 2008, On the determination of the rotational oblateness of Achernar, The Astrophysical Journal Letters, 676, L41

Cassan, A., Kubas, D., Beaulieu, J.-P., et al. 2012, One or more bound planets per Milky Way star from microlensing observations, Nature, 481, 167

Chambers, J. E. 1999, A hybrid symplectic integrator that permits close encounters between massive bodies, Monthly Notices of the Royal Astronomical Society, 304, 793

Chaplin, W., Sanchis-Ojeda, R., Campante, T., et al. 2013, Asteroseismic determination of obliquities of the exoplanet systems Kepler-50 and Kepler-65, The Astrophysical Journal, 766, 101

Chaplin, W. J., Sanchis-Ojeda, R., Campante, T. L., et al. 2013, Asteroseismic determination of obliquities of the exoplanet systems Kepler-50 and Kepler-65, ArXiv e-prints

Charbonneau, P. 2014, Solar dynamo theory, Annual Review of Astronomy and Astrophysics, 52, 251

Charnoz, S., Thébault, P., & Brahic, A. 2001, Short-term collisional evolution of a disc perturbed by a giant-planet embryo, Astronomy & Astrophysics, 373, 683

Chatterjee, S., Ford, E. B., Matsumura, S., & Rasio, F. A. 2008, Dynamical outcomes of planet-planet scattering, The Astrophysical Journal, 686, 580

Christensen-Dalsgaard, J., Däppen, W., Ajukov, S., et al. 1996, The current state of solar modeling, Science, 272, 1286

Claret, A. 2017, Limb and gravity-darkening coefficients for the TESS satellite at several metallicities, surface gravities, and microturbulent velocities, Astronomy & Astrophysics, 600, A30

Claret, A., & Bloemen, S. 2011, Gravity and limb-darkening coefficients for the Kepler, CoRoT, Spitzer, uvby, UBVRIJHK, and Sloan photometric systems, Astronomy & Astrophysics, 529, A75

Claret, A., & Bloemen, S. 2011, Gravity and limb-darkening coefficients for the Kepler, CoRoT, Spitzer, uvby, UBVRIJHK, and Sloan photometric systems, Astronomy & Astrophysics, 529, A75

Claret, A., Hauschildt, P. H., & Witte, S. 2013, New limb-darkening coefficients for Phoenix/1d model atmospheres. II. Calculations for 5000 K $\leq T_{\rm eff} \leq$ 10 000 K Kepler,

CoRot, Spitzer, uvby, UBVRIJHK, Sloan, and 2MASS photometric systems, Astronomy & Astrophysics, 552, A16

Collier Cameron, A., Guenther, E., Smalley, B., et al. 2010, Line-profile tomography of exoplanet transits - II. A gas-giant planet transiting a rapidly rotating A5 star, Monthly Notices of the Astronomical Society, 407, 507

Cumming, A. 2004, Detectability of extrasolar planets in radial velocity surveys, Monthly Notices of the Royal Astronomical Society, 354, 1165

Deitrick, R., Barnes, R., McArthur, B., et al. 2015, The Three-dimensional Architecture of the υ Andromedae Planetary System, Astrophysical Journal, 798, 46

Demory, B.-O., Gillon, M., De Wit, J., et al. 2016, A map of the large day–night temperature gradient of a super-Earth exoplanet, Nature, 532, 207

Désert, J.-M., Charbonneau, D., Demory, B.-O., et al. 2011, The hot-Jupiter Kepler-17b: discovery, obliquity from stroboscopic starspots, and atmospheric characterization, The Astrophysical Journal Supplement Series, 197, 14

Désert, J.-M., Charbonneau, D., Demory, B.-O., et al. 2011, The Hot-Jupiter Kepler-17b: Discovery, Obliquity from Stroboscopic Starspots, and Atmospheric Characterization, The Astrophysical Journals, 197, 14

Didelon, P. 1984, Stellar magnetic fields, Astronomy and Astrophysics Supplement Series, 55, 69

Edelson, R., & Krolik, J. 1988, The discrete correlation function-A new method for analyzing unevenly sampled variability data, The Astrophysical Journal, 333, 646

Epstein, C. R., & Pinsonneault, M. H. 2013, How good a clock is rotation? The stellar rotation-mass-age relationship for old field stars, The Astrophysical Journal, 780, 159

Ford, E. B., Lystad, V., & Rasio, F. A. 2005, Planet–planet scattering in the upsilon Andromedae system, Nature, 434, 873

Forster, P., Ramaswamy, V., Artaxo, P., et al. 2007, in Climate Change 2007. The Physical Science Basis

Fortney, J. J., Demory, B.-O., Désert, J.-M., et al. 2011, Discovery and atmospheric characterization of giant planet Kepler-12b: An inflated radius outlier, The Astrophysical Journal Supplement Series, 197, 9

Frémat, Y., Zorec, J., Hubert, A.-M., & Floquet, M. 2005, Effects of gravitational darkening on the determination of fundamental parameters in fast-rotating B-type stars, Astronomy & Astrophysics, 440, 305

Fuller, J., Cantiello, M., Lecoanet, D., & Quataert, E. 2015, The spin rate of pre-collapse stellar cores: wave-driven angular momentum transport in massive stars, ArXiv e-prints

Gandolfi, D., Collier Cameron, A., Endl, M., et al. 2012, Doppler tomography of transiting exoplanets: a prograde, low-inclined orbit for the hot Jupiter CoRoT-11b, Astronomy And Astrophysics, 543, L5

Gandolfi, D., Cameron, A. C., Endl, M., et al. 2012, Doppler tomography of transiting exoplanets: a prograde, low-inclined orbit for the hot Jupiter CoRoT-11b, Astronomy & Astrophysics, 543, L5

Gaudi, B. S., & Winn, J. N. 2007, Prospects for the characterization and confirmation of transiting exoplanets via the Rossiter-McLaughlin effect, The Astrophysical Journal, 655, 550

Gaudi, B. S., Stassun, K. G., Collins, K. A., et al. 2017, A giant planet undergoing extreme-ultraviolet irradiation by its hot massive-star host, Nature, 546, 514

Gimenez, A. 2006, Equations for the analysis of the Rossiter-MCLaughlin effect in extrasolar planetary transits, The Astrophysical Journal, 650, 408

Gough, D., & McIntyre, M. 1998, Inevitability of a magnetic field in the Sun's radiative interior, Nature, 394, 755

Grießmeier, J.-M., Stadelmann, A., Grenfell, J., Lammer, H., & Motschmann, U. 2009, On the protection of extrasolar Earth-like planets around K/M stars against galactic cosmic rays, Icarus, 199, 526

Guenther, E. W., Díaz, R. F., Gazzano, J.-C., et al. 2012, Transiting exoplanets from the CoRoT space mission. XXI. CoRoT-19b: a low density planet orbiting an old inactive F9V-star, Astronomy And Astrophysics, 537, A136

Guillot, T., Burrows, A., Hubbard, W., Lunine, J., & Saumon, D. 1996, Giant planets at small orbital distances, The Astrophysical Journal Letters, 459, L35

Haigh, J. D. 2007, The Sun and the Earth's climate, Living Reviews in Solar Physics, 4, 1

Hambleton, K., Degroote, P., Conroy, K., et al. 2013, Physics of Eclipsing Binaries: Heartbeat Stars and Tidally Induced Pulsations, European Astronomical Society Publications Series, 64, 285

Hansen, C. J., & Kawaler, S. D. 1994, Stellar Interiors. Physical Principles, Structure, and Evolution. (New York: Springer-Verlag)

Harrington, J. P., & Collins, G. W. 1968, Intrinsic Polarization of Rapidly Rotating Early-Type Stars, The Astrophysical Journal, 151, 1051

Haykin, S. 2006, Nonlinear methods of spectral analysis, Vol. 34 (Springer Science & Business Media)

Held, I. M., & Soden, B. J. 2000, Water vapor feedback and global warming 1, Annual review of energy and the environment, 25, 441

Henry, G. W., Marcy, G. W., Butler, R. P., & Vogt, S. S. 1999, A transiting 51 Peg-like planet, The Astrophysical Journal Letters, 529, L41

Hernández, A. G., Moya, A., Michel, E., et al. 2009, Asteroseismic analysis of the CoRoT \ δ-Scuti star HD 174936, Astronomy & Astrophysics, 506, 79

Hirano, T., Sanchis-Ojeda, R., Takeda, Y., et al. 2012, Measurements of Stellar Inclinations for Kepler Planet Candidates, The Astrophysical Journal, 756, 66

Hirano, T., Sanchis-Ojeda, R., Takeda, Y., et al. 2012, Measurements of Stellar Inclinations for Kepler Planet Candidates, The Astrophysical Journal, 756, 66

Howard, A. W. 2013, Observed properties of extrasolar planets, science, 340, 572

Howarth, I. D., & Morello, G. 2017, Rapid rotators revisited: absolute dimensions of KOI-13, Monthly Notices of the Royal Astronomical Society, 470, 932

Huber, D., Carter, J. A., Barbieri, M., et al. 2013, Stellar Spin-Orbit Misalignment in a Multiplanet System, Science, 342, 331

Ibañez-Mejia, J. C., & Braithwaite, J. 2015, Stability of toroidal magnetic fields in stellar interiors, Astronomy & Astrophysics, 578, A5

Jackson, B., Barnes, R., & Greenberg, R. 2009, Observational evidence for tidal destruction of exoplanets, The Astrophysical Journal, 698, 1357

Jackson, B., Jensen, E., Peacock, S., Arras, P., & Penev, K. 2016, Tidal decay and stable Roche-lobe overflow of short-period gaseous exoplanets, Celestial Mechanics and Dynamical Astronomy, 126, 227

Johnson, M. C. 2013, Doppler tomographic observations of exoplanetary transits

Johnson, M. C., Cochran, W. D., Albrecht, S., et al. 2014, A Misaligned Prograde Orbit for Kepler-13 Ab via Doppler Tomography, The Astrophysical Journal, 790, 30

Kaib, N. A., Raymond, S. N., & Duncan, M. J. 2011, 55 Cancri: A Coplanar Planetary System That is Likely Misaligned with Its Star, Astrophysical Journal Letters, 742, L24

Kervella, P., Jankov, S., Vakili, F., et al. 2005, Gravitational-darkening of Altair from interferometry, Astronomy & Astrophysics, 442, 567

Kopal, Z. 1959, Close binary systems, The International Astrophysics Series, London: Chapman & Hall, 1959

Kozai, Y. 1962, Secular perturbations of asteroids with high inclination and eccentricity, The Astronomical Journal, 67, 591

Lai, D. 2014, Star–disc–binary interactions in protoplanetary disc systems and primordial spin–orbit misalignments, Monthly Notices of the Royal Astronomical Society, 440, 3532

Lai, D., Foucart, F., & Lin, D. N. 2011, Evolution of spin direction of accreting magnetic protostars and spin–orbit misalignment in exoplanetary systems, Monthly Notices of the Royal Astronomical Society, 412, 2790

Lammer, H., Selsis, F., Ribas, I., et al. 2003, Atmospheric loss of exoplanets resulting from stellar X-ray and extreme-ultraviolet heating, The Astrophysical Journal Letters, 598, L121

Lenz, P., & Breger, M. 2004, Period04: A software package to extract multiple frequencies from real data, Proceedings of the International Astronomical Union, 2004, 786

Lesage, A.-L., Spronck, J., Stuik, R., et al. 2014, in Ground-based and Airborne Telescopes V, Vol. 9145, International Society for Optics and Photonics, 914514

Levison, H. F., Lissauer, J. J., & Duncan, M. J. 1998, Modeling the diversity of outer planetary systems, The Astronomical Journal, 116

Libert, A.-S., & Tsiganis, K. 2009, Kozai resonance in extrasolar systems, Astronomy and Astrophysics, 493, 677

Lidov, M. 1961, Evolution of the planets artificial satellites orbits under effect of the outer bodies gravity perturbations, Artificial Satellites of the Earth, 5

Lissauer, J. J. 1993, Planet formation, Annual review of astronomy and astrophysics, 31, 129

Lissauer, J. J., Barnes, J. W., & Chambers, J. E. 2012, Obliquity variations of a moonless Earth, Icarus, 217, 77

Lissauer, J. J., Fabrycky, D. C., Ford, E. B., et al. 2011, A closely packed system of low-mass, low-density planets transiting Kepler-11, Nature, 470, 53

MacKay, D. J. 1998, Introduction to Gaussian processes, NATO ASI Series F Computer and Systems Sciences, 168, 133

Maeder, A. 2009, Physics, Formation and Evolution of Rotating Stars (Physics, Formation and Evolution of Rotating Stars: , Astronomy and Astrophysics Library, Volume . ISBN 978-3-540-76948-4. Springer Berlin Heidelberg, 2009), doi:10.1007/978-3-540-76949-1

Mandel, K., & Agol, E. 2002, Analytic Light Curves for Planetary Transit Searches, The Astrophysical Journal Letters, 580, L171

Martynov, D. Y. 1973, Eclipsing Variable Stars (Nauka, Moscow)

Masuda, K. 2015, Spin–Orbit Angles of Kepler-13Ab and HAT-P-7b from Gravity-darkened Transit Light Curves, The Astrophysical Journal, 805, 28

Mayor, M., & Queloz, D. 1995, A Jupiter-mass companion to a solar-type star, Nature, 378, 355

Mazeh, T. 2015, in Astronomical Society of the Pacific Conference Series, Vol. 496, Astronomical Society of the Pacific Conference Series, ed. S. M. Rucinski, G. Torres, & M. Zejda, 167

McAlister, H. A., ten Brummelaar, T. A., Gies, D. R., et al. 2005, First Results from the CHARA Array. I. An Interferometric and Spectroscopic Study of the Fast Rotator Leonis (Regulus), The Astrophysical Journal, 628, 439

McCullough, P. R., Stys, J., Valenti, J., et al. 2005, The XO project: searching for transiting extrasolar planet candidates, Publications of the Astronomical Society of the Pacific, 117, 783

McGehee, R., & Lehman, C. 2012, A Paleoclimate Model of Ice-Albedo Feedback Forced by Variations in Earth's Orbit, SIAM Journal on Applied Dynamical Systems, 11, 684

McLaughlin, D. B. 1924, Some results of a spectrographic study of the Algol system., The Astrophysical Journal, 60, 22

McQuillan, A. 2013, PhD thesis, University of Oxford

McQuillan, A., Mazeh, T., & Aigrain, S. 2014, Rotation periods of 34,030 Kepler main-sequence stars: the full autocorrelation sample, The Astrophysical Journal Supplement Series, 211, 24

Meadows, V. S., Arney, G. N., Schwieterman, E. W., et al. 2016, The Habitability of Proxima Centauri b: II: Environmental States and Observational Discriminants, arXiv preprint arXiv:1608.08620

Mestel, L. 1968, Magnetic braking by a stellar wind-I, Monthly Notices of the Royal Astronomical Society, 138, 359

Monnier, J. D., Zhao, M., Pedretti, E., et al. 2007, Imaging the Surface of Altair, Science, 317, 342

Murray, C. D., & Dermont, S. F. 2008, Solar System Dynamics (Cambridge University Press)

Naef, D., Latham, D., Mayor, M., et al. 2001, HD 80606 b, a planet on an extremely elongated orbit, Astronomy & Astrophysics, 375, L27

Nagasawa, M., Ida, S., & Bessho, T. 2008, Formation of hot planets by a combination of planet scattering, tidal circularization, and the Kozai mechanism, The Astrophysical Journal, 678, 498

Nahin, P. J. 2001, The Science of Radio (Springer Science & Business Media)

Nelder, J. A., & Mead, R. 1965, A simplex method for function minimization, The computer journal, 7, 308

Nutzman, P. A., Fabrycky, D. C., & Fortney, J. J. 2011, Using Star Spots to Measure the Spin-orbit Alignment of Transiting Planets, The Astrophysical Journal Letters, 740, L10

O'Brien, D. P., Morbidelli, A., & Levison, H. F. 2006, Terrestrial planet formation with strong dynamical friction, Icarus, 184, 39

O'Donovan, F. T., Charbonneau, D., & Hillenbrand, L. 2006, in Bulletin of the American Astronomical Society, Vol. 38, 1212

Ogilvie, G., & Lin, D. 2007, Tidal dissipation in rotating solar-type stars, The Astrophysical Journal, 661, 1180

Ohta, Y., Taruya, A., & Suto, Y. 2005, The Rossiter-McLaughlin effect and analytic radial velocity curves for transiting extrasolar planetary systems, The Astrophysical Journal, 622, 1118

Payne, M. J., Ford, E. B., & Veras, D. 2010, Transit timing variations for inclined and retrograde exoplanetary systems, The Astrophysical Journal Letters, 712, L86

Pepper, J., Pogge, R. W., DePoy, D., et al. 2007, The Kilodegree Extremely Little Telescope (KELT): A Small Robotic Telescope for Large-Area Synoptic Surveys, Publications of the Astronomical Society of the Pacific, 119, 923

Petrovich, C. 2014, Hot Jupiters from Coplanar High-eccentricity Migration, arXiv preprint arXiv:1409.8296

Petrovich, C. 2015, The Stability and Fates of Hierarchical Two-planet Systems, Astrophysical Journal, 808, 120

Podsiadlowski, P. 1993, in Planets around pulsars, Vol. 36, 149–165

Pollacco, D. L., Skillen, I., Cameron, A. C., et al. 2006, The WASP project and the SuperWASP cameras, Publications of the Astronomical Society of the Pacific, 118, 1407

Pont, F., Hebrard, J. M., Irwin, J. M., et al. 2009, Spin-Orbit Misalignment in the HD80606 Planetary System, The Astrophysical Journal

Pont, F., Endl, M., Cochran, W. D., et al. 2010, The spin-orbit angle of the transiting hot Jupiter CoRoT-1b, Monthly Notices of the Astronomical Society, 402, L1

Poretti, E., Michel, E., Garrido, R., et al. 2009, HD 50844: a new look at \ δ-Scuti stars from CoRoT space photometry, Astronomy & Astrophysics, 506, 85

Press, W. H. 2007, Numerical recipes 3rd edition: The art of scientific computing (Cambridge university press)

Press, W. H., Teukolsky, S. A., Vetterling, W. T., & Flannery, B. P. 1992, Random numbers, Numerical Recipes in C: The Art of Scientific Computing, 274

Press, W. H., Teukolsky, S. A., Vetterling, W. T., & Flannery, B. P. 2007, Numerical Recipes. The art of scientific computing, third edition (Cambridge: University Press)

Price, E. M., Rogers, L. A., Johnson, J. A., & Dawson, R. I. 2015, How Low can You go? The Photoeccentric Effect for Planets of Various Sizes, The Astrophysical Journal, 799, 17

Rasmussen, C. E., & Williams, C. K. 2006, Gaussian processes for machine learning, Vol. 1 (MIT press Cambridge)

Raymond, S. N., Barnes, R., Armitage, P. J., & Gorelick, N. 2008, Mean motion resonances from planet-planet scattering, The Astrophysical Journal Letters, 687, L107

Raymond, S. N., Barnes, R., Veras, D., et al. 2009, Planet-planet scattering leads to tightly packed planetary systems, The Astrophysical Journal Letters, 696, L98

Ribas, I., Guinan, E. F., Güdel, M., & Audard, M. 2005, Evolution of the solar activity over time and effects on planetary atmospheres. I. High-energy irradiances (1-1700 Å), The Astrophysical Journal, 622, 680

Ribas, I., Bolmont, E., Selsis, F., et al. 2016, The habitability of Proxima Centauri b. I. Irradiation, rotation and volatile inventory from formation to the present, arXiv preprint arXiv:1608.06813

Rice, W., & Armitage, P. J. 2005, Quantifying orbital migration from exoplanet statistics and host metallicities, The Astrophysical Journal, 630, 1107

Rogers, T. M., Lin, D. N. C., & Lau, H. H. B. 2012, Internal Gravity Waves Modulate the Apparent Misalignment of Exoplanets around Hot Stars, Astrophysical Journal Letters, 758, L6

Rohlfs, K., & Wilson, T. L. 2013, Tools of radio astronomy (Springer Science & Business Media)

Rossiter, R. A. 1924, On the detection of an effect of rotation during eclipse in the velocity of the brigher component of beta Lyrae, and on the constancy of velocity of this system., The Astrophysical Journal, 60, 15

Rowe, J. F., Bryson, S. T., Marcy, G. W., et al. 2014, Validation of Kepler's Multiple Planet Candidates. III. Light Curve Analysis and Announcement of Hundreds of New Multi-planet Systems, The Astrophysical Journal, 784, 45

Sanchis-Ojeda, R., & Winn, J. N. 2011, Starspots, Spin-Orbit Misalignment, and Active Latitudes in the HAT-P-11 Exoplanetary System, The Astrophysical Journal, 743, 61

Sing, D. K. 2010, Stellar limb-darkening coefficients for CoRot and Kepler, Astronomy & Astrophysics, 510, A21

Sing, D. K. 2010, Stellar limb-darkening coefficients for CoRot and Kepler, Astronomy & Astrophysics, 510, A21

Smith, J. C., Stumpe, M. C., Van Cleve, J. E., et al. 2012, Kepler presearch data conditioning II-A bayesian approach to systematic error correction, Publications of the Astronomical Society of the Pacific, 124, 1000

Smullen, R. A., & Kobulnicky, H. A. 2015, Heartbeat stars: spectroscopic orbital solutions for six eccentric binary systems, The Astrophysical Journal, 808, 166

Spalding, C., & Batygin, K. 2014, in AAS/Division for Planetary Sciences Meeting Abstracts, Vol. 46

Storch, N. I., Anderson, K. R., & Lai, D. 2014, Chaotic dynamics of stellar spin in binaries and the production of misaligned hot Jupiters, Science, 345, 1317

Suarez, J. C., Bruntt, H., & Buzasi, D. 2005, Modelling of the fast rotating δ Scuti star Altair, Astronomy & Astrophysics, 438, 633

Szopa, C., Cernogora, G., Boufendi, L., Correia, J. J., & Coll, P. 2006, PAMPRE: A dusty plasma experiment for Titan's tholins production and study, Planetary and space Science, 54, 394

Terquem, C. 2013, The effects of disc warping on the inclination of planetary orbits, Monthly Notices of the Royal Astronomical Society, 435, 798

Teyssandier, J., Terquem, C., & Papaloizou, J. C. B. 2013, Orbital evolution of a planet on an inclined orbit interacting with a disc, Monthly Notices of the Astronomical Society, 428, 658

Thies, I., Kroupa, P., Goodwin, S. P., Stamatellos, D., & Whitworth, A. P. 2011, A natural formation scenario for misaligned and short-period eccentric extrasolar planets, Monthly Notices of the Royal Astronomical Society, 417, 1817

Toomre, J., Zahn, J.-P., Latour, J., & Spiegel, E. 1976, Stellar convection theory. II-Single-mode study of the second convection zone in an A-type star, The Astrophysical Journal, 207, 545

Traub, W. A. 2011, Terrestrial, habitable-zone exoplanet frequency from Kepler, The Astrophysical Journal, 745, 20

Triaud, A. H. M. J., Queloz, D., Bouchy, F., et al. 2009, The Rossiter-McLaughlin effect of CoRoT-3b and HD 189733b, Astronomy And Astrophysics, 506, 377

Turbet, M., Leconte, J., Selsis, F., et al. 2016, The habitability of Proxima Centauri b II. Possible climates and Observability, Astronomy and Astrophysics-A&A, arXiv

Udry, S., Fischer, D., & Queloz, D. 2007, A decade of radial-velocity discoveries in the exoplanet domain, Protostars and Planets V, 951, 685

Valsecchi, F., & Rasio, F. A. 2014, Tidal Dissipation and Obliquity Evolution in Hot Jupiter Systems, The Astrophysical Journal, 786, 102

Van Cleve, J. E., & Caldwell, D. A. 2016, Kepler instrument handbook, Kepler Science Document, KSCI-19033-002, Edited by Michael R. Haas and Steve B. Howell

Van Eylen, V., & Albrecht, S. 2015, Eccentricity from Transit Photometry: Small Planets in Kepler Multi-planet Systems Have Low Eccentricities, Astrophysical Journal, 808, 126

Van Eylen, V., Lund, M. N., Silva Aguirre, V., et al. 2014, What Asteroseismology can do for Exoplanets: Kepler-410A b is a Small Neptune around a Bright Star, in an Eccentric Orbit Consistent with Low Obliquity, Astrophysical Journal, 782, 14

Villaver, E., Livio, M., Mustill, A. J., & Siess, L. 2014, Hot jupiters and cool stars, The Astrophysical Journal, 794, 3

Vio, R., Andreani, P., & Biggs, A. 2010, Unevenly-sampled signals: a general formalism for the Lomb-Scargle periodogram, Astronomy & Astrophysics, 519, A85

Vio, R., & Wamsteker, W. 2002, Joint Time–Frequency Analysis: A tool for exploratory analysis and filtering of non-stationary time series, Astronomy & Astrophysics, 388, 1124

Von Zeipel, H. 1924, The radiative equilibrium of a rotating system of gaseous masses, Monthly Notices of the Royal Astronomical Society, 84, 665

White, R. J., & Ghez, A. M. 2001, Observational Constraints on the Formation and Evolution of Binary Stars, The Astrophysical Journal

Winn, J. N., Fabrycky, D., Albrecht, S., & Johnson, J. A. 2010, Hot stars with hot Jupiters have high obliquities, The Astrophysical Journal Letters, 718, L145

Winn, J. N., Noyes, R. W., Holman, M. J., et al. 2005, Measurement of spin-orbit alignment in an extrasolar planetary system, The Astrophysical Journal, 631, 1215

Winn, J. N., Holman, M. J., Henry, G. W., et al. 2007, The Transit Light Curve Project. V. System Parameters and Stellar Rotation Period of HD 189733, Astronomical Journal, 133, 1828

Winn, J. N., Holman, M. J., Henry, G. W., et al. 2007, The transit light curve project. V. System parameters and stellar rotation period of HD 189733, The Astronomical Journal, 133, 1828

Winn, J. N., Howard, A. W., Johnson, J. A., et al. 2009, The transit ingress and the tilted orbit of the extraordinarily eccentric exoplanet HD 80606b, The Astrophysical Journal, 703, 2091

Winn, J. N., Howard, A. W., Johnson, J. A., et al. 2011, Orbital Orientations of Exoplanets: HAT-P-4b is Prograde and HAT-P-14b is Retrograde, Astronomical Journal, 141, 63

Woolfson, M. M. 1993, The Solar System - Origin and Evolution, Astronomy & Geophysics, 34

Wright, J. T., Fakhouri, O., Marcy, G. W., et al. 2011, The Exoplanet Orbit Database, The Astrophysical Journal, doi:10.1086/659427

Xiang-Gruess, M., & Papaloizou, J. 2014, Evolution of a disc–planet system with a binary companion on an inclined orbit, Monthly Notices of the Royal Astronomical Society, 440, 1179

Yoon, J., Peterson, D. M., Kurucz, R. L., & Zagarello, R. J. 2010, A New View of Vega's Composition, Mass, and Age, The Astrophysical Journal, 708, 71

Yung, Y. L. 2005, in AGU Fall Meeting Abstracts

Zechmeister, M., & Kürster, M. 2009, The generalised Lomb-Scargle periodogram-a new formalism for the floating-mean and Keplerian periodograms, Astronomy & Astrophysics, 496, 577

Zhou, G., & Huang, C. X. 2013, A Highly Inclined Orbit for the 110 Day Period M-dwarf Companion KOI-368.01, The Astrophysical Journal Letters, 776, L35

Appendix A: Copyright for Published Articles

A.1 Copyright for IOP Publishing

"Upon transfer of copyright, IOP and/or the copyright owner grants back to authors a number of rights. These include the right to include the Final Published Version of the article in your research thesis or dissertation. Please include citation details and, for online use, a link to the Version of Record. IOP's permission will be required for commercial use of an article published as part of your thesis. IOP does not allow ProQuest to publish or sell the article as part of your dissertation."

Links to publications:
Chapter 3: http://iopscience.iop.org/article/10.1088/0004-637X/786/2/131/meta
Chapter 4: http://iopscience.iop.org/article/10.1088/0004-637X/814/1/67/meta
Chapter 5: http://iopscience.iop.org/article/10.3847/0004-637X/832/1/93/meta

A.2 Copyright for EDP Sciences

"The copyright consists of all rights protected by the worldwide copyright laws, in all languages and forms of communication, including the right to furnish the article or the abstracts to abstracting and indexing services, and the right to republish the entire article in any format or medium. In return, ESO grants to the author(s) the non-exclusive right of republication, subject only to their giving appropriate credit to A&A. This non-exclusive right of republication permits authors to post the published PDF version of the above article on their personal and/or institutional web site(s), including ArXiV. The non-exclusive right of republication also includes the authors' right to grant reproduction of parts of your article wherever they wish, provided they request the permission to do so from the A&A Editor-in-Chief (aanda.paris@obspm.fr). To protect the copyright in the article, the following notice should be included in the credit: 'Credit: Author, A&A, vol., page, year, reproduced with permission, © ESO'."

Credit for Chapter 6: Ahlers, J., Barnes, J., Horvath, S., Myers, S., Hedman, M., A&A,

vol. 615, no. 1, pp. 128-139, 2018, reproduced with permission, © ESO

Links to publication:
Chapter 6: https://www.aanda.org/articles/aa/pdf/2018/07/aa32446-17.pdf